DDA1, a novel factor in transcription-coupled repair, modulates CRL4CSA dynamics at DNA damage-stalled RNA polymerase II

Alex Pines (a.pines@erasmusmc.nl)
Erasmus MC https://orcid.org/0000-0001-7990-910X

Diana Llerena Schiffmacher
Erasmus MC https://orcid.org/0009-0000-5938-9311

Shun-Hsiao Lee
Netherlands Cancer Institute

Katarzyna Kliza
Radboud Institute

Arjan Theil
Erasmus MC & Oncode Institute https://orcid.org/0000-0001-5779-1681

Masaki Akita
Erasmus MC

Angela Helfricht
Erasmus MC

Karel Bezstarosti
Erasmus MC

Camila Gonzalo-Hansen
Erasmus MC

Haico van Attikum
Leiden University Medical Center

Matty Verlaan-de Vries
Leiden University Medical Center

Alfred Vertegaal
Leiden University Medical Centre

Jan Hoeijmakers
Erasmus MC https://orcid.org/0000-0003-3526-7795

Jurgen Marteijn
Department of Molecular Genetics, Oncode Institute, Erasmus MC Cancer Institute, Erasmus University Medical Center https://orcid.org/0000-0001-9321-518X

Hannes Lans
Erasmus MC https://orcid.org/0000-0003-4417-5358

Jeroen Demmers
Erasmus MC https://orcid.org/0000-0002-8757-9611
Michiel Vermeulen
Radboud University Nijmegen https://orcid.org/0000-0003-0836-6894
Titia Sixma
NKI, the Netherlands https://orcid.org/0000-0001-6180-0632
Tomoo Ogi
Nagoya University https://orcid.org/0000-0002-5492-9072
Wim Vermeulen
Erasmus MC https://orcid.org/0000-0003-3616-734X

Article

Keywords:

Posted Date: October 12th, 2023

DOI: https://doi.org/10.21203/rs.3.rs-3385435/v1

Additional Declarations: There is **NO** Competing Interest.

DDA1, a novel factor in transcription-coupled repair, modulates CRL4^{CSA} dynamics at DNA damage-stalled RNA polymerase II

Diana Llerena Schiffmacher[1,14], Shun-Hsiao Lee[2,13,14], Katarzyna W. Kliza[3,8], Arjan F. Theil[1], Masaki Akita[1,9], Angela Helfricht[1], Karel Bezstarosti[4], Camila Gonzalo-Hansen[1], Haico van Attikum[5], Matty Verlaan-de Vries[6], Alfred C.O. Vertegaal[6], Jan H.J. Hoeijmakers[1,10,11,13], Jurgen A. Marteijn[1,13], Hannes Lans[1], Jeroen A.A. Demmers[4], Michiel Vermeulen[3,12,13], Titia Sixma[2,13], Tomoo Ogi[7], Wim Vermeulen[1*] and Alex Pines[1*]

1. Department of Molecular Genetics, Erasmus MC Cancer Institute, Erasmus University Medical Center, 3015 CN, Rotterdam, The Netherlands

2. Division of Biochemistry and Oncode institute, Netherlands Cancer Institute, Plesmanlaan 121, 1066CX Amsterdam, The Netherlands.

3. Department of Molecular Biology, Faculty of Science, Radboud Institute for Molecular Life Sciences (RIMLS), Oncode Institute, Radboud University Nijmegen, 6525 GA Nijmegen, the Netherlands

4. Proteomics Center, Erasmus University Medical Center, 3015 CN, Rotterdam, The Netherlands

5. Department of Human Genetics, Leiden University Medical Center, 2333 ZC, Leiden, The Netherlands

6. Department of Cell and Chemical Biology, Leiden University Medical Center, 2333 ZC, Leiden, The Netherlands

7. Department of Genetics, Research Institute of Environmental Medicine (RIeM), Nagoya University, Nagoya, Japan; Department of Human Genetics and Molecular Biology, Graduate School of Medicine, Nagoya University, Nagoya, Japan

8. Current address: Max Planck Institute of Molecular Physiology, Otto-Hahn-Straße 11, 44227, Dortmund, Germany.

9. Current address: Department of Biology and National Centre for Biomolecular Research, Masaryk University, Kamenice 5/A7, Brno, Czech Republic

10. University Hospital of Cologne, CECAD Forschungszentrum, Institute for Genome Stability in Aging and Disease, Joseph Stelzmann Strasse 26, 50931 Köln, Germany.

11. Princess Maxima Center for Pediatric Oncology, Heidelberglaan 25, 3584 CS, Utrecht, the Netherlands.

12. Division of Molecular Genetics and Oncode institute, The Netherlands Cancer Institute, Plesmanlaan 121, Amsterdam 1066 CX, the Netherlands

13. Oncode Institute, The Netherlands

14. These authors contributed equally

* Correspondence: w.vermeulen@erasmusmc.nl and a.pines@erasmusmc.nl

Abstract

Transcription-blocking DNA lesions are specifically targeted by transcription-coupled nucleotide excision repair (TC-NER), which removes a broad spectrum of DNA lesions to preserve transcriptional output and thereby cellular homeostasis to counteract aging. TC-NER is initiated by the stalling of RNA polymerase II at DNA lesions, which triggers the assembly of the TC-NER-specific proteins CSA, CSB and UVSSA. CSA, a WD40-repeat containing protein, is the substrate receptor subunit of a cullin-RING ubiquitin ligase complex composed of DDB1, CUL4A/B and RBX1 ($CRL4^{CSA}$). Although ubiquitination of several TC-NER proteins by $CRL4^{CSA}$ has been reported, it is still unknown how this complex is regulated. To unravel the dynamic molecular interactions and the regulation of this complex, we applied a single-step protein-complex isolation coupled to mass spectrometry analysis and identified DDA1 as a CSA interacting protein. Cryo-EM analysis showed that DDA1 is an integral component of the $CRL4^{CSA}$ complex. Functional analysis revealed that DDA1 coordinates ubiquitination dynamics during TC-NER and is required for efficient turnover and progression of this process.

Introduction

Different DNA damage repair mechanisms and signaling pathways collectively preserve genome stability, protect cells against DNA-damaging agents and are key to maintain proper cellular functioning and thereby counteract both carcinogenesis and aging[1,2]. Among the different DNA repair systems, Nucleotide Excision Repair (NER) stands out for its versatility to remove a broad spectrum of base-pair-disturbing DNA lesions through an intricate multistep process[3-5]. NER removes lesions by two complementary sub-pathways: Global Genome NER (GG-NER) that repairs helix-distorting DNA damage throughout the whole genome, and Transcription-Coupled NER (TC-NER) which removes transcription-blocking DNA lesions (TBLs) in the transcribed strand of active genes and preserves thereby the crucial transcription programs. After damage recognition, the two sub-pathways share the downstream steps of local DNA unwinding, lesion verification, excision of the lesion-containing single-stranded DNA, followed by restoration of the strand by DNA synthesis and ligation[3-5].

TC-NER is initiated by stalling of elongating RNA polymerase II (RNAPII) onto DNA lesions[6,7], which triggers binding of Cockayne syndrome B protein (CSB), a member of the SWI2/SNF2 family[8]. While, CSB normally interacts transiently with RNAPII for monitoring progression and to facilitate the translocation over intrinsic pausing sites and smaller lesions, upon encountering helix-disturbing TBLs, CSB becomes firmly bound to RNAPII[7] and enables further assembly of the other TC-NER core factors CSA and UVSSA[3-5]. CSA is a WD40-domain-containing protein that belongs to the DCAF (DDB1- and CUL4-associated factors) family[9] and is the substrate receptor subunit of the DDB1, CUL4A/B and RBX1 containing cullin-RING ubiquitin ligase complex ($CRL4^{CSA}$)[10,11]. The activity of this ligase is activated by the NEDD8 conjugation to CUL4 and negatively regulated by the COP9 signalosome (CSN) complex[12]. Upon UV-light-induced DNA damage, $CRL4^{CSA}$ gets activated and ubiquitinates different TC-NER-associated substrates, including RNAPII[13], UVSSA[14] and CSB[15]. The CSA-dependent CSB ubiquitination is counteracted by the broad-spectrum de-ubiquitinating enzyme USP7 which is recruited to the TC-NER complex by UVSSA[16,17]. UVSSA itself is also ubiquitinated at Lysine 414, to facilitate TFIIH recruitment and promote RNAPII ubiquitination[13,14,18]. Additionally, previous studies have also shown that other ubiquitin ligases and ubiquitin-chain editing enzymes are implicated in differential RNAPII ubiquitination[4]. These complex and dynamic ubiquitination events on RNAPII were proposed to determine the fate of lesion-stalled RNAPII, that either drive the timely association and likely also dissociation of the TC-NER factors, or are implicated in the removal and degradation of lesion-stalled RNAPII, or control genome-wide dissociation of promotor-paused RNAPII in response to TBLs[13,14,19]. Recently, the structure of human elongating RNAPII bound by CSB, $CRL4^{CSA}$ and UVSSA was resolved using cryo-electron microscopy (cryo-EM) and has provided important structural information on how the elongating RNAPII complex is converted into a TC-NER complex which forms the basis for coupling transcription to DNA repair in human cells[20].

Although CSA has been studied extensively for many years and valuable insight into the molecular interactions and possible ubiquitination targets have been obtained, we still know very little about how the $CRL4^{CSA}$ is controlled and interconnected with the repair machinery at DNA damage-stalled RNAPII. To study this, we applied a mass spectrometry approach using a fluorescently tagged CSA knock-in (KI) cell line and identified DDA1[21] as an important binding partner of CSA. DDA1 is a core subunit of multiple, though not all, Cul4-based E3 ligases[22]. We showed that DDA1 is an integral component of the $CRL4^{CSA}$ complex and that it coordinates the $CRL4^{CSA}$ complex activity and facilitates TC-NER progression. Our findings suggests that not only a highly controlled cooperative assembly, but also a timely turnover of TC-NER proteins is important in regulating the progression of DNA repair to preserve the transcription program integrity.

Results

Generation and characterization of CSA-mClover knock-in cells

How $CRL4^{CSA}$ operates and controls TC-NER is presently matter of debate[13,19]. Further information on $CRL4^{CSA}$ functioning might be provided by defining the composition of this protein complex. To comprehensively chart the CSA interactome in human cells, we applied biochemical techniques in concert with quantitative mass spectrometry (MS)[23] using Stable Isotope Labelling by Amino acids in Cell culture (SILAC)[24]. To efficiently isolate CSA containing complexes, we generated a homozygous CSA knock-in HCT116 cell line by CRISPR-Cas9-mediated genome editing[25], that expresses a fluorescently tagged version of endogenous CSA. mClover DNA, a modified version of GFP[26], was inserted at the 3' end of the CSA gene. Sequencing confirmed the proper in frame integration of the mClover tag and immuno-blot analysis showed that CSA-mClover is expressed at equal levels as non-tagged CSA in the parental cell line (supplementary Figure 1 A-B). Colony Survival, revealed that the CSA-mClover knock-in cells (hereafter CSA-mC KI) were equally resistant to UV-C light (hereafter UV)-induced DNA damage as the cognate parental wild-type HCT116 cells, in contrast to the highly UV-sensitive CSA HCT116 knock-out cells (supplementary Figure 1 C). Moreover, Recovery of RNA Synthesis[27] (RRS) analysis by 5-EU labelling after UV irradiation (supplementary Figure 1 D), showed that the TC-NER activity is not affected by the mClover tag. To further validate the CSA-mC KI cell line, we performed fluorescence redistribution after photobleaching[28] (FRAP). In this assay, fluorescent proteins are photobleached in a narrow strip spanning the cell nucleus by a high-intensity laser pulse. The subsequent fluorescence redistribution is monitored in time, providing a measure for the protein's mobility and to dissect different kinetic pools, *e.g.* free diffusing and/or chromatin-bound fractions in living cells. FRAP experiments showed a markedly reduced fluorescence recovery of CSA-mClover after 10 J/m^2 of UV irradiation, indicative for binding (immobilization) of CSA-mClover to chromatin-bound lesion-stalled RNAPII (supplementary Figure 1 E). This UV-induced immobilization was absent in presence of transcription inhibitor THZ1. Importantly, UV-induced CSA-mClover immobilization is completely reverted to the pre-UV-damaged situation 10 h after UV (supplementary Figure 1 F). Both the transcription dependency and reversion of immobilized CSA-mClover 10 h after UV, when most TBLs are repaired, clearly indicate that this immobilization reflects active participation in TC-NER. Together these TC-NER activity assays demonstrate that the generated CSA-mC KI cell line is a *bona fide* and highly sensitive tool to study the binding kinetics of CSA in TC-NER and provides a valid source to capture CSA-associated proteins.

MS analysis revealed DDA1 as an interaction partner of CSA

Here we used the mClover (GFP derivative) tag as bait for affinity purification to isolate protein complexes by a simple, single-step affinity purification protocol employing GFP-Trap beads[29]. CSA-mC KI cells were mock treated or irradiated with UV and the CSA-mClover-containing protein complex(es) were isolated by immuno-precipitation and identified by LC-MS. This methodology is based on stringent washing conditions coupled with highly selective and specific GFP-bead purification to obtain stable complexes of significant purity for MS analysis[30,31]. SILAC analysis under non-damaging conditions, comparing CSA-mC KI with the parental HCT116 cells, identified known CSA-specific interacting proteins[11]. These include, the CRL complex subunits, all subunits of the COP9 signalosome and the chaperonin complex TRiC, previously shown to be essential for proper CSA incorporation into the CRL complex[32] (Figure 1 A).

Surprisingly, CSB appeared already associated with $CRL4^{CSA}$ even in the absence of exogenously induced TBLs, suggesting that either a fraction of CSA and CSB are already connected prior to their binding to lesion-staled RNAPII or that in non-UV-challenged cells TC-NER is continuously active

towards endogenously induced TBLs. We similarly examined the changes in the CSA interactome upon UV irradiation by comparing mock-treated and UV-treated CSA-mC KI cells. Numerous previously described TC-NER interacting proteins were identified[33,34], including several RNAPII subunits and RNAPII-associated factors, PAF-1 complex and the transcription factor II H (TFIIH) complex, validating the screen (Figure 1 B). In addition, we identified the DET1 and DDB1 Associated protein 1 (DDA1) as a constitutive interacting component of $CRL4^{CSA}$ (Figure 1 A-B and supplementary Table1) both in the presence and absence of UV-induced DNA damage. Immuno-blot analysis of CSA-mClover pulldowns from both CSA-mC knock-in and CSA-GFP overexpressing cell lines confirmed the interaction of CSA with the CRL (CUL4A and DDB1), COP9 (CSN5), TC-NER (CSB), and the TRiC (TCP-1) complex and validated the specific interaction between CSA and DDA1 (Figure 1 C and supplementary Figure 2 A). DDA1 was previously identified as a subunit of several CRL4-based E3 ligase complexes[22], but remarkably was not found associated with the $CRL4^{DDB2}$, which is involved in DNA damage recognition within GG-NER, and is structurally comparable to $CRL4^{CSA}$ [10]. To further investigate the selectivity for $CRL4^{CSA}$, we generated GFP-DDB2 HCT116 knock-in cells by inserting a GFP tag at the N-terminus of DDB2 locus. These cells were validated by immune-blot analysis, UV colony survival and FRAP analysis (supplementary Figure 2 B-C). Pulldown of GFP-DDB2 from these cells followed by both immune-blot and LC-MS analysis, (Figure 1 C, supplementary Figure 2 D and supplementary Table2) confirmed that DDA1 could not be detected in $CRL4^{DDB2}$ complexes. It should be noted, however, that the absence of DDA1 identification within $CRL4^{DDB2}$ does not fully prove its absence in this complex as it might associate sub-stoichiometric or only transiently.

DDA1 is a component of the CSA/DDB1 complex

To investigate the binding of DDA1 to CSA, we assembled part of the TC-NER ubiquitin ligase complex and determined its structure by cryo-EM at 3.4 Å resolution (Figure 2 A-E and supplementary Figure 3). The complex contains CSA-DDB1-DDA1, the substrate recognition module of $CRL4A^{CSA}$, together with K414 mono-ubiquitinated UVSSA[13] and the catalytic inactive deubiquitinating enzyme USP7 ($USP7^{C223A}$). The two WD40 domains of DDB1 (BPA and BPC) and CSA as well as the N-terminal region of DDA1 were well resolved, whereas the third WD40 domain of DDB1 (BPB) has multiple orientations relative to the other domains of DDB1. After focused refinement, the VHS domain of UVSSA was also well defined and its interaction with CSA was found similar to that in a recently published cryo-EM structure (PDB 7OO3)[20] (Figure 2 B-D). However, USP7 and the rest of UVSSA showed high heterogeneity and the USP7 structure could not be resolved even after various attempts at local processing.

In this structure we found DDA1 to interact with both DDB1 and CSA. The DDA1 interaction with DDB1 is similar to previous structures: the DDB1-DDA1 complex (PDB 6DSZ) and the RBM39-DCAF15-DDB1-DDA1 complex (PDB 6Q0W, 6UD7, 6PAI)[35-38], involving residues 2-75 of DDA1. The interaction of DDA1 with CSA is in a similar area of this DCAF as the DDA1 interaction with DCAF15, but the details are different, as DDA1 has clearly rearranged itself. In the DCAF15-DDA1 complex, DDA1 forms an α helix from residue 53 to 73, creating a binding interface that complements an extensive groove of DCAF15. The DDA1 binding groove of DCAF15 is not conserved in CSA (supplementary Figure 4 A-B) and we did not observe the full helix in the interaction with CSA. Instead, low resolution densities were identified around blades 4 and 5 of the CSA β propeller. We could visualize DDA1 up to residue 62, but the region where it binds to CSA was poorly resolved and we could not build any model with confidence (Figure 2 D-E). By applying a mask and focused processing, we found that the densities in this area adopt multiple conformations, suggesting that the interaction is at low affinity and transient. We hypothesize that in order to be able to interact with various targets, DDA1 has adopted unique interactions with different DCAF subunits.

To better understand the role of DDA1 in the complex, we tested its effect on thermal stability of the complex using nano-differential scanning fluorimetry. Addition of DDA1 conferred a modest but reproducible stabilization of one degree in melting curve analysis compared to CSA-DDB1 alone (Supplementary Figure 4 C-D), which is somewhat less than its effect on the DCAF15 DDB1 complex[36]. This result suggests that DDA1 plays a structural and possible stabilizing role in the $CRL4^{CSA}$ complex, which may be required to provide sufficient dynamics of the complex.

DDA1 is required for transcription recovery following DNA damage

$CRL4^{CSA}$ is a crucial TC-NER factor to resolve TBLs and the subsequent resumption of transcription arrested by DNA damage. To investigate the significance of DDA1 for the $CRL4^{CSA}$ function in TC-NER we tested the effect of its absence (DDA1 KO, Figure 3 A) on CSA and CSB stability, UV-survival and recovery of RNA synthesis (RRS) after UV treatment, which is a proxy for TC-NER activity[27]. The levels of CSA and CSB protein were unaltered in total extracts isolated from DDA1 KO cells compared to the parental cell line (Figure 3 A), revealing that DDA1 loss does not affect the stability of CSA and CSB. DDA1-KO cells showed a clear RRS defect (Figure 3 B) after 10 J/m^2 UV irradiation, similar to CSA and CSB KO cells. However, in contrast to this strong RRS defect, DDA1 KO cells were only moderately sensitive to UV irradiation when compared to CSA and CSB KO cells, as measured by colony survival assay (Figure 3 C). Strikingly, at lower UV doses the DDA1-dependent UV sensitivity was not even significantly distinct from WT cells and became only apparent at higher doses. We speculated that this moderate sensitivity of DDA1-KO cells at low doses of UV would correlate to a similar mild effect on RNA synthesis resumption at lower UV doses. Indeed, RRS did not appear to be affected at lower doses of 2.5 and at 5 J/m^2 UV in DDA1 KO cells and became only noticeable at a higher dose of 10 J/m^2 (Figure 3 D). These data suggest that the crucial role of DDA1 in TC-NER becomes apparent at higher UV doses, when more functional CSA-containing complexes are likely required. Importantly, the ectopic expression of DDA1 in DDA1 KO cells did rescue the resumption of transcription (supplementary Figure 5 A), indicating that the observed phenotypes are directly associated to the DDA1 protein.

DDA1 is required for proper CSA localization

Previously, we found that the TRiC chaperonin is required for proper folding, stability and incorporation of CSA into the CRL4 complex and its subsequent nuclear localization, essential for optimal performance of the $CRL4^{CSA}$ complex in TC-NER[32]. In contrast to TRiC, DDA1 does not seem to be necessary for CSA's stability (Figure 3A). However, immuno-fluorescent analysis of endogenous CSA showed that in the absence of DDA1, CSA is not exclusively localized to the nucleus and shows increased levels in the cytoplasm as compared to wild-type and CSB KO cells, assayed in parallel (Figure 4 A-B). This observation was confirmed by siRNA against DDA1 in cells ectopically expressing GFP-tagged CSA, showing that loss of DDA1 triggers mislocalization of CSA (supplementary Figure 5 B-C). Moreover, expressing GFP-tagged DDA1 in the DDA1-KO cells not only restored the resumption of transcription after UV-induced inhibition (supplementary Figure 5 A) but also rescued the subcellular localization of CSA (supplementary Figure 5 E). Interestingly, absence or depletion of DDA1 did not affect nuclear localization of endogenous DDB2 nor ectopically expressed GFP-tagged DDB2 (Figure 4 A-B and supplementary Figure 5 D). Together the data showed that DDA1 specifically modifies $CRL4^{CSA}$ without affecting the similar GG-NER-specific $CRL4^{DDB2}$ complex.

This partial CSA nuclear localization in DDA1-deficient cells may be causative for the observed TC-NER defect. It is thus expected that, by restoring the correct cellular compartmentalization of CSA, the repair capacity could be complemented. Strikingly however, expression of GFP-CSA fused to an array

of three nuclear localization signals (3-NLS), CSA-GFP-3-NLS (supplementary Figure 5 F) in DDA1 KO cells did not rescue the transcription resumption in response to UV irradiation (Figure 4C), despite that the addition of 3-NLS to CSA provided full nuclear localization. These experiments strongly suggest that the TC-NER defect in DDA1KO cells is associated to another, thus far unidentified, molecular mechanism rather than to a reduced nuclear protein level of CSA.

DDA1 modulates the protein network of CRL4^{CSA} complex

To further assess how DDA1 is linked to CRL4^{CSA} function, we examined whether the loss of DDA1 would affect the protein-network of CSA. To that aim, we immunoprecipitated CSA-mClover from WT KI and DDA1 KO (CSA-mClover KI) cell lines after UV irradiation followed by MS applying the Data Independent Acquisition[39] (DIA) and label free quantification (LFQ) approach[40]. DIA is a recent MS approach which provides high sensitivity with unprecedented proteome coverage[41] (supplementary Table 3). MS comparison between CSA-mClover and non-expressing control cells (supplementary Figure 6 A-B) recapitulated our previous MS results (Figure 1), substantiating these and our earlier observations[32]. We observed a stronger interaction of CSA with RNAPII, PAF-complex, CSB, UVSSA and the CRL and COP9 complexes after UV induced DNA damage in cells lacking DDA1 (Figure 5 A). This increased interaction might be caused by the reduced TC-NER activity in the absence of DDA1 in which factors still assemble but remain associated. However, even without DNA damage and despite part of CSA roaming in the cytoplasm, we noted a stronger interaction of CSA with CSB, UVSSA and the core subunits of the CRL and the COP9 complexes (Figure 5B), suggesting that DDA1 is affecting the protein network of the CRL4^{CSA} complex already under basal conditions. The interaction of CSA with TRiC complex were unchanged and not affected by UV or loss of DDA1 (supplementary Figure 6 C). These data suggest that in the absence of DDA1 there is either an imbalance in complex assembly, or, due to the diminished nuclear presence of CSA, a larger proportion of CRL4^{CSA} is engaged in TC-NER in response to endogenously produced TBLs, or, alternatively, DDA1 is involved in the dynamic turnover of the CRL-COP9 complex and in partial pre-assembled TC-NER complex.

CSA- and DDA1-dependent ubiquitination

The cellular response to UV irradiation triggers a series of ubiquitination events that facilitate TC-NER progression in which the CRL4^{CSA} complex[13,14] plays an important role together with other ubiquitin ligases[42-44]. To investigate whether the impaired TC-NER performance in DDA1 KO cells is related to altered CRL4^{CSA} ubiquitination activity by its increased association with the inhibitory COP9 subcomplex, we conducted global UV-induced ubiquitin signaling profiling by SILAC-based MS in WT, CSA KO and DDA1 KO cell lines. Ubiquitinated peptides were enriched by immunoaffinity purification using an antibody bound to a resin that specifically recognizes diglycine-modified peptides (K-GG)[45], generated by tryptic digestion of ubiquitin-modified proteins. We performed, in duplicate, three separate experiments in each of which Light- and Heavy-SILAC cells were mock or UV treated (supplementary Fig. 7A). In addition, we also compared WT cells with either CSA or DDA1 KO cells without external DNA damage induction to identify possible basal or intrinsic CSA-, and DDA1-dependent ubiquitination activity. Together, this led to the identification of 23,054 unique ubiquitin sites, which were reduced to 17,697 unique sites after stringent filtering (supplementary Figure 7 A, supplementary Table 4). The ubiquitinome coverage distribution plot showed similar quantification depths for all conditions and good reproducibility between experimental duplicates (supplementary Figure 7 B-C, supplementary Figure 8 A-E, supplementary Figure 9 A-C).

To identify UV-activated pathways, we focused on proteins containing ubiquitin sites found in both duplicates in at least one of the tested cell lines after UV irradiation. The application of a threshold filter

of 2-fold change (FC) provided us 401 UV-induced ubiquitin sites, which were subjected to ingenuity pathway analysis (IPA)[46]. As expected, UV irradiation induced a strong activation of DDR manifested by the significant enrichment of NER pathway components among these sites (Figure 5 C). Additionally, K6-linked ubiquitin chains were substantially increased, in contrast, the levels of K48 and K63 were almost unaltered after UV (Figure 5 E), in line with previous observations[47,48], which validated the applied procedure and obtained results. Strikingly, no prominent overall changes were detected in UV-activated pathways between WT, CSA KO and DDA1 KO cell lines.

For an in-depth comparison of the ubiquitination responses upon UV irradiation among WT, CSA KO and DDA1 KO cell lines, we examined ubiquitin-sites which were quantified in all 6 UV experiments (4324 unique ubiquitin sites) and we applied a threshold filter of 2-FC, resulting in 49 ubiquitin sites found to be commonly responding upon UV irradiation (Figure 5 D). We also observed specific ubiquitin-peptides in CSB and UVSSA, which were previously identified as important UV-induced ubiquitination targets[14,15], however, they were not consistent among the experiments (i.e K414 in UVSSA, supplementary Figure 9 A-C, and supplementary Table 4), This inconsistency makes it challenging to draw definitive conclusions. However, it is possible that the CSB and UVSSA ubiquitination are a highly dynamic phenomenon, occurring in a specific or short time window during TC-NER, which may not be easily captured by our procedure at the set time after UV-irradiation. To further investigate the role of DDA1 we performed *in vitro* ubiquitination assays with CSB, UVSSA and neddylation activated CRL4^{CSA} complex with and without DDA1 (Supplementary Figure 10 A-C). Under those conditions, we observed robust and fast polyubiquitination of CSB and mono-ubiquitination of UVSSA, showing that indeed CSA is capable to ubiquitinate CSB and UVSSA. These data further suggest that DDA1 is not essential for the E3 ligase CRL4^{CSA} activity on CSB and UVSSA *in vitro*. However, in cells, the CRL4^{CSA} ubiquitination activity is negatively regulated by the COP9 signalosome through its capacity to remove the CRL-activating Nedd8 from Cul4[12,49]. Since we noted that in non-treated conditions (Figure 5 B) CSA is stronger associated with CSB, UVSSA, CRL and the COP9 complex in DDA1 KO cells, it might be expected that the ubiquitin profile is already altered in absence of exogenous DNA damage. Indeed, ubiquitin profiling of DDA1 KO cells without exogenous DNA damage showed that a striking large number of ubiquitin sites and pathways were differentially regulated in the absence of DDA1 (Figure 6 A), endorsing our hypothesis. Among the pathways that were affected without exposure to exogenous genotoxic agents, also several DDR-associated processes, including NER, were identified. This DDA1-dependent alteration of the ubiquitin signaling profile, suggests that DDA1, potentially through its role in CRL4^{CSA}, is required to maintain cellular homeostasis even without exposure to exogenous DNA damaging agents. Similar significant pathway changes were observed in non-irradiated CSA KO cells, corroborating that DDA1-function within CRL4^{CSA} is already effective under basal conditions, *i.e.* without exposure to exogenous DNA damaging agents.

Our findings indicate that under non-damaging conditions several pathways were affected in the absence of either DDA1 or CSA, ranging from DDR-associated signaling, mRNA processing, translational mechanism, mitochondrial function and protein folding/stability processes. Strikingly, with previous gene expression profiling analysis similar biological pathways were found to be altered during aging, in NER-deficient mouse cells and upon low doses of UV-exposure[50]. Further in-depth analysis has provided evidence that these altered gene expression profiles were mainly caused by transcription stress, induced by endogenous DNA damage[51]. It is thus conceivable that CRL4^{CSA}, including DDA1, is activated by the presence of endogenous DNA damage.

Differential ubiquitination of RNA Polymerase II

We also observed specific ubiquitination of RNAPII's subunit RPB1/POLR2A (K177, K853, K1268 and K1350) after UV irradiation (Figure 5 F), in line with earlier studies[13,19]. Unexpectedly, we found that the SILAC ratio of UV-induced K1268 ubiquitination of RNAPII is only slightly decreased in the full absence of CSA. This specific ubiquitination site was previously identified as a focal point for coordinating TC-NER, protein assembly and signaling RNAPII for degradation and essential for surviving genotoxic insults[13,52,53]. Since we observed multiple CSA/DDA1-dependent ubiquitination events in the absence of exogenous DNA damage (Figure 6 A and discussed above) we further specifically focused on the RPB1 ubiquitination sites. Strikingly, we observed a clearly reduced RPB1-K1268 ubiquitination in CSA KO and less prominent reduction in DDA1 KO cells compared to isogenic WT control cells under non-damaging conditions. On the other hand, other known UV-responsive ubiquitin sites on RPB1, K853 and K1350 were not affected (Figure 6 B) by loss of CSA or DDA1 in absence of exogenous DNA damage. Importantly, the protein level of RNAPII was not changed, as deduced from the global protein profile determined by MS using the same input material applied for the detection of diglycine-modified peptides (Figure 5 F, Supplementary Table 5). Hence, it appears that CRL^{CSA} constitutively ubiquitinates this lysine residue 1268 in RPB1, a process crucial for the progression of TC-NER, which seems to be modulated by DDA1. The precise biological role of this constitutive ubiquitination at RPB1 K1268 remains elusive, especially considering that mice carrying this mutation do not exhibit evident phenotypic changes in the absence of externally induced TBLs[13]. We can only speculate on the trigger for this CRL^{CSA}-mediated activity, which may arise from the persistent albeit low levels of TBLs by endogenous sources of DNA damage[54-56] (*i.e.* cellular metabolites such as ROS or aldehydes).

It should be noted, however, that the UV-induced ubiquitin profiling reveals relative differences in RPB1 K1268 ubiquitination rather than absolute values. We thus speculate that the previous proposed essential role of CSA to ubiquitination RPB1-K1268 in response to UV-irradiation is, in part, explained by the intrinsic reduced K1268 ubiquitination in the absence of exogenous DNA damage when compared to WT cell (Figure 6 B). Although the majority of RPB1 K1268 ubiquitination is CSA dependent, it is also likely that a part of the TBL-induced RPB1 ubiquitination may occur by a CSA independent event.

DDA1 controls $CRL4^{CSA}$ activity via the COP9 complex

$CRL4^{CSA}$ activity appears important for the basal level of RNAPII ubiquitination, thereby also significantly reducing the overall ubiquitination response to UV-induced TBLs. However, Vidaković et al., suggested that the CSA-dependent RPB1 K1268 ubiquitination became mainly apparent at later time-points post UV[19]. In this scenario, the role of DDA1 as modulator of CSA, would become more evident in the TC-NER process at later time-points. Since we observed that absence of DDA1 partly impairs the RPB1-K1268 ubiquitination, though not to the same extent as absence of CSA, we investigated whether the loss of DDA1 would affect the dynamic association of CSA-mClover with the TC-NER machinery by live cell imaging. CSA rapidly accumulated at the site of UV laser-induced DNA damage and was not influenced by the absence or presence of DDA1 (Figure 6 C), indicating that TC-NER complex assembly is not affected. FRAP analysis of CSA-mClover, shortly after UV-irradiation also showed that immobilization of CSA, reflecting binding to lesion-stalled RNAPII, was not changed by the absence of DDA1. However, FRAP analysis at a later time point, *i.e.* 10 h post UV, showed that a significant fraction of CSA-mClover molecules remained immobilized in DDA1 KO cells, whereas in WT cells the mobility was fully recovered to the same level as in undamaged cells (Figure 6 D, supplementary figure 11 A). These data suggest that in the absence of DDA1, CSA

molecules were longer bound to lesion-stalled RNAPII. This was confirmed by immunoprecipitation of CSA-mClover and immunoblot analysis (Figure 6 E), showing that the interaction between CSA and RNAPII was still evident 10 h after UV-irradiation in absence of DDA1, whereas in WT cells this was not observed. This reduced clearance of CSA-mClover from lesion-stalled RNAPII can either be caused by a reduced repair rate (longer presence of TBLs) or a slower disassembly of regulatory subunits from the $CRL4^{CSA}$ complex. The latter option is in line with the increased interaction between $CRL4^{CSA}$ with the COP9 complex in absence of DDA1 in UV irradiated, but also in mock treated as detected by MS (Figure 5 A-B). These data suggest an intrinsically slower disassembly of the $CRL4^{CSA}$-COP9 complex when DDA1 is absent. We speculate that this aberrant complex turnover might be related to a compromised $CRL4^{CSA}$ activity in which the presence of COP9 complex may physically interfere with its activity.

CRL is activated by NAE1, which conjugates the ubiquitin-like NEDD8 to CUL4. The covalent attachment of NEDD8 induces a conformational change of CUL4, thereby promoting polyubiquitination of its substrates. However, the CRL-associated COP9 complex keeps $CRL4^{CSA}$ in a dormant state by removing Nedd8 from CUL4. Regulation of CRL activity is thus achieved by a delicate balance between activating and de-activating modalities. Disturbance of this balance or increase association with COP9 complex, as in the absence of DDA1, may thus interfere with a timely activation/inactivation cycle of the complex. To gain insight into the molecular events that mediate $CRL4^{CSA}$ activity and the TC-NER progression, we inactivated this complex with the broad class neddylation inhibitor, MLN4924[57] (NAEi). NAEi treatment triggers accumulation of the deneddylated, inactive isoform of the complex, mimicking its partial inactivation by increased COP9 association caused by DDA1 absence. The inhibitor treatment completely prevented CSA mobility to return to the same level as in non-damaged cells 10 h after UV irradiation, similarly, though stronger, as observed in DDA1 KO cells (Figure 6 F, supplementary figure 11 B). Altogether, these results further support the idea that DDA1 is important for the molecular coordination and dynamics of the $CRL4^{CSA}$ by tuning the COP9 complex interaction.

Discussion

Mechanistically how $CRL4^{CSA}$ drives TBLs removal and its significance for transcription maintenance is still unclear. Although the $CRL4^{CSA}$ E3 ligase structure is well defined, the identification and characterization of its interacting DDA1 factor revealed a more complex organization, in which DDA1 plays an important role in promoting resolution of TBLs, by modulating the $CRL4^{CSA}$ ubiquitinating activity to control transcription-coupled repair. Our study reveals an unexpected complexity of how regulatory ubiquitination orchestrates the progress of TC-NER.

CRL4s are a large family of E3 ligases in which DDB1-CUL4 associated factors (DCAF) are receptors to identify a great number of specific substrate proteins[58]. DDA1 is a core subunit of multiple, but not all, CRL4 complexes. Remarkably, DDA1 was not found to be associated with or extremely dynamic bound to the CRL^{DDB2} and its absence did not influence DDB2's nuclear localization nor its function in GG-NER. This finding is intriguing, since the overall architectures of both $CRL4^{DDB2}$ and $CRL4^{CSA}$ E3 ubiquitin ligase complexes appear very similar[10], although the major differences in enzymatic activity is defined by the WD40 domain of each DCAF. This domain coordinates the CRL4-E3 ligase activity by functioning as interaction platform for the binding of specific proteins to diversify the substrate range. Our findings suggest that each DCAF has to adopt a strategy to deal with DDA1, providing an opportunity for a more subtle regulation of the CRLs. Indeed, we have found that the adding of DDA1 to CSA/DDB1 complexes *in vitro* confers a modest stabilization, in contrast to a more stabilizing effect

for DCAF15/DDB1 where a DDA1-binding groove is present[35-38]. Precisely how DDA1 modulates the overall topology of the fully assembled CRL4–substrate complex remains to be established.

CSA is regulated by several factors, including the chaperonin TRiC[32], which provides properly folded CSA to DDB1. We previously showed that the TRiC complex is required for CSA stability and to facilitate its assembly into the $CRL4^{CSA}$ complex, which can then efficiently translocate into the nucleus. Mutant CSA proteins, with likely exposed hydrophobic patches lead to enhanced interaction with TRiC and cause cytoplasmic retention of CSA. Although we found that DDA1 promotes nuclear localization of CSA, quantitative MS and immunoblot revealed that DDA1 did not affect the level of CSA protein nor the interaction between CSA and TRiC, suggesting that the cellular localization of CSA in DDA1 KO cells is not connected with the CSA folding, stability and with the hand-over mechanism for the formation of $CRL4^{CSA}$ complex. Based on these observations, it is tempting to speculate that loss of DDA1 may cause insufficient nuclear presence of CSA to fully support TC-NER at high loads of TBLs, even though the majority of the $CRL4^{CSA}$ complex is still nuclear. Most notably in this regard, is that a tagged version of CSA fused with a tandem of three nuclear localization signals failed to rescue the TC-NER defect in DDA1 KO cells. These observations suggest that the TC-NER-deficient phenotype is not only caused by a reduced nuclear protein level of CSA.

Importantly, we provide direct evidence that DDA1 controls the disassembly or dissolution of the TC-NER complex. Indeed, the mobility of CSA was impaired in DDA1 KO cells which correlates with a stronger interaction between $CRL4^{CSA}$ and the COP9 complex, and subsequently association with chromatin-bound RNAPII. Our findings suggest that loss of DDA1 affects the dynamic activation-deactivation cycle of $CRL4^{CSA}$ through controlling the association of the COP9 complex. By serving as ubiquitination controlling factor, DDA1 subsequently promotes the progress of the repair of DNA-damage-stalled RNAPII. We envisage a scenario in which the regulatory ubiquitination of RNAPII at TBLs is not only maintained by $CRL4^{CSA}$, but also involves other E3 ligases. The function of $CRL4^{CSA}$ may not be only to cooperate with other E3 ligases to trigger ubiquitination of RNAPII, but also to amplify, propagate and stabilize the initial ubiquitination events to coordinate the TC-NER process. The strongly altered ubiquitin profile in both CSA and DDA1 KOs in absence of external DNA damage may be explained by the continuous induction of TBLs from endogenous sources that may trigger activation of transcription-coupled repair processes. In conclusion, our findings reveal that DDA1 is an important factor in regulating the progression of DNA repair, and it will be very interesting to gain structural insights into TC-NER including DDA1 as a core component of $CRL4^{CSA}$ complex.

1. MATERIAL AND METHODS

REAGENT or RESOURCE	SOURCE	IDENTIFIER
gRNA and Primers		
sgCSA exon 12 (5'-TGTATGGTCTATTCCTGACA-3')	Integrated DNA technologies	N/A
Primer FW CSAKI (5'-GGAGCAGCAGTGATGAAGAAGGA-3')	Integrated DNA technologies	N/A
Primer RV CSAKI (5'-'GGATAGTAGGAGACATTGAGCCCC-3')	Integrated DNA technologies	N/A
sgDDA1 exon 2 (5'-GGACTCCGTGTGCAAAGCCT-3')	Integrated DNA technologies	N/A
sgDDA1 exon 3 (5'-GCAGGTAGACTGAGGGCCGT-3')	Integrated DNA technologies	N/A
Primer FW DDA1 KO (5'-GGGATGTGCACATAGCCTGGCC-3')	Integrated DNA technologies	N/A
Primer RV DDA1 KO (5'-TTTGCCTGGACCCCCTTCCCAT-3')	Integrated DNA technologies	N/A
sgCSB exon 2	[31]	N/A
sgCSA exon 3 and 7	[31]	N/A
sgDDB2 exon 1 (5'-CCTTCACACGGAGGACGCGA-3')	Integrated DNA technologies	N/A
Primer FW DDB2 KI (5'-GTCCCATCTACTTAGGAGGC-3')	Integrated DNA technologies	N/A
Primer RV DDB2 KI (5'-TTCAAGCCCCAGTAAACCTC-3')	Integrated DNA technologies	N/A
siRNA DDA1 (1) (5'-GAAGAGAGACCAGGAGCAAUU-3')	Thermo Scientific Dharmacon	N/A
siRNA DDA1 (2) (5'-CAGAUCAUCGUGACAGAAAUU-3')	Thermo Scientific Dharmacon	N/A
siRNA Control	[59]	N/A
Vectors and DNA		
CSA-GFP (DNA)	[32]	N/A
CSA-GFP-3NLS (DNA)	This paper	N/A
GFP (DNA)	[32]	N/A
GFP-3NLS (DNA)	This paper	N/A
GFP-DDA1 (DNA)	GenScript	N/A
GFP-DDA1 (DNA)	GenScript	N/A
His_6-DDB1 (DNA)	Integrated DNA technologies	N/A
His_6-UVSSA (DNA)	Integrated DNA technologies	N/A
mClover (DNA)	GenScript	N/A
pAC8-CSA-Strep II	[10]	N/A
pcDNA3-HA2-ROC1 (RBX1)	Addgene[60]	19897
pcDNA3-myc3-CUL4A	Addgene[61]	19951
pETNKI	[62]	N/A

pFastBac-HA-CSB-His_6	[63]	N/A
pGEX-6p1-$USP7^{C223A}$	[64]	N/A
pGEX-APPBP1-UBA3	[65]	N/A
pGEX-NEDD8	[65]	N/A
pGEX-UBE2M	[65]	N/A
pLenti-CMV-puro-DEST plasmid	Addgene[66]	17452
pLentiCRISPR.v2	Addgene[67]	52961

Antibodies

Alexa Fluor ® 647 Phalloidin	Life Technologies Europe BV	A22287
Alexa Fluor 488 (rabbit)	Invitrogen	A11008
Alexa Fluor 594 (mouse)	Invitrogen	A11005
Alexa Fluor 594 (rabbit)	Invitrogen	A21207
Goat anti-mouse CF™ IRDye 680	Sigma-Aldrich	sab4600199
Goat anti-rabbit CF™ IRDye 770	Sigma-Aldrich	sab4600215
Mouse anti-CSN5	Novus biologicals	NB120-495
Mouse anti-TCP-1	Abnova	H00006950-M01
Mouse anti-Tubulin (B512)	Sigma-Aldrich	T5168
Rabbit anti- Rpb1 NTD	Cell Signaling Techn	14958
Rabbit anti-CSA	Abcam	ab240096
Rabbit anti-CSA	Abcam	ab137033
Rabbit anti-CSB	antibodies-online.com	ABIN2855858
Rabbit anti-CUL4A	Santa Cruz	sc-293
Rabbit anti-DDA1	antibodies-online.com	ABIN2798422
Rabbit anti-DDB1	Novus biologicals	NBP2-75465
Rabbit anti-GFP	Abcam	ab9194
Rabbit anti-H2B	Millipore	07-371

Bacterial strains

One Shot™ Top10 Chemically competent cells	Invitrogen	C4040-06

Chemicals, peptides, and recombinant proteins

[$^{12}C_6$,$^{14}N_4$]-arginine	Silantes	201003902
[$^{12}C_6$]-lysine	Silantes	211004102
[$^{13}C_6$,$^{15}N_4$]-arginine	Cambridge Isotope Laboratories	CNLM-539-H-1
[$^{13}C_6$]-lysine	Cambridge Isotope Laboratories	CNLM-291-H-1
2× Laemmli sample buffer	Sigma-Aldrich	S3401
4′,6-diamidino-2-phenylindole (DAPI)	Sigma-Aldrich	D9542
5-Ethynyl-uridine (5-EU)	Axxora	JBS-CLK-N002
Acetic acid	Sigma-Aldrich	33209-M
Acetonitrile	Sigma-Aldrich	271004
Aqua-Poly/Mount	Polysciences, Inc.	18606-20
Ascorbic Acid	Sigma-Aldrich	209198
Atto 594 Azide	Atto Tec	AD594-105
Benzonase® Nuclease	Novagen/Millipore	70664

Bovine Serum Albumin (BSA)	Sigma-Aldrich	A3294
Briljant Blue R	Sigma-Aldrich	B-0149
$CuSO_4*5H_2O$	Sigma-Aldrich	A0278
Dialyzed fetal calf serum	Gibco	26400044
Dithiothreitol (DTT)	ThermoScientific	R0861
DMEM for SILAC	ThermoScientific	15786803
DMEM, high glucose, HEPES, no phenol red	Gibco™	21063045
Dulbecco's modified Eagle's medium (DMEM)	Gibco™	11965084
EDTA-free Protease Inhibitor Cocktail	Roche	11836170001
Fetal calf serum (FCS)	Capricorn	FBS-12A
Flavopiridol hydrochloride hydrate	Sigma-Aldrich	F3055
Formaldehyde solution	Sigma-Aldrich	47608
Formic acid	Sigma-Aldrich	5.33002
Glycerol	Honeywell	49770
HEPES	GibcoTM	15630080
JetPEI Transfection reagent	Polyplus	101-10N
Imidazole	Sigma-Aldrich	56750
Iodoacetamide	Cambridge Isotope Laboratories	DLM-7249-0.1
L-Proline	Sigma-Aldrich	P0380-100G
Magnesium chloride (MgCl2)	Fluka	63072
Methanol	Honeywell	32213
MG132	Enzo	BML-PI102
MLN4924 (NAE1i)	Boston Biochem	I-502
Nonidet P 40 Substitute (NP40)	Fluka	74385
Sequencing Grade Modified Trypsin	Promega	V5113
Sodium chloride (NaCl)	Sigma-Aldrich	71380-M
Penicillin/streptomycin (PS)	Sigma-Aldrich	P0781
Puromycin	InvivoGen	ant-pr-1
Q5 hifi DNA pol	Biolabs	M0491S
THZ1	Xcessbio.com	M60214-2S
Tris(2-carboxyethyl)phosphine (TCEP)	Sigma-Aldrich	C4706
TritonTM X-100	Sigma-Aldrich	T8787
Trizma® base	Sigma-Aldrich	T6066
TWEEN® 20	Sigma-Aldrich	P1379
	Commercial kits	
PureLink® Genomic DNA Mini Kit	Invitrogen	K182001
RNAiMAX transfection reagent	Invitrogen	13778500
	Deposited data	
CryoEM	EMDB	EMD-18377
	EMDB	EMD-18378
	EMDB	EMD-18380
	EMDB	EMD-18413
	PDB	PDB-8QH5

Mass spectrometry data	PRIDE/ProteomeXchange	PXD045415
Experimental models: cell lines		
CS3BEhT CSA-GFP	[32]	N/A
HCT116 CSA KO	[31]	N/A
HCT116 CSA-mClover KI	This paper	N/A
HCT116 CSA-mClover KI DDA1 KO	This paper	N/A
HCT116 CSB KO	[31]	N/A
HCT116 DDA1 KO	This paper	N/A
HCT116 GFP-DDB2 KI	This paper	N/A
HCT116 Wild type	[13]	N/A
VH10hT GFP-DDB2	[68]	N/A
Software and algorithms		
AlphaFold2	[69]	N/A
Chimera	[70]	N/A
Coot	[71]	N/A
cryoSPARC	[72]	N/A
CTFFIND-4.1	[73]	N/A
Fiji ImageJ	https://imagej.net/Fiji	N/A
LAS AF (version 3.3.0.16799)	Leica Microsystems	N/A
MaxQuant software (version1.6.3.3 or 2.0.3.0)	[74]	N/A
MotionCor2	[75]	N/A
PDB-REDO	[76]	N/A
Perseus (version 1.6.14.0)	[77]	N/A
Phenix	[78]	N/A
Prism GraphPad (version 8.2.1)	GraphPad software Inc.	N/A
QIAGEN IPA	[46]	N/A
Relion3.0	[79]	N/A
Spectronaut Pulsar X (version 17.0.221202)	Biognosys,	N/A
TOPAZ	[80]	N/A
Equipment		
Bioruptor Sonication System	Diagenode	N/A
EASY-nLC™ 1200 System	ThermoScientific	N/A
FACS Aria II 5L SORP	BD	N/A
FEI Titan Krios 300 kV electron microscope	ThermoScientific	N/A
GelCount	Oxford Optronix	N/A
Leica TCS SP8 microscope	Leica	N/A
LSM700 Axio Imager Z2 upright microscope	Zeiss	N/A
Mass Spectrometer Orbitrap Lumos™ Tribrid™	ThermoScientific	N/A
Odyssey® Imaging System	LI-COR	N/A
Prometheus NT.48	NanoTemper Technologies	N/A
Vitrobot Mk IV plunge freezer	ThermoScientific	N/A

Other		
Amicon ultrafiltration	Merck Millipore	N/A
GFP-Trap-A® agarose bead slurry	ChromoTek	gta-100
Glutathione sepharose 4B resin	Cytiva	N/A
HiTrapQ column	GE Healthcare	N/A
HiTrapSP column	GE Healthcare	N/A
PTMscan (K-ε-GG)	Cell Signaling Technologie	5562
Mini-PROTEAN TGX™ Precast Protein Gels	BioRad	456-1084
Nickel-chelating sepharose	Cytiva	N/A
NuPAGE™ 4 to 12% Precast Protein Gels	Invitrogen	NP0321BOX
NuPAGE™ MOPS SDS running buffer	Invitrogen	NP0001
Resource Q column	GE Healthcare	N/A
Superdex 200 16/600 column	GE Healthcare	N/A
TUV lamp (UV-C)	Phillips	N/A
Zeba Spin Desalting Columns	ThermoScientific	N/A

Cell lines and cell culture.

HCT116 colorectal cancer cells were cultured in Dulbecco's modified Eagle's medium DMEM or in phenol red-free DMEM for live cell imaging experiment, supplemented with 10% fetal calf serum, 1% penicillin/streptomycin in a humidified incubator at 37 °C and 5% CO2. VH10 (GFP-DDB2[68], hTert), CS3BE (CSA-GFP[32], hTert) fibroblasts were maintained in DMEM with 15% FCS and antibiotics. For SILAC, cells were grown for 2 weeks (>10 cell doublings) in arginine/lysine-free SILAC DMEM supplemented with 15% dialysed FCS, 1% penicillin–streptomycin, 200 μg ml^{-1} proline and either 73 μg.ml^{-1} light [$^{12}C_6$]-lysine and 42 μg.ml^{-1} [$^{12}C_6$, $^{14}N_4$]-arginine or heavy [$^{13}C_6$]-lysine and [$^{13}C_6$, $^{15}N_4$]-arginine.

HCT116 KO cells were generated by transiently transfecting HCT116 cells by jetPEI with a pLentiCRISPR.v2 plasmid[67] expressing Cas9 and containing appropriate sgRNAs (Table reagent or resource), according to manufacturer instructions. Transfected cells were selected by culturing in 1 μg.ml^{-1} puromycin containing medium for 2 days, and single cells were seeded to allow expansion. Genotyping of single-cell clones was performed by immunoblotting or genomic PCR as indicated (Table reagent or resource).

CSA-GFP-3NLS, GFP-3NLS and GFP-DDA1 complemented cell lines were generated by lentiviral transduction in WT and DDA1$^{-/-}$ cells. Full-length expression construct with GFP-DDA1 was synthesized (gene synthesis services, GenScript). Three nuclear localization signals (3NLS) were added to CSA-GFP and GFP[28]. Tagged CSA-GFP-3NLS, GFP-3NLS and GFP-DDA1 constructs were inserted in a pLenti-CMV-puro-DEST plasmid[66]. After transduction, cells were selected with 1 μg ml^{-1} puromycin.

HCT116 CSA-mClover KI cells were generated by transiently transfecting cells with a sgRNA-containing pLentiCRISPR.v2 plasmid (Table reagent or resource) targeting the stop codon of CSA and co-transfecting a homology-directed repair template, which included two TEV cleaving sites, mClover and on either side 300 bp CSA locus-specific genomic DNA for homologous recombination to each end of CRISPR-generated dsDNA break (gene synthesis services GenScript, sequence upon request). The cells were seeded and kept in the presence of 2 ug.ml^{-1} puromycin and subsequently sorted for mClover-positive cells by FACS. Single-cell clones were genotyped, and homozygous KI clones were selected for further analysis. Genotyping PCR was performed on genomic DNA isolated using a PureLink® Genomic DNA Mini Kit according to the manufacturer's protocol with Q5 hifi DNA

polymerases according to the manufacturer's protocol. Primer sequences are provided in Table reagent or resource.
siRNA (Table reagent or resource) transfections were performed 2 or 3 days before each experiment using Lipofectamine RNAiMax according to the manufacturer's protocol. Knockdown efficiency was determined by immunoblotting.

Survival assays
For the clonogenic survival assay, 750 cells were seeded per well in triplicate in a 6-well plate. The following day, cells were treated with UV at the indicated doses. Following treatment, colonies were grown for 7–10 days, after which they were fixed and stained using Coomassie blue (50% methanol, 7% acetic acid and 0.1% Coomassie blue. Colony numbers were counted using GelCount. The relative colony number was plotted from at least three independent experiments, each performed in triplicate. Levels were normalized to mock-treated, set to 100 and plotted with standard deviation values (SD).

RNA synthesis recovery assay
Cells were grown on coverslips and mock treated or irradiated with 10 $J.m^{-2}$ UV. RNA was labelled at the indicated time points for 1 h with 200 μM EU , fixed with 3.7% formaldehyde (FA) in PBS for 15 min at room temperature and permeabilized by 0.1% Triton X-100 in PBS for 10 min. Cells were incubated for Click-it-chemistry-based azide coupling for 1 h with 60 μM Atto594 Azide in 50 mM Tris buffer (pH 8) with 4 mM CuSO4 and 10 mM freshly prepared ascorbic acid. 4,6-Diamidino-2-phenylindole (DAPI) was added to visualize the nuclei. Coverslips were washed with 0.1% Triton in PBS and with PBS only and mounted with Aqua-Poly/Mount. Cells were imaged using a Zeiss LSM 700 Axio Imager Z2 upright microscope (Carl Zeiss Micro Imaging). The EU signal in the nuclei was quantified using ImageJ.

Total extracts and immunoblotting
Cell pellets were lysed in denaturing lysis buffer (2% SDS, 1% NP-40, 150mM NaCl, 50mM Tris pH 7.5) with additional 50 U Benzonase® nuclease for 10 min at RT in rotation. Lysates were centrifuged 13,200 r.p.m. for 10 min and equal volumes of supernatant and 2x Laemmli-SDS sample buffer were heated at 98°C for 5 min. Proteins were separated by SDS-PAGE using 4–12% Bis-Tris NuPAGE® gels with MOPS running buffer. Separated proteins were transferred onto PVDF membranes (0.45 μm) overnight at 4 °C, blocked in 5% BSA in PBS and probed with the appropriate primary antibodies (Table reagent or resource). Membranes were washed with PBS containing 0.05% Tween-20 and incubated with IRDye-conjugated secondary antibodies (Table reagent or resource). Proteins were visualized by the Odyssey® Imaging System.

Immunoprecipitation
GFP-DDB2, CSA-GFP ectopically expressing cell lines and the CSA-mClover KI cells were mock-treated or irradiated with 10 or 30 $J.m^{-2}$ UV at different time points before cell collection. Cell pellets were prepared from three confluent 145-cm^2 dishes per condition for IP or mass spectrometry. Cells were collected by trypsinization and pelleted in cold PBS by centrifugation for 5 mins at 1,500 r.p.m. After one wash with cold PBS, cell pellets were stored at −80 °C until IP analysis. For IP, pellets were thawed on ice and lysed for 10 min on ice in HEPES buffer containing 30mM HEPES pH 7.5; 130mM NaCl; 1mM $MgCl_2$; 0.5% Triton X-100; 1x EDTA-free Protease Inhibitor Cocktail. After 10 cycles of sonication using the Bioruptor Sonicator (15 sec on; 45 sec off) at 4°C, 500 U Benzonase® nuclease was added and samples were kept in rotation for 1-2 h at 4°C. The insoluble fraction was pelleted at

13,200 r.p.m. for 10 min at 4 °C, and the soluble fraction was applied for immoprecipitation for 90 min at 4 °C, using 25 µl slurry GFP-Trap®A beads. Bound proteins were directly digested by trypsin for MS-data independent analysis (DIA) or eluted with SDS–PAGE loading buffer and separated on 4–12% Bis-Tris NuPAGE® gels and processed for immunoblotting or for MS-data dependent analysis approach (DDA).

Immunofluorescence

Immunofluorescence was carried out as previously described[81]. Cells were grown on 24-mm glass coverslips and fixed for 15 min in PBS with 3.7% FA. Subsequently, cells were permeabilized with 0.1% Triton X-100 in PBS and washed with PBS+ (0.15% BSA and 0.15% glycine in PBS). Cells were incubated for 2 h at room temperature with rabbit anti-CSA, DDB2, GFP antibodies (Table reagent or resource) in PBS+. Thereafter, cells were washed with PBS+, 0.1% Triton and PBS+ before incubating for 2 h at room temperature with donkey anti-rabbit Alexa Fluor 488 or anti-rabbit Alexa Fluor 594 or anti-mouse Alexa Fluor 488 conjugated antibody (Table reagent or resource) and DAPI. Alexa Fluor 647 Phalloidin was used to detect actin. After washes with PBS+ and 0.1% Triton, coverslips were mounted with Aqua-Poly/Mount. Images were acquired with a Zeiss LSM700 Axio Imager Z2 upright microscope equipped with a ×63 Plan-apochromat 1.4 NA oil-immersion lens (Carl Zeiss Micro Imaging). The intensities were quantified using ImageJ.

UV laser accumulation

Accumulation of proteins to UV laser-induced DNA damage was measured on a Leica SP8 confocal microscope (with LAS X software version 3.3.0.16799), coupled to a 4.5 mW pulsed (15 kHz) diode-pumped solid-state laser emitting at 266 nm (Rapp Opto Electronic, Hamburg GmbH; Supplementary). Cells, grown on quartz coverslips, were imaged and irradiated through an Ultrafluar quartz 100×/1.35 NA glycerol immersion lens (Carl Zeiss Micro Imaging Inc.) at 37 °C and 5% CO2. Resulting accumulation curves were corrected for background values and normalized to the relative fluorescence signal before local irradiation. After background correction, signals in the damaged and non-damaged areas of the nucleus were normalized to the average fluorescence levels of pre-damage conditions.

Fluorescence Redistribution After Photobleaching

For FRAP, a Leica TCS SP8 microscope equipped with a 40 × /1.25 NA HC PL APO oil immersion lens (Leica Microsystems) was used. CSA-mClover cells were maintained at 37 °C and 5% CO_2 during imaging. Cells were seeded on glass coverslip two days prior to live imaging experiments and were treated with indicated UV doses and/or incubated with transcription inhibitors THZ1 (1 µM) 1 h before live cell imaging, or treated with CRL inhibitor NAE1i (10 µM) 30 min before FRAP analysis. A narrow strip of 512 × 16 spanning the nucleus was imaged at 400 Hz using a 488-m laser with a zoom of 8x. A total of 30 frames were measured to reach steady-state levels before photobleaching, followed by two frame 100% laser power. After photobleaching, the redistribution or recovery of fluorescence was measured with 200 ms frames until steady-state was reached. Fluorescence intensity was background-corrected, normalized to the average of the last 30 pre-bleach frames and set to 100%. During one experiment for each condition at least 10 cells were measured. The immobile fraction (F_{imm}) was calculated as described in (REF) with the formula: $F_{imm} = 1 - (I_{final,\ treat} - I_{0,\ treat})/(I_{final,\ untr} - I_{0,\ treat})$

K-GG enrichment

Analysis of the global proteome and enrichment for diGlycine (diGly) remnant containing peptides using antibody-based enrichment was performed as described before[45]. Briefly, proteolytic peptides were fractionated using high pH reverse-phase (RP) chromatography. For the RP chromatography, a protein digest: stationary phase ratio of 1 : 50 was used and peptides were eluted in three fractions using increasing amounts of acetonitrile (7 %, 13.5 % and 50 %). Fractions and flowthrough were subsequently dried to completeness by lyophilization. For immunoprecipitation of diGly peptides, ubiquitin remnant motif (K-ε-GG) antibodies coupled to beads (PTMscan) were used. After immunoprecipitation, the supernatant was stored for further global proteome analysis.

Mass Spectrometry

MS DATA Dependent Analysis (DDA): CSA-mClover protein complexes were pulled down from chromatin-enriched protein extracts with GFP-Trap®A beads as described previously[31]. Eluted proteins in Laemmli-SDS sample buffer were separated on 4–12% Bis-Tris NuPAGE® gels with MOPS running buffer and visualized with Coomassie. After cutting the gel lanes into 2-mm slices, the proteins were in-gel reduced with dithiothreitol, alkylated with iodoacetamide and digested with trypsin. Peptides were separated on a home-made 20 cm x 100 µm C18 column (BEH C18, 130 Å, 3.5 µm, Waters, Milford, MA, USA) after trapping on a nanoAcquity UPLC Symmetry C18 trapping column (Waters, 100 Å, 5 µm, 180 µm x 20 mm), using an EASY-nLC 1000 liquid-chromatograph. Subsequent mass spectrometry analyses were performed on a Thermo Scientific Orbitrap Fusion™ Lumos Tribrid™ mass spectrometer or an Orbitrap Eclipse™ Tribrid™ mass spectrometer directly coupled to the EASY-nLC. All mass spectra were acquired in profile mode. The resolution in MS1 mode was set to 120,000 (AGC target: 4E5), the m/z range 350-1400. Fragmentation of precursors was performed in 2 s cycle time data-dependent mode by HCD with a precursor window of 1.6 m/z and a normalized collision energy of 30.0; MS2 spectra were recorded in the orbitrap at 30,000 resolution. Singly charged precursors were excluded from fragmentation and the dynamic exclusion was set to 60 seconds.

Raw mass spectrometry data were analyzed with the MaxQuant software suite[74] as described previously[82] with the additional options 'LFQ' and 'iBAQ' selected. The A false discovery rate of 0.01 for proteins and peptides and a minimum peptide length of 7 amino acids were set. The Andromeda search engine was used to search the MS/MS spectra against the Uniprot database (taxonomy: Homo sapiens, release December 2022) concatenated with the reversed versions of all sequences. A maximum of two missed cleavages was allowed. The peptide tolerance was set to 10 ppm and the fragment ion tolerance was set to 0.6 Da for HCD spectra. The enzyme specificity was set to trypsin and cysteine carbamidomethylation was set as a fixed modification. For K-GG enriched samples, the number of missed cleavages was raised to 3, while the variable modifications were set to oxidation (M) and GlyGly (K) and no fixed modification was selected. Both the PSM and protein FDR were set to 0.01. In case the identified peptides of two proteins were the same or the identified peptides of one protein included all peptides of another protein, these proteins were combined by MaxQuant and reported as one protein group. Before further statistical analysis, the 'proteingroups.txt' table was filtered for contaminants and reverse hits.

MS DATA Independent Analysis (DIA): CSA-mClover protein complexes were pulled down from chromatin-enriched protein extracts with GFP-Trap®A beads as described previously[31]. Proteins were reduced with dithiothreitol, alkylated with iodoacetamide and digested with trypsin on beads. Peptides were separated on a home-made 20 cm x 100 µm C18 column (BEH C18, 130 Å, 3.5 µm, Waters, Milford, MA, USA) after trapping on a nanoAcquity UPLC Symmetry C18 trapping column (Waters, 100 Å, 5 µm, 180 µm x 20 mm), using an EASY-nLC 1000 liquid-chromatograph. Subsequent mass spectrometry analyses were performed on Thermo Scientific Orbitrap Fusion™ Lumos Tribrid™ mass

spectrometer Orbitrap Eclipse™ Tribrid™ mass spectrometer directly coupled to the EASY-nLC. All spectra were recorded at a resolution of 120,000 for full scans in the scan range from 350–1650 m/z. The maximum injection time was set to 50 ms (AGC target: 4E5). For MS2 acquisition, the mass range was set to 336–1391 m/z with dynamic isolation windows ranging from 7–82 m/z, with a window overlap of 1 m/z. The orbitrap resolution for MS2 scans was set to 30,000. The maximum injection time was at 54 ms (AGC target: 5E4; normalized AGC target: 100 %).
DIA raw data files were analyzed with the Spectronaut Pulsar X software package (Biognosys, version 17.0.221202), using directDIA for DIA analysis including MaxLFQ as the LFQ method and Spectronaut IDPicker algorithm for protein inference. The Q-value cutoff at precursor and protein level was set to 0.01. All imputation of missing values was disabled.
MS raw data and data for protein identification and quantification were submitted as supplementary tables to the ProteomeXchange Consortium via the PRIDE partner repository with the data identifier PXD045415.

Expression clones for recombinant proteins

All coding genes are full length and of human origin. Except where noted, individual ORFs were cloned into pETNKI vectors by ligase-independent cloning[62]. The pAC8-CSA-Strep II clone was a gift from Nicolas Thomä[10]. The N-terminal 6×histidine tagged DDB1 gene was synthesized and codon optimized for insect cell expression (gene synthesis services, Integrated DNA Technologies). The DDA1 construct was derived from GFP-DDA1 (gene synthesis services, GenScript), a TwinStrep-flag tag was introduced to the C-terminus. The CUL4A and RBX1 constructs[60,61] were obtained from Yue Xiong laboratory, both genes were fused in-frame to a N-terminal 6×histidine tag. The N-terminal 6×histidine tagged UVSSA gene was synthesized and codon optimized for insect cell expression (gene synthesis services, Integrated DNA Technologies). The pFastBac-HA-CSB-His6 construct was derived from Wim Vermeulen laboratory, the coding sequence contains an N-terminal HA tag and a C-terminal 6×histidine tag[63]. The codon-optimized pGEX-6p1-USP7^{C223A} construct was derived from Titia Sixma laboratory, the gene was codon optimized for bacterial expression and a GST tag was fused at the N-terminus[64]. The bacterial expression vectors pGEX-APPBP1-UBA3, pGEX-UBE2M and pGEX-NEDD8 were gifts from Brenda Schulman [65].
For protein complex co-expression in insect cells (CSA-DDB1-DDA1, CSA-DDB1, CUL4A-RBX1), biGBac polycistronic expression system was generated. The individual gene expression cassettes were amplified by PCR and integrated into a pBIG1a vector by Gibson assembly as described previously[83].

CSA-DDB1-DDA1 and CSA-DDB1 purification

The CSA complexes with and without DDA1 were expressed in Sf9 insect cells and purified an analogous procedure. Pellet from 2L Sf9 culture was re-suspended in lysis buffer (20 mM HEPES pH 7.5, 150 mM NaCl, 5% glycerol (v/v), 0.1 mM EDTA, 0.5 mM TCEP, 30 mM imidazole). Cells were opened by sonication and the debris was removed by centrifugation at 53,340 ×g for 30 min at 4°C. Clarified lysate was loaded onto 5 ml Nickel-chelating sepharose and washed with 150 ml lysis buffer. The protein was eluted with lysis buffer containing 300 mM imidazole. The eluate was applied to a Resource Q column and then eluted with a 200-600 mM NaCl gradient. Peak fractions were collected, concentrated and injected into Superdex 200 16/600 column pre-equilibrated with SEC buffer (20 mM HEPES pH 7.5, 150 mM NaCl, 5% glycerol (v/v), 0.1 mM EDTA, 0.5 mM TCEP). The peak fractions were concentrated to around 5 mg/ml using an Amicon ultrafiltration device. Proteins were frozen in liquid nitrogen and stored in -80°C.

UVSSA purification

Pellet from 2L Sf9 culture was re-suspended in high salt lysis buffer (20 mM HEPES pH 7.5, 500 mM NaCl, 5% glycerol (v/v), 0.1 mM EDTA, 0.5 mM TCEP, 30 mM imidazole). Cells were opened by sonication and the debris was removed by centrifugation at 53,340 ×g for 30 min at 4°C. Clarified lysate was loaded onto 5 ml Nickel-chelating sepharose and washed with 100 ml high salt lysis buffer and 50 ml low salt lysis buffer (20 mM HEPES pH 7.5, 150 mM NaCl, 5% glycerol (v/v), 0.1 mM EDTA, 0.5 mM TCEP, 30 mM imidazole). The protein was eluted with low salt lysis buffer containing 300 mM imidazole. The eluate was applied to a Resource S column and then eluted with a 150-450 mM NaCl gradient. Fractions containing UVSSA were collected and diluted two times with dilution buffer (20 mM HEPES pH 7.5, 5% glycerol (v/v), 0.1 mM EDTA, 0.5 mM TCEP). The diluted UVSSA was absorbed onto a 5 ml HiTrapQ column and eluted with a 200-500 mM NaCl gradient. To concentrate the protein, the peak fractions were collected and dialyzed overnight against storage buffer (20 mM HEPES pH 7.5, 300 mM NaCl, 50% glycerol (v/v), 0.1 mM EDTA, 0.5 mM TCEP). Protein was frozen in liquid nitrogen and stored at -80°C.

Preparation of K414 mono-ubiquitinated UVSSA

UVSSA can be in vitro mono-ubiquitinated by E2 enzyme UBE2E1 (UbcH6) in an E3-independent manner[18]. The UVSSA after HiTrapQ purification was used for large scale preparation of mono-ubiquitinated UVSSA. 50 mM Bis-Tris-Propane pH 9.0, 0.5 μM UBA1, 16 μM UBE2E1, 20 μM ubiquitin, 10 mM $MgCl_2$, 1 mM TCEP were added into UVSSA. Reaction was initiated by adding 5 mM ATP and incubate at room temperature for 30 min, and then the reaction was purified again with HiTrapQ column. The peak fractions were collected and dialyzed against storage buffer as described above.

CSB purification

Pellet from 2L Sf9 culture was re-suspended in high salt lysis buffer (20 mM HEPES pH 7.5, 500 mM NaCl, 5% glycerol (v/v), 0.1 mM EDTA, 0.5 mM TCEP, 30 mM imidazole). Cells were opened by sonication and the debris was removed by centrifugation at 53,340 ×g for 30 min at 4°C. Clarified lysate was loaded onto 5 ml Nickel-chelating sepharose and washed with 100 ml high salt lysis buffer and 50 ml low salt lysis buffer (20 mM HEPES pH 7.5, 150 mM NaCl, 5% glycerol (v/v), 0.1 mM EDTA, 0.5 mM TCEP, 30 mM imidazole). The protein was eluted with low salt lysis buffer containing 300 mM imidazole. The eluate was applied to a Heparin column and then eluted with a 150-1000 mM NaCl gradient. The peak fractions were concentrated and injected into a Superdex 200 16/600 column pre-equilibrated with SEC buffer (20 mM HEPES pH 7.5, 450 mM NaCl, 5% glycerol (v/v), 0.1 mM EDTA, 0.5 mM TCEP). The CSB fractions were concentrated to around 5 mg/ml. Aliquots were frozen in liquid nitrogen and stored in -80°C.

USP7^{C223A} purification

USP7^{C223A} was purified as previously described with minor modifications [64]. Pellet from 4L E. coli Rosetta2(DE3) pLysS culture in TB medium was re-suspended in high salt lysis buffer (20 mM HEPES pH 7.5, 500 mM NaCl, 5% glycerol (v/v), 0.1 mM EDTA, 0.5 mM TCEP). Cells were opened by sonication and the debris was removed by centrifugation at 53,340 ×g for 30 min at 4°C. Clarified lysate was loaded onto 5 ml glutathione sepharose 4B resin and washed with 100 ml high salt lysis buffer and followed with 50 ml low salt buffer (20 mM HEPES pH 7.5, 150 mM NaCl, 5% glycerol (v/v), 0.1 mM EDTA, 0.5 mM TCEP). The protein was eluted with low salt buffer containing 20 mM reduced

glutathione. The GST tag was removed by 3C protease under dialysis against Q buffer (20 mM HEPES pH 7.5, 50 mM NaCl, 5% glycerol (v/v), 1 mM EDTA, 0.5 mM TCEP). The sample was then loaded onto a Resource Q column and eluted with a 100-450 mM NaCl gradient. The peak fractions were collected and injected into Superdex 200 16/600 column pre-equilibrated with SEC buffer (20 mM HEPES pH 7.5, 150 mM NaCl, 5% glycerol (v/v), 0.1 mM EDTA, 0.5 mM TCEP). The fractions of pure USP7 were concentrated to around 5-12 mg/ml using ultrafiltration device. Proteins were frozen in liquid nitrogen and stored in -80°C.

Neddylated CUL4A-RBX1 purification

Pellet from 2L Sf9 culture was re-suspended in lysis buffer (20 mM HEPES pH 7.5, 200 mM NaCl, 10% glycerol (v/v), 0.1 mM EDTA, 0.5 mM TCEP, 30 mM imidazole). Cells were opened by sonication and the debris was removed by centrifugation at 53,340 ×g for 30 min at 4°C. Clarified lysate was loaded onto 5 ml Nickel-chelating sepharose and washed with 150 ml lysis buffer. The protein was eluted with the same buffer containing 300 mM imidazole. The eluate was diluted to 120 mM NaCl and loaded onto a HiTrapSP column. Proteins were eluted with 120-500 mM NaCl gradient. The peak fractions were collected and treated with 3C protease to remove the tags. The proteins were injected into a Superdex 200 16/600 column pre-equilibrated with SEC buffer (20 mM HEPES pH 7.5, 200 mM NaCl, 10% glycerol (v/v), 0.5 mM TCEP). The fractions of CUL4A-RBX1 were concentrated for in vitro neddylation reaction.

The in vitro neddylation was carried out in a 2 ml reaction containing 9 µM CUL4A-RBX1, 0.2 µM APPBP1-UBA3, 4 µM UBE2M, and 30 µM NEDD8 in 20 mM HEPES pH 7.5, 200 mM NaCl, 10% glycerol, 2 mM ATP, 5 mM $MgCl_2$ and 0.5 mM TCEP. The reaction was incubated at room temperature for 30 minutes and terminated by adding EDTA to 50 mM. The neddylated CUL4A-RBX1 was further purified by cation ion exchange and size exclusion chromatography as described above.

Cryo-EM sample preparation

UVSSA~Ub, USP7C223A, and CSA-DDB1-DDA1 were mixed in 1:1:1 ratio and incubated on ice for 10 min. The complex was crosslinked by GraFix[84] in which the sample was applied to a glycerol gradient containing 20 mM HEPES pH 7.5, 150 mM NaCl, 0.5 mM TCEP, 10-30% glycerol and 0-0.12% glutaraldehyde. The gradient was ultracentrifugated at 90,000 ×g for 16 hours at 4°C. Fractions containing the crosslinked complex were pooled and exchanged to the same buffer without glycerol using Zeba spin desalting column (Thermo Fisher Scientific). To prepare cryo-EM grids, 3 µl of crosslinked sample was applied on a Quantifoil R1.2/1.3 Cu 300 grid pre-coated with graphene oxide. The grid was blotted for 2.5 s and frozen in liquid ethane using Vitrobot Mk IV plunge freezer operating at 4°C and 100% humidity.

Cryo-EM data collection and processing

The micrographs were acquired on FEI Titan Krios 300 kV electron microscope (NeCEN, the Netherlands) with a K3 detector (Gatan) and an energy filter (Gatan) with slit width of 20 eV. Automated data collection was using EPU (ThermoFisher Scientific) and the movies were acquired in a magnification of 81,000× (1.09 Å/pix) with a dose of 60 e-/Å over 50 frames.

The initial data processing was carried out in cryoSPARC[72]. Particles were picked using TOPAZ[80]. The TOPAZ picking model was trained using manual picked particles from subset of micrographs. After 2D classification clean-up and consensus 3D refinement, the coordinates were imported to Relion3.0[79]. In Relion, micrographs were motion corrected by MotionCor2 and the contrast transfer function was estimated by CTFFIND-4.1[73,75]. Due to structural heterogeneity, iterations of particle subtraction and

focused classification were conducted. The details of the processing are described in Supplementary figure 4.

Model building

Model building and refinement were done in Chimera, Phenix and Coot[70,71,78]. For CSA-DDB1 (BPA and BPC), the available model (PDB code 7OO3[20]) was rigid body fitted to the map and manual adjusted in Coot. The missing loops of DDB1 (289-295, 743-748, 1111-1124) were built with the guidance of AlphaFold2 model[69]. For DDA1 the crystal structure (PDB code 6UD7[36]) was used as the initial reference, and the C-terminal helix was rebuilt in Coot. The core structure containing CSA-DDB1(BPA/BPC)-DDA1 was real space refined in Phenix and PDB-REDO[76,78]. The DDB1 BPB domain was rigid body fitted with available crystal structure (PDB code 6ZX9[85]) with minor adjustment. The UVSSA VHS domain was fitted with AlphaFold2 model from residue 1-150. Several cysteines (Cys222, Cys260 and Cys288 of CSA; Cys363, Cys725, and Cys1008 of DDB1) show additional density indicative of glutaraldehyde or oxidation, but resolution was not sufficient to build unequivocally.

Differential scanning fluorometry

The thermostability of CSA-DDB1-DDA1 and CSA-DDB1 were analyzed by differential scanning fluorometry (DSF). Samples were diluted to 2 µM in reaction buffer (20 mM HEPES pH 7.5, 150 mM NaCl, 5% glycerol, 0.5 mM TCEP) and applied on a Prometheus NT.48 using the standard capillaries. The intrinsic tryptophan fluoresce 350/330 nm ratio was measured in a 1°C/min temperature gradient from 20 to 90°C.

Ubiquitination assays

For analysis of E3-dependent UVSSA ubiquitination, 10 µl reactions were set up on ice containing 1.5 µM UVSSA, 0.2 µM UBA1, 1 µM UBE2E1 (UbcH6), 20 µM ubiquitin and indicated amount of neddylated $CRL4A^{CSA}$ in 20 mM HEPES pH 7.5, 100 mM NaCl, 2 mM ATP, 5 mM MgCl2 and 0.5 mM TCEP. Reactions were initiated by adding ATP and incubated at 30°C for 20 minutes. Reactions were terminated with SDS loading buffer. Proteins were separated on Bolt 8% Bis-Tris Plus gels (Thermo Fisher Scientific) in MOPS buffer and stained with Coomassie blue.

For CSB ubiquitination, analogous reactions were setup except using 1 µM CSB as substrate and 1 µM UBE2D3 (UbcH5c) as E2 enzyme. Proteins were separated on Bolt 4-12% Bis-Tris Plus gels in MOPS buffer and stained with Coomassie blue.

Statistical analysis

Mean values, as well as each individual value and S.D. or S.E.M. error bars are shown for each experiment. The number of samples analysed per experiment are reported in the respective figure legends. Multiple t-tests (unpaired, two-tailed) were used to determine statistical significance between groups, followed by multiple comparison correction with the Holm-Sidak method without assuming a consistent standard deviation. For analysis of Figure 3C-D, Figure 4B-C, supplementary Figure 1D, supplementary Figure 5A, C-D a nested t-test was performed with significance levels set to 0.05. All analyses were performed using Graph Pad Prism version 8.2.1 for Windows (GraphPad Software, La Jolla California USA). P values expressed as *$P < 0.05$; **$P < 0.01$, ***$P < 0.001$, ****$P < 0.0001$ were considered to be significant, otherwise as non-significant (n.s.). The networks were generated through the use of QIAGEN IPA[46] (QIAGEN Inc., https://digitalinsights.qiagen.com/IPA).

Figure 1. DDA1 is an interaction partner of CSA. **A-B,** Scatter plot of Log_2 SILAC ratios of proteins isolated by GFP-pulldown in CSA-mClover HCT116 cells. The experiments were conducted in duplicate with a label swap, comparing the GFP immunoprecipitation of mock-treated CSA-mClover versus HCT116 cells (**A**) or UV-treated CSA-mClover versus HCT116 cells (**B**). Proteins with Log_2 SILAC ratio >0.6 (indicated by gray line) in both replicates were classified as specific CSA interactors. RNAPII subunits are indicated in green, PAF1 subunits are indicated in light purple, proteins associated with RNAPII are indicated in brown, TFIIH subunits are indicated in grey, TRiC subunits are indicates in orange, the COP9 subunits in yellow, CRL subunits in dark purple and TC-NER factors are indicated in red. **C,** IP of CSA-mClover and GFP-DDB2 using GFP beads in CSA-mClover and GFP-DDB2 KI cells followed by immunoblotting for the indicated proteins. HCT116 cells were used as a control.

Figure 2. DDA1 is a component of $CRL4^{CSA}$ complex.
A, Domain architecture of the protein complex used for cryo-EM analysis. The stable core is highlighted by dash lines. Due to structural heterogeneity, USP7 and large part of UVSSA are invisible in the final reconstructed cryo-EM map. **B,** Cryo-EM structure of UVSSA-CSA-DDB1-DDA1. CSA (in light blue) and DDB1 (in light green) form a canonical substrate recognition module of CRL4 E3 ligases. The VHS domain of UVSSA (in pink) binds to a corner of CSA. DDA1 (in orange) interacts with both DDB1 and CSA. **C**, Molecular model of UVSSA-CSA-DDB1-DDA1 in ribbon diagram. **D**, Close up views of CSA interacting proteins. UVSSA interacts with CSA via the VHS domain (in pink). The C-terminal helix of DDA1 (in orange) interacts with CSA. The extension of the helix can be observed in the cryo-EM map at low threshold. **E**, Unstable interaction between DDA1 and CSA. The C-terminal helix of DDA1 is poorly resolved and various forms of densities can be identified by focused classification on this region, indicating that the interaction is unstable.

Figure 3. DDA1 is required for transcription recovery following DNA damage
A, Immunoblot of cell extracts from the HCT116 WT and KO cells stained for the indicated proteins. Tubulin and H2B were used as loading control. **B,** Transcription restart after UV, determined by relative EU incorporation in HCT116 WT and KO cells, at 24 hours after UV exposure (10 $J.m^{-2}$). EU incorporation derived fluorescence was normalized to non-irradiated cells (set to 1). The mean ± S.D. is indicated in red from three independent experiments of (left to right) n=454, 368, 486, 241, 393, 334, 412 and 283 cells. **C,** UV colony survival of HCT116 WT and KO cells exposed to the indicated doses of UV. Data shown represent the mean ± SD from three independent experiments. NS represent non-significant, *P ≤ 0.05, **P ≤ 0.01 relative to WT analysed by unpaired, two-tailed t-test, adjusted for multiple comparison. **D,** Transcription restart after UV, determined by relative EU incorporation in HCT116 WT and KO cells, at 24 hours after UV exposure (2.5, 5 and 10 $J.m^{-2}$) or mock treated. EU incorporation derived fluorescence was normalized to non-irradiated cells (set to 1). , The mean ± S.D. is indicated in red from three independent experiments of (left to right) n=1174, 1272, 1219, 1168, 1275, 1235, 1148, 980, 1014, 1278, 1166 and 1039 cells. Data shown in **B**, **D** NS represents non-significant, *P ≤ 0.05, **P ≤ 0.01, ****P ≤ 0.0001, each analysed by a nested t-test.

Figure 4. DDA1 provides properly CSA localization
A, Representative immunofluorescence images of endogenous CSA and DDB2 in HCT116 WT and KO cells, scale bar: 10 μm. **B**, Nuclear and cytoplasmic CSA and DDB2 levels in HCT116 WT and KO cells, analysed and quantified by fluorescence microscopy and ImageJ. The mean ± S.D. is indicated in red from three independent experiments of ≥ 30 images. CSA and DDB2 signal intensity at nucleus (as identified by DAPI staining) was compared to that in the rest of the cell (phalloidin). **C**,

Transcription restart after UV damage as determined by relative EU incorporation in HCT116 WT and KO cells, with either CSA-GFP-3NL or GFP-3NL expression, 24 h after UV exposure (10 $J.m^{-2}$) or mock treated. EU incorporation levels were normalized to the non-irradiated cells (set to 1). The mean ± S.D. is indicated in red from three independent experiments of (left to right) n=1275, 1118, 1164, 1195, 1068, 603, 1061 and 677cells. Data shown in **B** and **C** represent NS, **P ≤ 0.01 analysed by a nested t-test.

Figure 5. DDA1 modulates the protein network of CRL4^{CSA} complex

A-B, Volcano plots depicting the statistical differences between three replicates of the MS analysis after GFP immunoprecipitation of UV treated (**A**) or mock-treated (**B**) cells, comparing the protein network of CSA in WT with DDA1KO cells. The fold change (Log_2) is plotted on the x-axis and the significance (t-test $-Log_{10}$ (P value)) is plotted on the y-axis. RNAPII subunits are indicated in green, PAF1 subunits are indicated in light purple, proteins associated with RNAPII are indicated in brown, the COP9 subunits in yellow, CRL subunits in dark purple and TC-NER factors are indicated in red. **C**, Heatmap showing the statistically significantly enriched canonical pathways (p-value 0.001, Ingenuity Pathway Analysis, IPA) of the UV responsive ubiquitin sites that passed a 2-fold change cut-off (including duplicates). The color coding depicts -Log_{10}(P value) of the statistically significant terms. **D,** Heatmap showing the Log_2 SILAC ratios of ubiquitin sites that are quantified in all UV conditions (including duplicates) over untreated controls and that passed a 2-fold change cut-off (up and down regulated). The color density reflects the scale of enrichment. **E**, Log_2 SILAC ratios of ubiquitin K6, K11, K27, K29, K33, K48 and K63 chains as determined by quantitative global ubiquitin-proteomics in WT, CSAKO and DDA1KO cells after UV treatment (20 $J.m^{-2}$, 30 min). The mean ± S.D. of duplicate experiments are plotted. **F**, Log_2 SILAC ratios of POLR2A protein and ubiquitin sites of POLR2A (853K, 1268K and 1350K) as determined by quantitative proteomics and global ubiquitin-proteomics in WT, CSAKO and DDA1KO cells after UV treatment (20 $J.m^{-2}$, 30 min). The mean ± S.D. of duplicate experiments are plotted.

Figure 6. DDA1 affects the dynamic of CRL4^{CSA} via COP9 complex

A, Heatmap showing the statistically significantly enriched canonical pathways (p-value 0.001, Ingenuity Pathway Analysis, IPA) of the ubiquitin sites which were differentially modulated in mock treated conditions, that passed a 2-fold change cut-off. The color coding depicts $-Log_{10}$ (P value) of the statistically significant terms. **B**, SILAC ratios of POLR2A protein and ubiquitin sites of POLR2A (853K, 1268K and 1350K) as determined by quantitative proteomics and global ubiquitin-proteomics in WT/CSAKO and WT/DDA1KO cells in mock treated conditions. The mean ± S.D. of duplicate experiments are plotted. **C**, Binding kinetics of CSA-mClover in HCT116 WT or DDA1KO cells to locally UV damaged sites induced by 266 nm micro-beam laser irradiation. GFP fluorescence intensities at the site of UV damage were measured by real-time imaging until they reached a maximum. Mean and S.E.M. are from 30 cells per condition from three independent experiments. **D**, FRAP analysis of CSA-mClover in mock or UV irradiated (10 $J.m^{-2}$) HCT116 WT and DDA1KO cells, measured at the indicated time points. Percentage of CSA-mClover immobile fraction was determined from FRAP analyses (supplementary figure 13A). Graphs depict the mean & S.E.M. of ≥ 30 cells from at least three independent experiments. **E,** IP of CSA using GFP beads in CSA-mClover KI HCT116 WT and DDA1 KO cells followed by immunoblotting for the indicated proteins. Cells were collected 1 and 10 h after mock-treatment or irradiation with (10 $J.m^{-2}$) UV. **F**, FRAP analysis of CSA-mClover in presence or absence of NAEi added 1 h before irradiation and followed by UV irradiation (10 $J.m^{-2}$). Percentage of CSA-mClover immobile fraction determined from FRAP analyses (supplementary figure 13B) was measured at the indicated time points. Graphs depict the mean & S.E.M. of ≥ 30 cells from at least three

independent experiments. Data shown in **D** and **F** represent NS, *P ≤ 0.05, ****P ≤ 0.0001 analysed by unpaired, two-tailed t-test adjusted for multiple comparisons.

Supplementary Figure 1.

A, Schematic representation of the CSA-mClover, which includes a linker and two TEV protease recognition sequences. **B**, Immunoblot of indicated HCT116 cell lines showing CSA or CSA-mClover expression. Tubulin was used as loading control. **C**, Relative colony survival of the indicated HCT116 WT, CSA-mclover KI and CSA KO cells exposed to the indicated doses of UV. Data shown represent the mean ± SD from three independent experiments. **D**, Transcription restart after UV damage as determined by relative EU incorporation in the indicated HCT116 WT, CSA-mClover KI and CSA KO cells, at 24 h after UV exposure (10 $J.m^{-2}$) or mock treated. RNA synthesis was measured by EU incorporation and levels were normalized to the non-irradiated cells (set to 1) and each normalized EU signal is shown as one data point. The mean ± S.D. is indicated in red from three independent experiments. **E**, Fluorescence Recovery After Photobleaching (FRAP) analysis of CSA-mClover mobility in presence or absence of THZ1inhibitor added 1 h before irradiation and followed by UV irradiation (10 $J.m^{-2}$). Graphs depict the mean & S.E.M. of ≥ 30 cells from at least three independent experiments. **F,** FRAP analysis of CSA-mClover in mock and UV treated (10 $J.m^{-2}$) (the data are reported also in Supplementary Figure 13A). Graphs depict the mean & S.E.M. of ≥ 30 cells from at least three independent experiments. Data shown in **C** represent NS, *P ≤ 0.05, **P ≤ 0.01, ***P ≤ 0.001 relative to WT analysed by unpaired, two-tailed t-test, adjusted for multiple comparison. Data shown in **D** represent NS, *P ≤ 0.05 analysed by a nested t-test.

Supplementary Figure 2.

A, IP of CSA and DDB2 using GFP beads from CSA-GFP expressed in CS3BEhT and GFP-DDB2 expressed in VH10hT cells followed by immunoblotting for the indicated proteins. CS3BEhT and VH10hT cells were used as a control. **B**, FRAP analysis of GFP-DDB2 mobility from GFP-DDB2 KI HCT116 1 and 3 h after UV irradiation (10 $J.m^{-2}$). Graphs depict the mean & S.E.M. of ≥ 30 cells from at least three independent experiments. **C**, Relative colony survival of the indicated HCT116 WT and GFP-DDB2 knock-in cells exposed to the indicated doses of UV. Data shown represent the mean ± SD from three independent experiments. **D,** Scatter plot of Log_2 SILAC ratios of proteins isolated by GFP-pulldown from GFP-DDB2 KI HCT116 cells. The SILAC fold change (Log_2) is plotted on the x-axis and the signal intensity of the peptides is plotted on the y-axis. Data shown in **C** represent NS relative to WT analysed by unpaired, two-tailed t-test, adjusted for multiple comparison.

Supplementary Figure 3.

Cryo-EM sample preparation and data processing. Reconstitution of $USP7^{C223A}$-Ub~UVSSA-CSA-DDB1-DDA1 in a glycerol gradient is shown in the right panel. For EM analysis, the complex is crosslinked with glutaraldehyde. The fractions used for cryo-EM analysis are highlighted in red. Steps in processing are as indicated. Structure was built in the composite map.

Supplementary Figure 4.

A-B, Structure comparison of DDA1-DCAF interactions. The UVSSA-CSA-DDB1-DDA1 structure (this study, panel A) is compared to RBM39-DCAF15-DDB1-DDA1 (PDB 6UD7, panel B). Close up views of DDA1-DCAF interactions are highlighted below with cryo-EM density. The atomic model 6UD7 is fitted into cryo-EM map (EMDB 10213). DCAF15 has an atypical β propeller configuration that the extended β sheet provides a large interaction interface with the DDA1 C-terminal helix. C-D,

Thermostability analysis of CSA-DDB1 complexes. The stability of CSA-DDB1 was monitored by nanoDSF. C, The intrinsic fluorescence 350 nm/330 nm ratio of the samples. D, The first derivative of the melting experiments. In the presence of DDA1, the melting temperature increases about one degree. The experiment has been repeated multiple times and the results are reproducible.

Supplementary Figure 5.

A, Transcription restart after UV damage as determined by relative EU incorporation in the indicated HCT116 WT and KO cells, with DDA1 re-expression where indicated, at 24 hours after UV exposure (10 J/m2) or mock treated. RNA synthesis was measured by EU incorporation and levels were normalized to the non-irradiated cells (set to 1) and each normalized EU signal is shown as one data point. The mean ± S.D. is indicated in red from three independent experiments of (left to right) n=931, 1026, 1004, 638, 1122, 839, 703 and 593 cells. **B**, Immunoblot showing endogenous CSA-GFP, GFP-DDB2 and DDA1 levels in the indicated cell lines. Tubulin and H2B were used as loading control. **C**, **D** Representative immunofluorescence images of CSA-GFP and GFP-DDB2 expressed in CS3BEhT and VH10hT cells, respectivelyscale bar: 10 μm. Graphs below: Nuclear over cytoplasmic ratios of CSA and DDB2 levels in CS3BEhT and VH10hT cells, respectively, were analysed and quantified by fluorescence microscopy and ImageJ. The mean ± S.D. is indicated in red from three independent experiments of ≥ 30 images. CSA and DDB2 signal intensity at nucleus (as identified by DAPI staining) was compared to that in the rest of the cell (phalloidin). **E**, Representative immunofluorescence images of endogenous CSA in GFP-DDA1 re-expression HCT116 DDA1KO cells. The dashed lines indicate the line-scan track used to quantify fluorescence intensity of CSA (red) and GFP-DDA1 (green). The nucleus was identified using DAPI staining (Blu). **F,** Representative immunofluorescence images of CSA-GFP-3NLS and GFP-3NLS in WT and DDA1 KO HCT116 cells, scale bar: 10 μm. Data shown in **A**, **C** and **D** represent NS, **P ≤ 0.01, ***P ≤ 0.001, ****P ≤ 0.0001, analysed by a nested t-test.

Supplementary Figure 6.

A-B Volcano plots depicting the statistical differences between three replicates of the MS analysis after GFP immunoprecipitation of CSA-mClover mock-treated (**A**) or UV treated (**B**) in HCT116 cells. The fold change (log2) is plotted on the x-axis and the significance (t-test $-\text{Log}_{10}$(P value)) is plotted on the y-axis. RNAPII subunits are indicated in green, PAF1 subunits in light purple, TRiC subunits in orange, COP9 subunits in yellow, CRL subunits in dark purple and TC-NER factors in red. **C**, Quantitative interaction proteomics of CSA-mClover from CSA-mClover DDA1KO cells relative to CSA-mClover WT cells. Reduced and no changed interactions in absence of DDA1 are indicated by red and yellow arrows respectively.

Supplementary Figure 7.

A, Experimental set up and step-by-step proteomics workflow to obtain the global ubiquitin profile. **B**, Coverage of the global proteome indicating the number of ubiquitinated peptides quantified for each experiment. **C**, Heatmap shows Pearson R values of Log_2 ubiquitinated peptides SILAC ratios.

Supplementary Figure 8.

A-E, Scatter plots of Log_2SILAC ratios of ubiquitin sites in HCT116 WT, CSA KO, DDA1 KO cells. The experiments were conducted in duplicate comparing mock-treated versus UV-treated cells (**A-C**) or WT mock-treated versus KOs mock-treated HCT116 cells (**D-E**).

Supplementary Figure 9.

A-C, top 50 up-regulated ubiquitin sites in WT (**A**), CSA KO (**B**), DDA1 KO (**C**) HCT116 cells treated with UV irradiation in both experiments.

Supplementary Figure 10.
A, Purified proteins for in vitro assays. **B**, In vitro ubiquitination assay of CSB in the presence and absence of DDA1. The reactions were mediated by the E2 enzyme UBE2D3 (UbcH5c). C, In vitro ubiquitination assay of UVSSA in the presence and absence of DDA1. The reactions were mediated by the E2 enzyme UBE2E1 (UbcH6). Reactions were analyzed by SDS-PAGE and Coomassie blue staining. The results show that DDA1 has no effect on E3 ligase activity.

Supplementary Figure 11.
A, FRAP analysis of CSA-mClover in mock and UV treated (10 $J.m^{-2}$) using WT (the data are reported also in Supplementary Figure 1F) or DDA1 KO cell lines. Graphs depict the mean & S.E.M. of ≥ 30 cells from at least three independent experiments. **B,** FRAP analysis of CSA-mClover in presence or absence of NAEi added 1 h before irradiation and followed by UV irradiation (10 $J.m^{-2}$). Graphs depict the mean & S.E.M. of ≥ 30 cells from at least three independent experiments.

Supplementary Figure 12.
Full size unprocessed Western-blots of which crops were used in the indicated figures.

Supplementary Table 1
Table with SILAC ratios as determined using quantitative interaction proteomics (CSAmClover).

Supplementary Table 2
Table with SILAC ratios as determined using quantitative interaction proteomics (GFP-DDB2).

Supplementary Table 3
Table label free (Data Independent Analysis) as determined using quantitative interaction proteomics (CSAmClover in WT and DDA1KO cell lines).

Supplementary Table 4
Table with SILAC ratios as determined using quantitative proteomics of ubiquitin peptides (WT, CSAKO, DDA1KO HCT116 cell lines).

Supplementary Table 5
Table with SILAC ratios as determined using quantitative proteomics of total proteins (WT, CSAKO, DDA1KO HCT116 cell lines).

Acknowledgements
This work was supported by the CW-TOP grant (714.017.003 to WV, TS and MV), ALW grant (ALWOP.143 to JHJH), EMBO long-term fellowship (ALTF 1159-2019 to SHL), Oncode Institute (partly financed by the Dutch Cancer Society to WV, TS, MV and JHJH), National Institute of Health (NIH)/National Institute of Ageing (NIA) (P01 AG017242 to JHJH), ZonMw Memorabel (project ID 733050810 to JHJH), European Research Council Advanced Grant Dam2Age, DFG (German Research Foundation) - FOR 5504 (496650118 to JHJH), and the European Joint Project on Rare Diseases RD20-113, acronym TC-NER to JHJH). The content is solely the responsibility of the authors and does not

necessarily represent the official views of the National Institutes of Health. We thank NeCEN staff for help in data collection. We thank Benita Quist, Clarissa Polidoro Pontalti and Stanley Van for their technical help in the experiments.

Author contributions

W.V., A.P. and D.L.S. conceived the research. D.L.S. generated knockout cells, constructs and stable cell-lines, performed RRS and clonogenic survival assays, all live-cell imaging experiments, PCR and western blot analysis to validate knockouts. S.H.L. generated expression clones for recombinant proteins, purified recombinant protein, prepared, collected and processed the Cryo-EM samples, performed the differential scanning fluorometry. K.W.K. discussed and analyzed the mass spectrometry samples. A.F.T. generated knockout cells. A.H. generated knockout cells. K.B. performed Ubiquitin enrichment experiments for mass spectrometry and analyzed the mass spectrometry samples. C.G.H. performed RRS assays. M.V.d.V. performed Co-IP experiments for western blot analysis. A.P. performed Co-IP experiments for western blot analysis, Co-IP experiments for mass spectrometry and RRS assays. T.S, M.W., W.V. and A.P. supervised the project. D.L.S., S.H.L., T.S., W.V. and A.P. draft the paper. D.L.S., S.H.L., K.W.K., H.v.A., A.C.O.V., J.H.J.H., J.A.M., H.L., J.A.A.D., M.V., T.S., T.O., W.V., and A.P. contributed to conceptualization, and reviewed and edited the draft.

References

1 Schumacher, B., Pothof, J., Vijg, J. & Hoeijmakers, J. H. J. The central role of DNA damage in the ageing process. *Nature* **592**, 695-703, doi:10.1038/s41586-021-03307-7 (2021).

2 Hoeijmakers, J. H. DNA damage, aging, and cancer. *N Engl J Med* **361**, 1475-1485, doi:10.1056/NEJMra0804615 (2009).

3 van den Heuvel, D., van der Weegen, Y., Boer, D. E. C., Ogi, T. & Luijsterburg, M. S. Transcription-Coupled DNA Repair: From Mechanism to Human Disorder. *Trends Cell Biol* **31**, 359-371, doi:10.1016/j.tcb.2021.02.007 (2021).

4 Nieto Moreno, N., Olthof, A. M. & Svejstrup, J. Q. Transcription-Coupled Nucleotide Excision Repair and the Transcriptional Response to UV-Induced DNA Damage. *Annu Rev Biochem* **92**, 81-113, doi:10.1146/annurev-biochem-052621-091205 (2023).

5 Marteijn, J. A., Lans, H., Vermeulen, W. & Hoeijmakers, J. H. Understanding nucleotide excision repair and its roles in cancer and ageing. *Nat Rev Mol Cell Biol* **15**, 465-481, doi:10.1038/nrm3822 (2014).

6 Lans, H., Hoeijmakers, J. H. J., Vermeulen, W. & Marteijn, J. A. The DNA damage response to transcription stress. *Nat Rev Mol Cell Biol* **20**, 766-784, doi:10.1038/s41580-019-0169-4 (2019).

7 Xu, J. *et al.* Structural basis for the initiation of eukaryotic transcription-coupled DNA repair. *Nature* **551**, 653-657, doi:10.1038/nature24658 (2017).

8 Troelstra, C. *et al.* ERCC6, a member of a subfamily of putative helicases, is involved in Cockayne's syndrome and preferential repair of active genes. *Cell* **71**, 939-953, doi:10.1016/0092-8674(92)90390-x (1992).

9 Lee, J. & Zhou, P. DCAFs, the missing link of the CUL4-DDB1 ubiquitin ligase. *Mol Cell* **26**, 775-780, doi:10.1016/j.molcel.2007.06.001 (2007).

10 Fischer, E. S. *et al.* The molecular basis of CRL4DDB2/CSA ubiquitin ligase architecture, targeting, and activation. *Cell* **147**, 1024-1039, doi:10.1016/j.cell.2011.10.035 (2011).

11 Groisman, R. *et al.* The ubiquitin ligase activity in the DDB2 and CSA complexes is differentially regulated by the COP9 signalosome in response to DNA damage. *Cell* **113**, 357-367, doi:10.1016/s0092-8674(03)00316-7 (2003).

12 Cavadini, S. *et al.* Cullin-RING ubiquitin E3 ligase regulation by the COP9 signalosome. *Nature* **531**, 598-603, doi:10.1038/nature17416 (2016).

13 Nakazawa, Y. *et al.* Ubiquitination of DNA Damage-Stalled RNAPII Promotes Transcription-Coupled Repair. *Cell* **180**, 1228-1244 e1224, doi:10.1016/j.cell.2020.02.010 (2020).
14 van der Weegen, Y. *et al.* The cooperative action of CSB, CSA, and UVSSA target TFIIH to DNA damage-stalled RNA polymerase II. *Nat Commun* **11**, 2104, doi:10.1038/s41467-020-15903-8 (2020).
15 Groisman, R. *et al.* CSA-dependent degradation of CSB by the ubiquitin-proteasome pathway establishes a link between complementation factors of the Cockayne syndrome. *Genes Dev* **20**, 1429-1434, doi:10.1101/gad.378206 (2006).
16 Schwertman, P. *et al.* UV-sensitive syndrome protein UVSSA recruits USP7 to regulate transcription-coupled repair. *Nat Genet* **44**, 598-602, doi:10.1038/ng.2230 (2012).
17 Zhang, X. *et al.* Mutations in UVSSA cause UV-sensitive syndrome and destabilize ERCC6 in transcription-coupled DNA repair. *Nat Genet* **44**, 593-597, doi:10.1038/ng.2228 (2012).
18 Higa, M., Tanaka, K. & Saijo, M. Inhibition of UVSSA ubiquitination suppresses transcription-coupled nucleotide excision repair deficiency caused by dissociation from USP7. *FEBS J* **285**, 965-976, doi:10.1111/febs.14382 (2018).
19 Tufegdzic Vidakovic, A. *et al.* Regulation of the RNAPII Pool Is Integral to the DNA Damage Response. *Cell* **180**, 1245-1261 e1221, doi:10.1016/j.cell.2020.02.009 (2020).
20 Kokic, G., Wagner, F. R., Chernev, A., Urlaub, H. & Cramer, P. Structural basis of human transcription-DNA repair coupling. *Nature* **598**, 368-372, doi:10.1038/s41586-021-03906-4 (2021).
21 Pick, E. *et al.* Mammalian DET1 regulates Cul4A activity and forms stable complexes with E2 ubiquitin-conjugating enzymes. *Mol Cell Biol* **27**, 4708-4719, doi:10.1128/MCB.02432-06 (2007).
22 Olma, M. H. *et al.* An interaction network of the mammalian COP9 signalosome identifies Dda1 as a core subunit of multiple Cul4-based E3 ligases. *J Cell Sci* **122**, 1035-1044, doi:10.1242/jcs.043539 (2009).
23 Smits, A. H. & Vermeulen, M. Characterizing Protein-Protein Interactions Using Mass Spectrometry: Challenges and Opportunities. *Trends Biotechnol* **34**, 825-834, doi:10.1016/j.tibtech.2016.02.014 (2016).
24 Ong, S. E. & Mann, M. A practical recipe for stable isotope labeling by amino acids in cell culture (SILAC). *Nat Protoc* **1**, 2650-2660, doi:10.1038/nprot.2006.427 (2006).
25 Sternberg, S. H. & Doudna, J. A. Expanding the Biologist's Toolkit with CRISPR-Cas9. *Mol Cell* **58**, 568-574, doi:10.1016/j.molcel.2015.02.032 (2015).
26 Bajar, B. T. *et al.* Improving brightness and photostability of green and red fluorescent proteins for live cell imaging and FRET reporting. *Sci Rep* **6**, 20889, doi:10.1038/srep20889 (2016).
27 Nakazawa, Y., Yamashita, S., Lehmann, A. R. & Ogi, T. A semi-automated non-radioactive system for measuring recovery of RNA synthesis and unscheduled DNA synthesis using ethynyluracil derivatives. *DNA Repair (Amst)* **9**, 506-516, doi:10.1016/j.dnarep.2010.01.015 (2010).
28 Vermeulen, W. Dynamics of mammalian NER proteins. *DNA Repair (Amst)* **10**, 760-771, doi:10.1016/j.dnarep.2011.04.015 (2011).
29 Baymaz, H. I., Spruijt, C. G. & Vermeulen, M. Identifying nuclear protein-protein interactions using GFP affinity purification and SILAC-based quantitative mass spectrometry. *Methods Mol Biol* **1188**, 207-226, doi:10.1007/978-1-4939-1142-4_15 (2014).
30 Davo-Martinez, C. *et al.* Different SWI/SNF complexes coordinately promote R-loop- and RAD52-dependent transcription-coupled homologous recombination. *Nucleic Acids Res*, doi:10.1093/nar/gkad609 (2023).
31 Llerena Schiffmacher, D. A. *et al.* Live cell transcription-coupled nucleotide excision repair dynamics revisited. *DNA Repair (Amst)*, doi:10.1016/j.dnarep.2023.103566 (2023).
32 Pines, A. *et al.* TRiC controls transcription resumption after UV damage by regulating Cockayne syndrome protein A. *Nat Commun* **9**, 1040, doi:10.1038/s41467-018-03484-6 (2018).

33 Boeing, S. *et al.* Multiomic Analysis of the UV-Induced DNA Damage Response. *Cell Rep* **15**, 1597-1610, doi:10.1016/j.celrep.2016.04.047 (2016).
34 van den Heuvel, D. *et al.* A CSB-PAF1C axis restores processive transcription elongation after DNA damage repair. *Nat Commun* **12**, 1342, doi:10.1038/s41467-021-21520-w (2021).
35 Du, X. *et al.* Structural Basis and Kinetic Pathway of RBM39 Recruitment to DCAF15 by a Sulfonamide Molecular Glue E7820. *Structure* **27**, 1625-1633 e1623, doi:10.1016/j.str.2019.10.005 (2019).
36 Bussiere, D. E. *et al.* Structural basis of indisulam-mediated RBM39 recruitment to DCAF15 E3 ligase complex. *Nat Chem Biol* **16**, 15-23, doi:10.1038/s41589-019-0411-6 (2020).
37 Faust, T. B. *et al.* Structural complementarity facilitates E7820-mediated degradation of RBM39 by DCAF15. *Nat Chem Biol* **16**, 7-14, doi:10.1038/s41589-019-0378-3 (2020).
38 Shabek, N. *et al.* Structural insights into DDA1 function as a core component of the CRL4-DDB1 ubiquitin ligase. *Cell Discov* **4**, 67, doi:10.1038/s41421-018-0064-8 (2018).
39 Chapman, J. D., Goodlett, D. R. & Masselon, C. D. Multiplexed and data-independent tandem mass spectrometry for global proteome profiling. *Mass Spectrom Rev* **33**, 452-470, doi:10.1002/mas.21400 (2014).
40 Smits, A. H., Jansen, P. W., Poser, I., Hyman, A. A. & Vermeulen, M. Stoichiometry of chromatin-associated protein complexes revealed by label-free quantitative mass spectrometry-based proteomics. *Nucleic Acids Res* **41**, e28, doi:10.1093/nar/gks941 (2013).
41 Li, K. W., Gonzalez-Lozano, M. A., Koopmans, F. & Smit, A. B. Recent Developments in Data Independent Acquisition (DIA) Mass Spectrometry: Application of Quantitative Analysis of the Brain Proteome. *Front Mol Neurosci* **13**, 564446, doi:10.3389/fnmol.2020.564446 (2020).
42 Anindya, R., Aygun, O. & Svejstrup, J. Q. Damage-induced ubiquitylation of human RNA polymerase II by the ubiquitin ligase Nedd4, but not Cockayne syndrome proteins or BRCA1. *Mol Cell* **28**, 386-397, doi:10.1016/j.molcel.2007.10.008 (2007).
43 Herlihy, A. E. *et al.* UBAP2/UBAP2L regulate UV-induced ubiquitylation of RNA polymerase II and are the human orthologues of yeast Def1. *DNA Repair (Amst)* **115**, 103343, doi:10.1016/j.dnarep.2022.103343 (2022).
44 Yasukawa, T. *et al.* Mammalian Elongin A complex mediates DNA-damage-induced ubiquitylation and degradation of Rpb1. *EMBO J* **27**, 3256-3266, doi:10.1038/emboj.2008.249 (2008).
45 Bezstarosti, K., van der Wal, L. & Demmers, J. A. A. Detection of Protein Ubiquitination Sites by Peptide Enrichment and Mass Spectrometry. *J Vis Exp*, doi:10.3791/59079 (2020).
46 Kramer, A., Green, J., Pollard, J., Jr. & Tugendreich, S. Causal analysis approaches in Ingenuity Pathway Analysis. *Bioinformatics* **30**, 523-530, doi:10.1093/bioinformatics/btt703 (2014).
47 Elia, A. E. *et al.* Quantitative Proteomic Atlas of Ubiquitination and Acetylation in the DNA Damage Response. *Mol Cell* **59**, 867-881, doi:10.1016/j.molcel.2015.05.006 (2015).
48 Mandemaker, I. K. *et al.* DNA damage-induced histone H1 ubiquitylation is mediated by HUWE1 and stimulates the RNF8-RNF168 pathway. *Sci Rep* **7**, 15353, doi:10.1038/s41598-017-15194-y (2017).
49 Schulze-Niemand, E. & Naumann, M. The COP9 signalosome: A versatile regulatory hub of Cullin-RING ligases. *Trends Biochem Sci* **48**, 82-95, doi:10.1016/j.tibs.2022.08.003 (2023).
50 Garinis, G. A. *et al.* Persistent transcription-blocking DNA lesions trigger somatic growth attenuation associated with longevity. *Nat Cell Biol* **11**, 604-615, doi:10.1038/ncb1866 (2009).
51 Gyenis, A. *et al.* Genome-wide RNA polymerase stalling shapes the transcriptome during aging. *Nat Genet* **55**, 268-279, doi:10.1038/s41588-022-01279-6 (2023).
52 van der Weegen, Y. *et al.* ELOF1 is a transcription-coupled DNA repair factor that directs RNA polymerase II ubiquitylation. *Nat Cell Biol* **23**, 595-607, doi:10.1038/s41556-021-00688-9 (2021).
53 Geijer, M. E. *et al.* Elongation factor ELOF1 drives transcription-coupled repair and prevents genome instability. *Nat Cell Biol* **23**, 608-619, doi:10.1038/s41556-021-00692-z (2021).

54 Mulderrig, L. *et al.* Aldehyde-driven transcriptional stress triggers an anorexic DNA damage response. *Nature* **600**, 158-163, doi:10.1038/s41586-021-04133-7 (2021).
55 Garaycoechea, J. I. *et al.* Genotoxic consequences of endogenous aldehydes on mouse haematopoietic stem cell function. *Nature* **489**, 571-575, doi:10.1038/nature11368 (2012).
56 Dingler, F. A. *et al.* Two Aldehyde Clearance Systems Are Essential to Prevent Lethal Formaldehyde Accumulation in Mice and Humans. *Mol Cell* **80**, 996-1012 e1019, doi:10.1016/j.molcel.2020.10.012 (2020).
57 Zhou, L., Zhang, W., Sun, Y. & Jia, L. Protein neddylation and its alterations in human cancers for targeted therapy. *Cell Signal* **44**, 92-102, doi:10.1016/j.cellsig.2018.01.009 (2018).
58 Harper, J. W. & Schulman, B. A. Cullin-RING Ubiquitin Ligase Regulatory Circuits: A Quarter Century Beyond the F-Box Hypothesis. *Annu Rev Biochem* **90**, 403-429, doi:10.1146/annurev-biochem-090120-013613 (2021).
59 Ribeiro-Silva, C. *et al.* Ubiquitin and TFIIH-stimulated DDB2 dissociation drives DNA damage handover in nucleotide excision repair. *Nat Commun* **11**, 4868, doi:10.1038/s41467-020-18705-0 (2020).
60 Ohta, T., Michel, J. J., Schottelius, A. J. & Xiong, Y. ROC1, a homolog of APC11, represents a family of cullin partners with an associated ubiquitin ligase activity. *Mol Cell* **3**, 535-541, doi:10.1016/s1097-2765(00)80482-7 (1999).
61 Liu, J., Furukawa, M., Matsumoto, T. & Xiong, Y. NEDD8 modification of CUL1 dissociates p120(CAND1), an inhibitor of CUL1-SKP1 binding and SCF ligases. *Mol Cell* **10**, 1511-1518, doi:10.1016/s1097-2765(02)00783-9 (2002).
62 Luna-Vargas, M. P. *et al.* Enabling high-throughput ligation-independent cloning and protein expression for the family of ubiquitin specific proteases. *J Struct Biol* **175**, 113-119, doi:10.1016/j.jsb.2011.03.017 (2011).
63 Citterio, E. *et al.* Biochemical and biological characterization of wild-type and ATPase-deficient Cockayne syndrome B repair protein. *J Biol Chem* **273**, 11844-11851, doi:10.1074/jbc.273.19.11844 (1998).
64 Kim, R. Q. *et al.* Kinetic analysis of multistep USP7 mechanism shows critical role for target protein in activity. *Nat Commun* **10**, 231, doi:10.1038/s41467-018-08231-5 (2019).
65 Huang, D. T. & Schulman, B. A. Expression, purification, and characterization of the E1 for human NEDD8, the heterodimeric APPBP1-UBA3 complex. *Methods Enzymol* **398**, 9-20, doi:10.1016/S0076-6879(05)98002-6 (2005).
66 Campeau, E. *et al.* A versatile viral system for expression and depletion of proteins in mammalian cells. *PLoS One* **4**, e6529, doi:10.1371/journal.pone.0006529 (2009).
67 Sanjana, N. E., Shalem, O. & Zhang, F. Improved vectors and genome-wide libraries for CRISPR screening. *Nat Methods* **11**, 783-784, doi:10.1038/nmeth.3047 (2014).
68 Pines, A. *et al.* PARP1 promotes nucleotide excision repair through DDB2 stabilization and recruitment of ALC1. *J Cell Biol* **199**, 235-249, doi:10.1083/jcb.201112132 (2012).
69 Jumper, J. *et al.* Highly accurate protein structure prediction with AlphaFold. *Nature* **596**, 583-589, doi:10.1038/s41586-021-03819-2 (2021).
70 Pettersen, E. F. *et al.* UCSF Chimera--a visualization system for exploratory research and analysis. *J Comput Chem* **25**, 1605-1612, doi:10.1002/jcc.20084 (2004).
71 Emsley, P., Lohkamp, B., Scott, W. G. & Cowtan, K. Features and development of Coot. *Acta Crystallogr D Biol Crystallogr* **66**, 486-501, doi:10.1107/S0907444910007493 (2010).
72 Punjani, A., Rubinstein, J. L., Fleet, D. J. & Brubaker, M. A. cryoSPARC: algorithms for rapid unsupervised cryo-EM structure determination. *Nat Methods* **14**, 290-296, doi:10.1038/nmeth.4169 (2017).
73 Rohou, A. & Grigorieff, N. CTFFIND4: Fast and accurate defocus estimation from electron micrographs. *J Struct Biol* **192**, 216-221, doi:10.1016/j.jsb.2015.08.008 (2015).
74 Cox, J. *et al.* Andromeda: a peptide search engine integrated into the MaxQuant environment. *J Proteome Res* **10**, 1794-1805, doi:10.1021/pr101065j (2011).

75 Zheng, S. Q. *et al.* MotionCor2: anisotropic correction of beam-induced motion for improved cryo-electron microscopy. *Nat Methods* **14**, 331-332, doi:10.1038/nmeth.4193 (2017).
76 Joosten, R. P., Long, F., Murshudov, G. N. & Perrakis, A. The PDB_REDO server for macromolecular structure model optimization. *IUCrJ* **1**, 213-220, doi:10.1107/S2052252514009324 (2014).
77 Tyanova, S. *et al.* The Perseus computational platform for comprehensive analysis of (prote)omics data. *Nat Methods* **13**, 731-740, doi:10.1038/nmeth.3901 (2016).
78 Adams, P. D. *et al.* PHENIX: a comprehensive Python-based system for macromolecular structure solution. *Acta Crystallogr D Biol Crystallogr* **66**, 213-221, doi:10.1107/S0907444909052925 (2010).
79 Zivanov, J. *et al.* New tools for automated high-resolution cryo-EM structure determination in RELION-3. *Elife* **7**, doi:10.7554/eLife.42166 (2018).
80 Bepler, T. *et al.* Positive-unlabeled convolutional neural networks for particle picking in cryo-electron micrographs. *Nat Methods* **16**, 1153-1160, doi:10.1038/s41592-019-0575-8 (2019).
81 van Cuijk, L. *et al.* SUMO and ubiquitin-dependent XPC exchange drives nucleotide excision repair. *Nat Commun* **6**, 7499, doi:10.1038/ncomms8499 (2015).
82 Schwertman, P. *et al.* An immunoaffinity purification method for the proteomic analysis of ubiquitinated protein complexes. *Anal Biochem* **440**, 227-236, doi:10.1016/j.ab.2013.05.020 (2013).
83 Weissmann, F. *et al.* biGBac enables rapid gene assembly for the expression of large multisubunit protein complexes. *Proc Natl Acad Sci U S A* **113**, E2564-2569, doi:10.1073/pnas.1604935113 (2016).
84 Kastner, B. *et al.* GraFix: sample preparation for single-particle electron cryomicroscopy. *Nat Methods* **5**, 53-55, doi:10.1038/nmeth1139 (2008).
85 Banchenko, S. *et al.* Structural insights into Cullin4-RING ubiquitin ligase remodelling by Vpr from simian immunodeficiency viruses. *PLoS Pathog* **17**, e1009775, doi:10.1371/journal.ppat.1009775 (2021).

Fig. 1

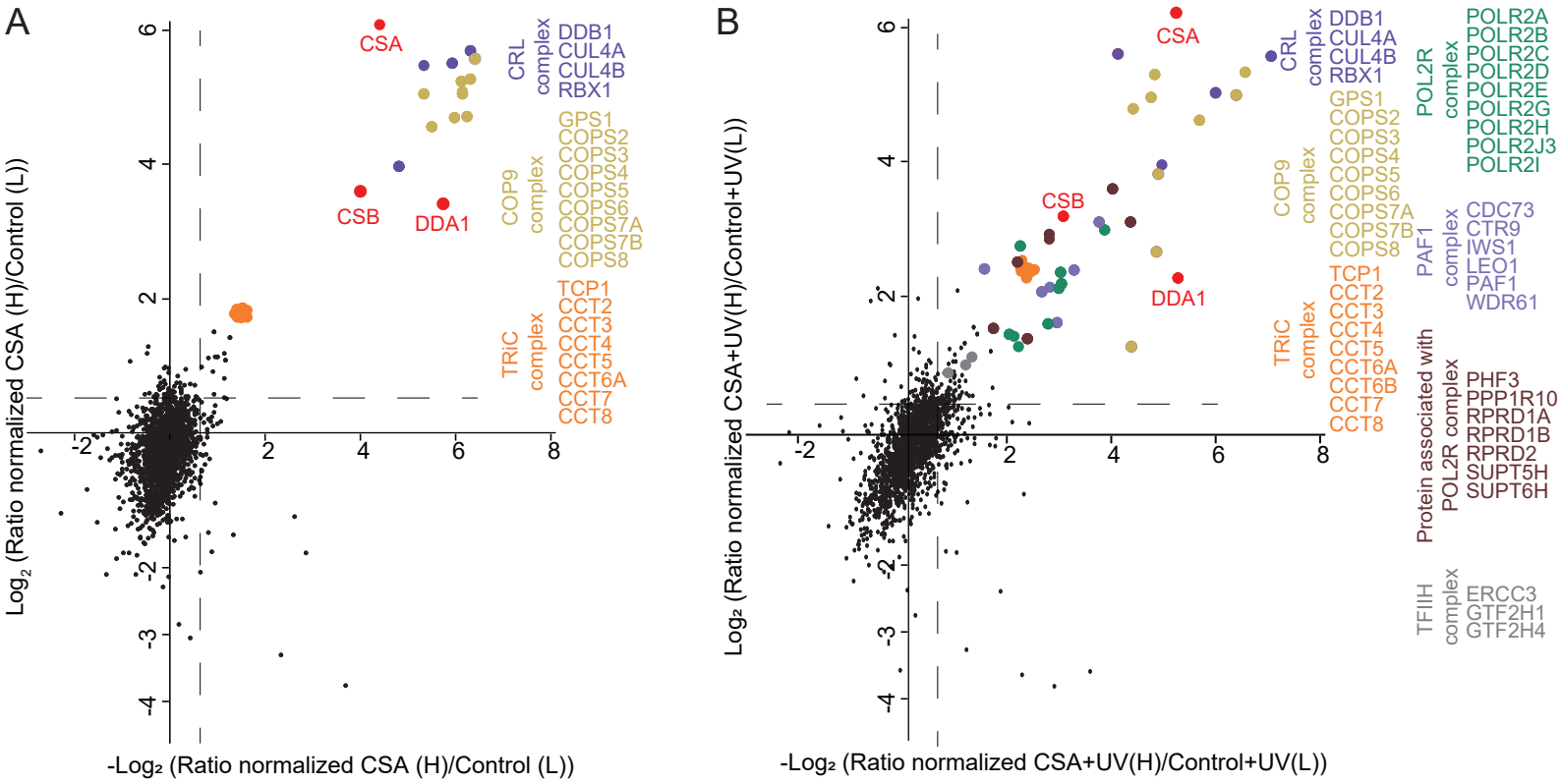
A
CSA
CSB
DDA1
CRL complex
DDB1
CUL4A
CUL4B
RBX1
COP9 complex
GPS1
COPS2
COPS3
COPS4
COPS5
COPS6
COPS7A
COPS7B
COPS8
TRiC complex
TCP1
CCT2
CCT3
CCT4
CCT5
CCT6A
CCT7
CCT8
Log2 (Ratio normalized CSA (H)/Control (L))
-Log2 (Ratio normalized CSA (H)/Control (L))
B
CSA
CSB
DDA1
CRL complex
DDB1
CUL4A
CUL4B
RBX1
COP9 complex
GPS1
COPS2
COPS3
COPS4
COPS5
COPS6
COPS7A
COPS7B
COPS8
TRiC complex
TCP1
CCT2
CCT3
CCT4
CCT5
CCT6A
CCT6B
CCT7
CCT8
POL2R complex
POLR2A
POLR2B
POLR2C
POLR2D
POLR2E
POLR2G
POLR2H
POLR2J3
POLR2I
PAF1 complex
CDC73
CTR9
IWS1
LEO1
PAF1
WDR61
Protein associated with POL2R complex
PHF3
PPP1R10
RPRD1A
RPRD1B
RPRD2
SUPT5H
SUPT6H
TFIIH complex
ERCC3
GTF2H1
GTF2H4
Log2 (Ratio normalized CSA+UV(H)/Control+UV(L))
-Log2 (Ratio normalized CSA+UV(H)/Control+UV(L))

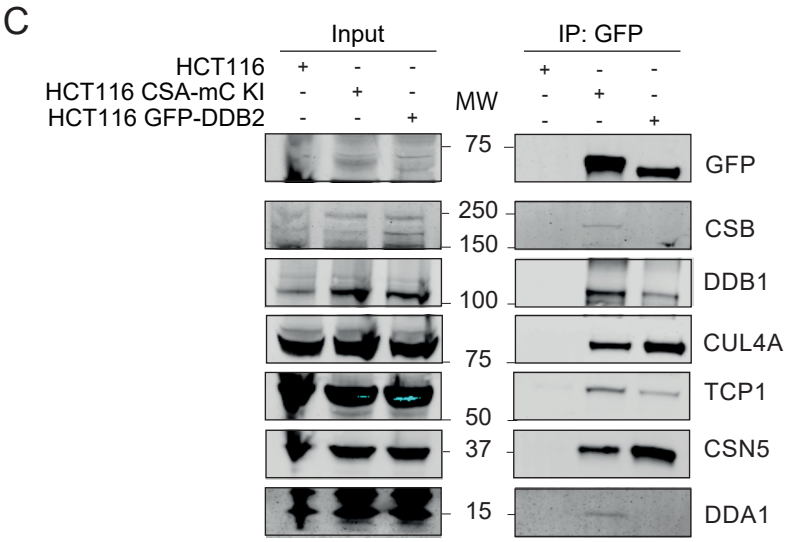
C
Input
IP: GFP
HCT116
HCT116 CSA-mC KI
HCT116 GFP-DDB2
MW
75
250
150
100
75
50
37
15
GFP
CSB
DDB1
CUL4A
TCP1
CSN5
DDA1

Fig. 2

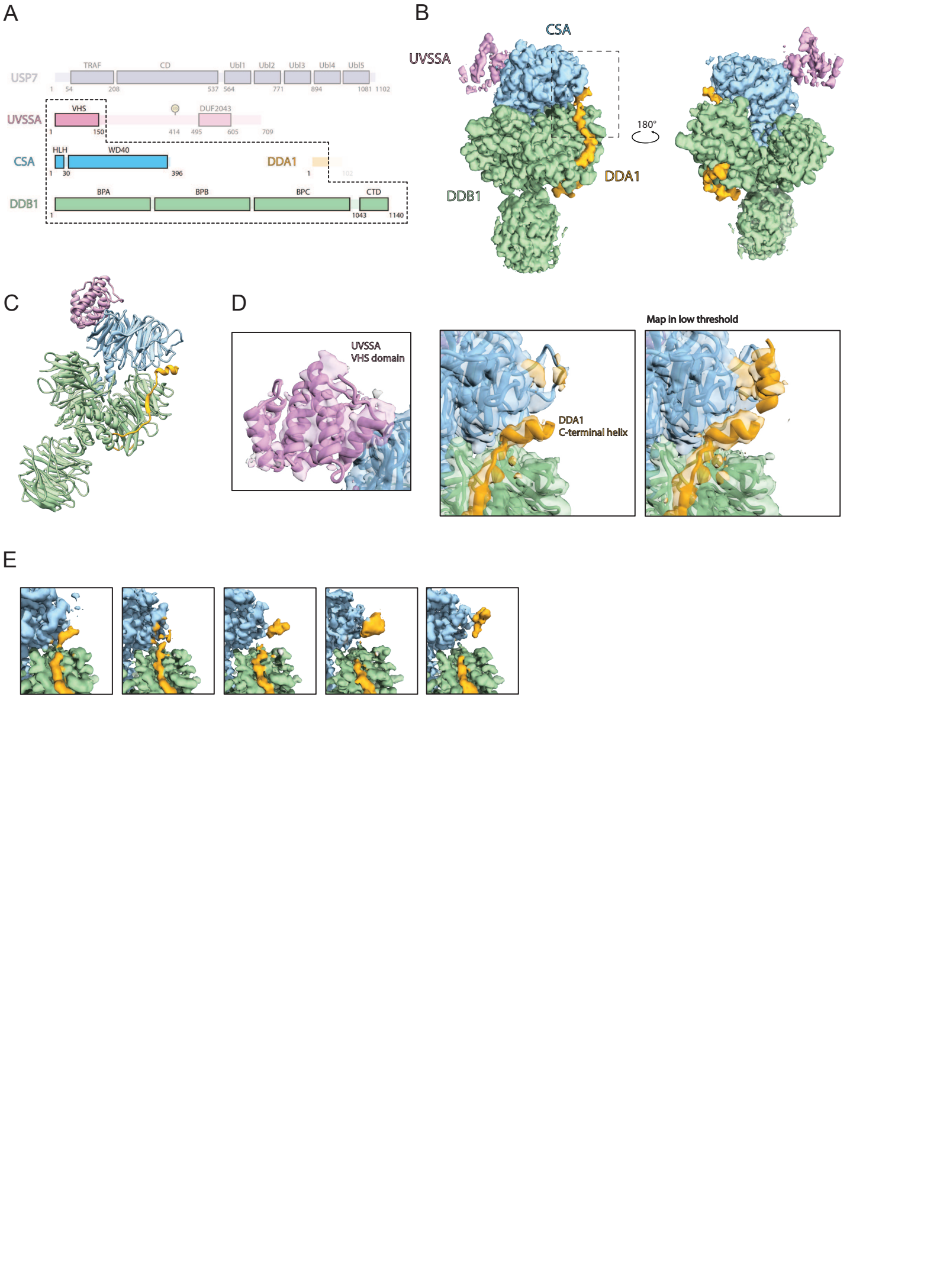
A
USP7
TRAF
CD
Ubl1
Ubl2
Ubl3
Ubl4
Ubl5
1
54
208
537
564
771
894
1081
1102
UVSSA
VHS
DUF2043
1
150
414
495
605
709
CSA
HLH
WD40
1
30
396
DDA1
1
102
DDB1
BPA
BPB
BPC
CTD
1
1043
1140
B
CSA
UVSSA
DDA1
DDB1
180°
C
D
UVSSA
VHS domain
DDA1
C-terminal helix
Map in low threshold
E

Fig. 3

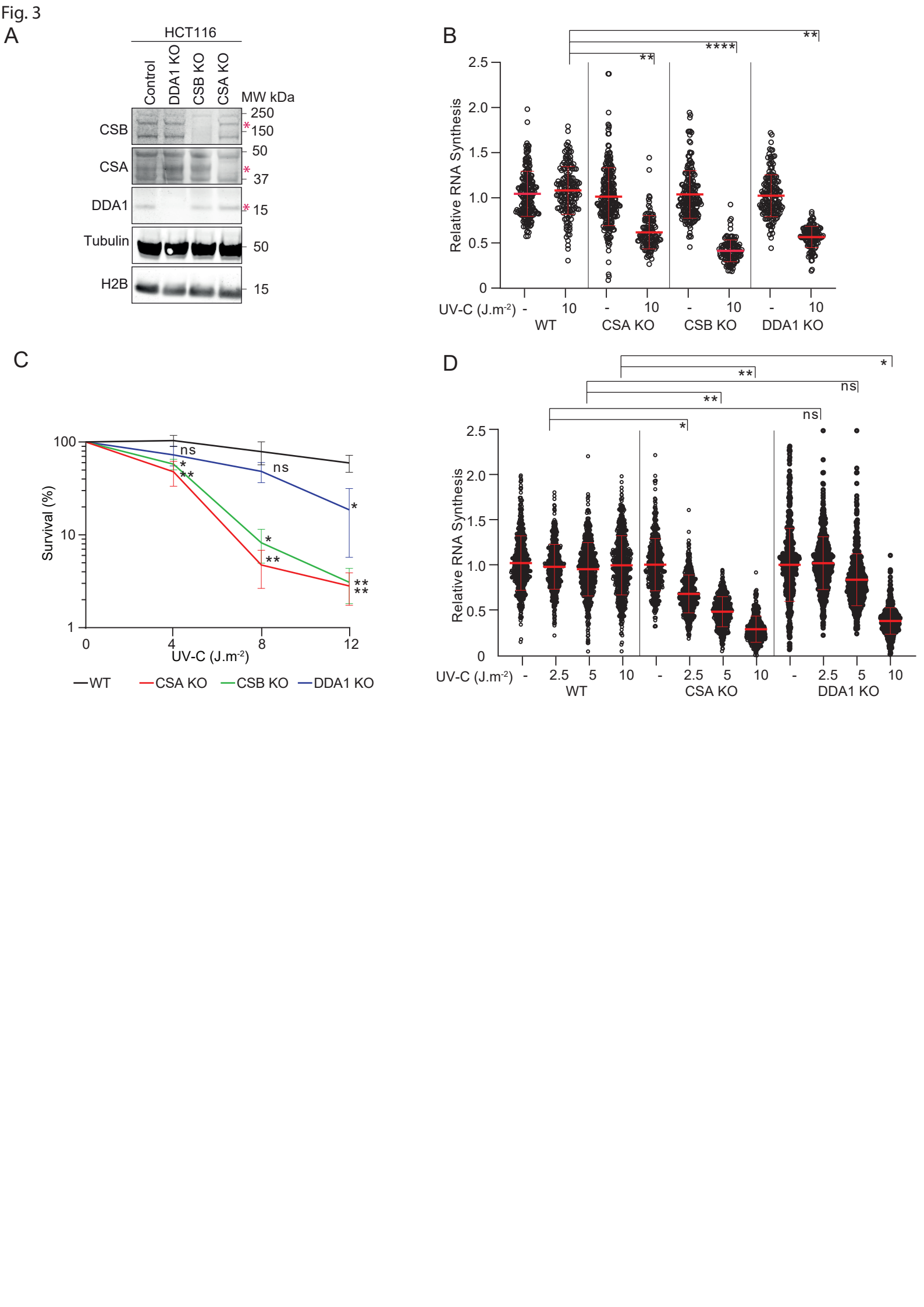
A
HCT116
Control
DDA1 KO
CSB KO
CSA KO
MW kDa
CSB
250
150
CSA
50
37
DDA1
15
Tubulin
50
H2B
15
B
Relative RNA Synthesis
UV-C (J.m-2)
WT
CSA KO
CSB KO
DDA1 KO
C
Survival (%)
UV-C (J.m-2)
WT
CSA KO
CSB KO
DDA1 KO
D
Relative RNA Synthesis
UV-C (J.m-2)
WT
CSA KO
DDA1 KO

Fig. 4

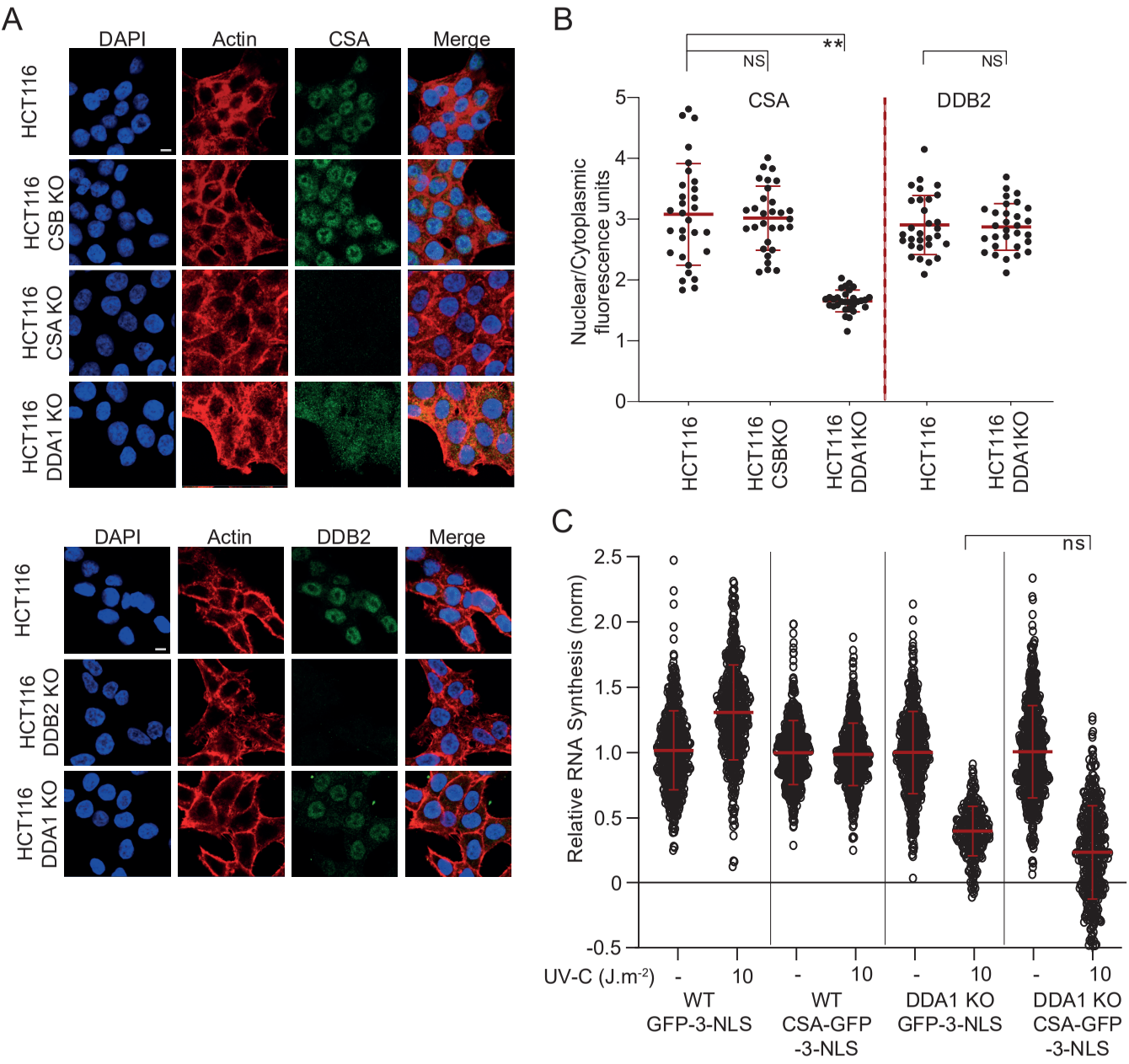
A
DAPI
Actin
CSA
Merge
HCT116
HCT116 CSB KO
HCT116 CSA KO
HCT116 DDA1 KO
DAPI
Actin
DDB2
Merge
HCT116
HCT116 DDB2 KO
HCT116 DDA1 KO
B
NS
**
NS
CSA
DDB2
Nuclear/Cytoplasmic fluorescence units
0
1
2
3
4
5
HCT116
HCT116 CSBKO
HCT116 DDA1KO
HCT116
HCT116 DDA1KO
C
ns
Relative RNA Synthesis (norm)
2.5
2.0
1.5
1.0
0.5
0
-0.5
UV-C (J.m-2)
-
10
-
10
-
10
-
10
WT GFP-3-NLS
WT CSA-GFP -3-NLS
DDA1 KO GFP-3-NLS
DDA1 KO CSA-GFP -3-NLS

Fig. 5

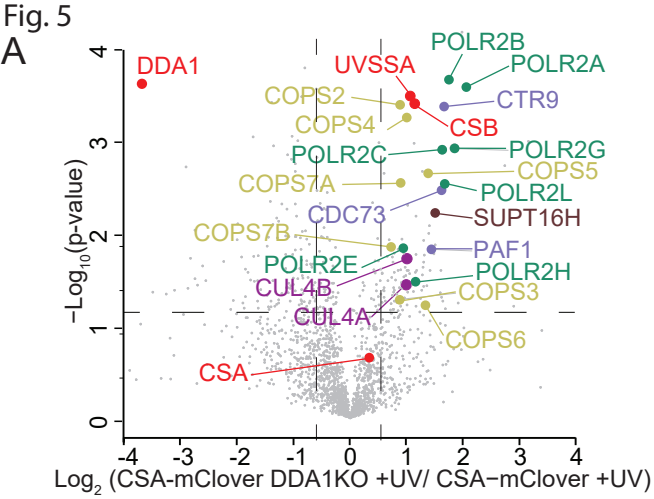
A
DDA1
UVSSA
POLR2B
POLR2A
COPS2
CTR9
COPS4
CSB
POLR2C
POLR2G
COPS7A
COPS5
POLR2L
CDC73
SUPT16H
COPS7B
PAF1
POLR2E
POLR2H
CUL4B
COPS3
CUL4A
COPS6
CSA
−Log10(p-value)
Log2 (CSA-mClover DDA1KO +UV/ CSA−mClover +UV)

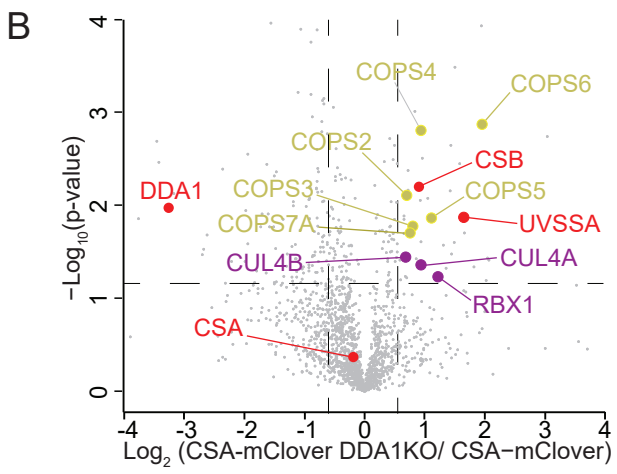
B
COPS4
COPS6
COPS2
CSB
DDA1
COPS3
COPS5
COPS7A
UVSSA
CUL4B
CUL4A
RBX1
CSA
−Log10(p-value)
Log2 (CSA-mClover DDA1KO/ CSA−mClover)

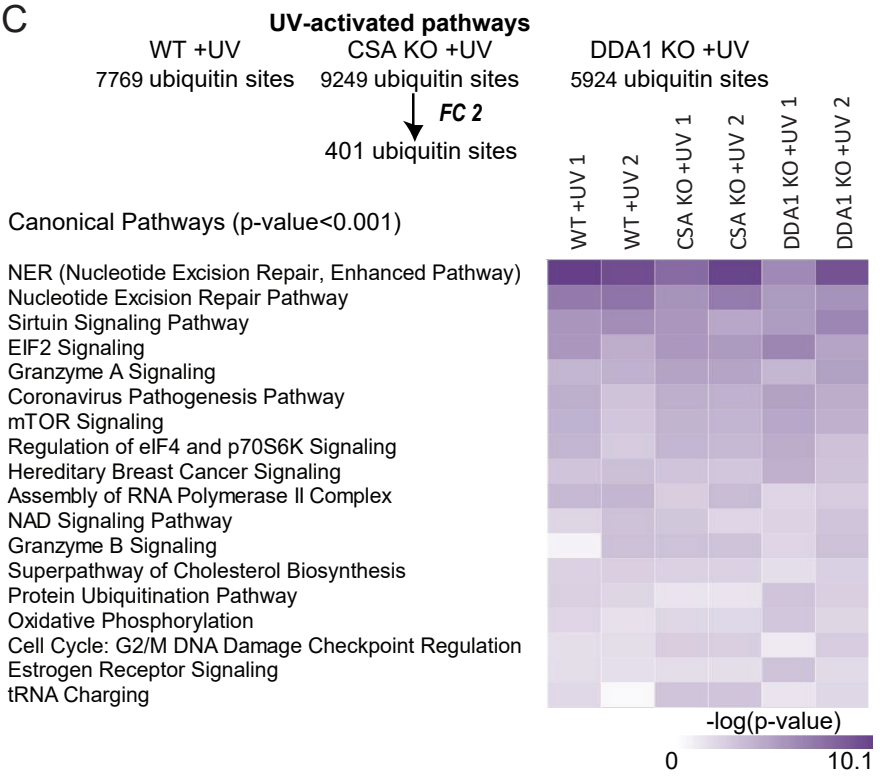
C
UV-activated pathways
WT +UV
7769 ubiquitin sites
CSA KO +UV
9249 ubiquitin sites
DDA1 KO +UV
5924 ubiquitin sites
FC 2
401 ubiquitin sites
Canonical Pathways (p-value<0.001)
NER (Nucleotide Excision Repair, Enhanced Pathway)
Nucleotide Excision Repair Pathway
Sirtuin Signaling Pathway
EIF2 Signaling
Granzyme A Signaling
Coronavirus Pathogenesis Pathway
mTOR Signaling
Regulation of eIF4 and p70S6K Signaling
Hereditary Breast Cancer Signaling
Assembly of RNA Polymerase II Complex
NAD Signaling Pathway
Granzyme B Signaling
Superpathway of Cholesterol Biosynthesis
Protein Ubiquitination Pathway
Oxidative Phosphorylation
Cell Cycle: G2/M DNA Damage Checkpoint Regulation
Estrogen Receptor Signaling
tRNA Charging
WT +UV 1
WT +UV 2
CSA KO +UV 1
CSA KO +UV 2
DDA1 KO +UV 1
DDA1 KO +UV 2
-log(p-value)
0
10.1

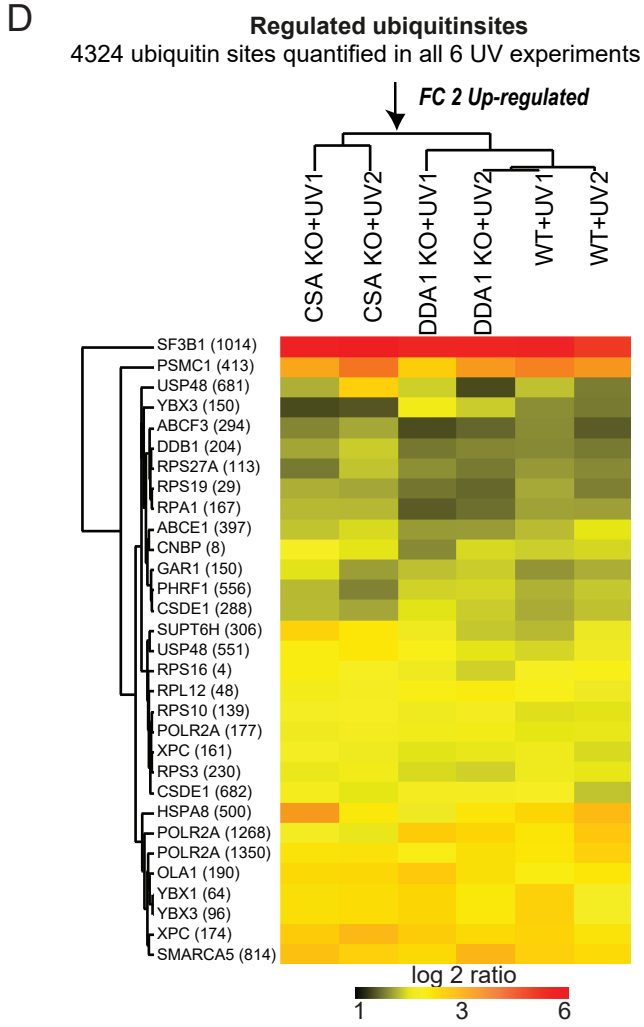
D
Regulated ubiquitinsites
4324 ubiquitin sites quantified in all 6 UV experiments
FC 2 Up-regulated
CSA KO+UV1
CSA KO+UV2
DDA1 KO+UV1
DDA1 KO+UV2
WT+UV1
WT+UV2
SF3B1 (1014)
PSMC1 (413)
USP48 (681)
YBX3 (150)
ABCF3 (294)
DDB1 (204)
RPS27A (113)
RPS19 (29)
RPA1 (167)
ABCE1 (397)
CNBP (8)
GAR1 (150)
PHRF1 (556)
CSDE1 (288)
SUPT6H (306)
USP48 (551)
RPS16 (4)
RPL12 (48)
RPS10 (139)
POLR2A (177)
XPC (161)
RPS3 (230)
CSDE1 (682)
HSPA8 (500)
POLR2A (1268)
POLR2A (1350)
OLA1 (190)
YBX1 (64)
YBX3 (96)
XPC (174)
SMARCA5 (814)
log 2 ratio
1
3
6

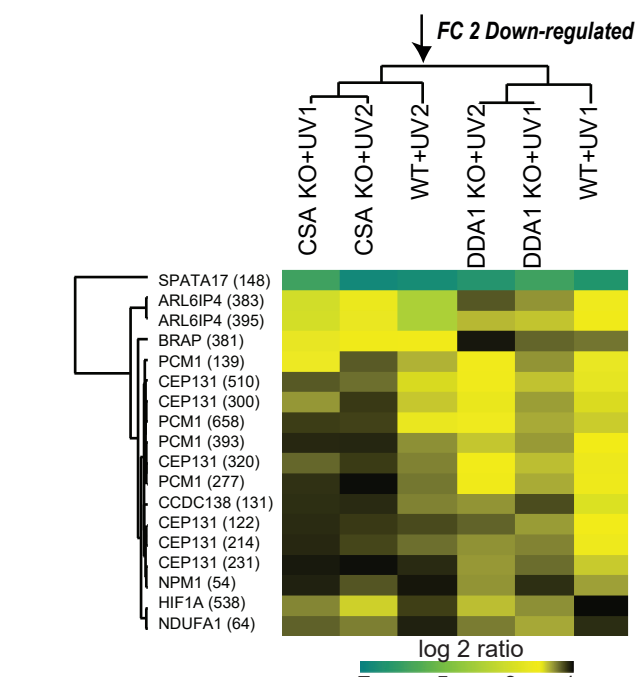
FC 2 Down-regulated
CSA KO+UV1
CSA KO+UV2
WT+UV2
DDA1 KO+UV2
DDA1 KO+UV1
WT+UV1
SPATA17 (148)
ARL6IP4 (383)
ARL6IP4 (395)
BRAP (381)
PCM1 (139)
CEP131 (510)
CEP131 (300)
PCM1 (658)
PCM1 (393)
CEP131 (320)
PCM1 (277)
CCDC138 (131)
CEP131 (122)
CEP131 (214)
CEP131 (231)
NPM1 (54)
HIF1A (538)
NDUFA1 (64)
log 2 ratio
-7
-5
-3
-1

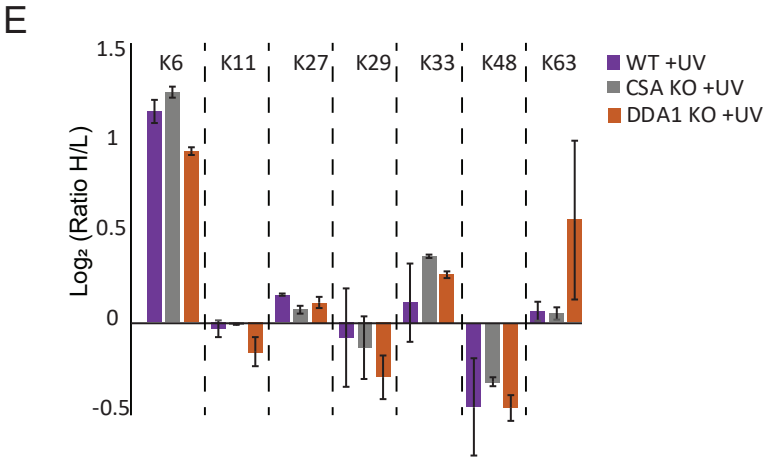
E
K6
K11
K27
K29
K33
K48
K63
WT +UV
CSA KO +UV
DDA1 KO +UV
Log2 (Ratio H/L)

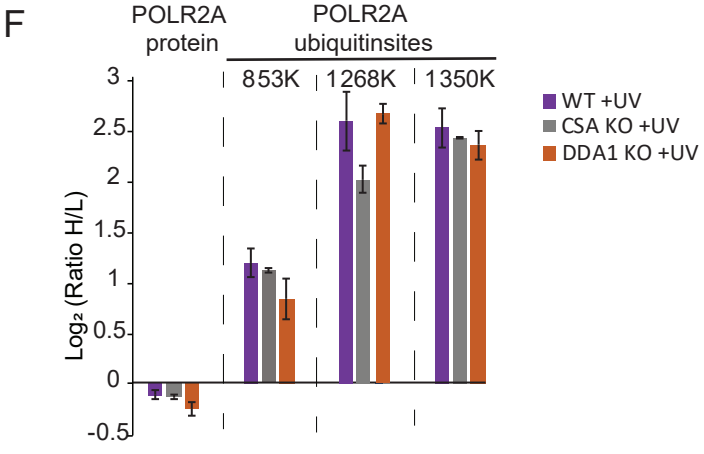
F
POLR2A protein
POLR2A ubiquitinsites
853K
1268K
1350K
WT +UV
CSA KO +UV
DDA1 KO +UV
Log2 (Ratio H/L)

Fig. 6

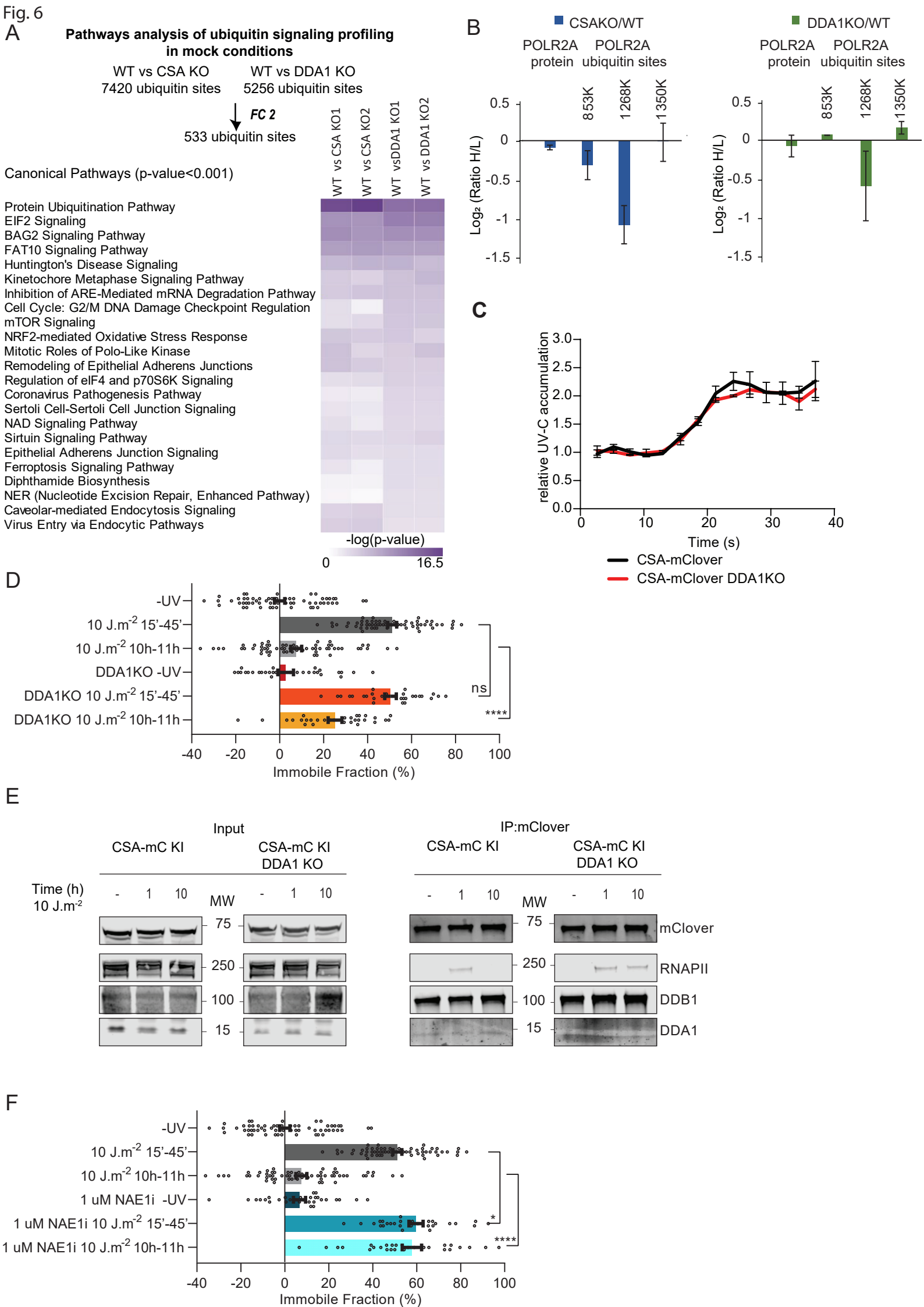
A
Pathways analysis of ubiquitin signaling profiling in mock conditions
WT vs CSA KO
7420 ubiquitin sites
WT vs DDA1 KO
5256 ubiquitin sites
FC 2
533 ubiquitin sites
Canonical Pathways (p-value<0.001)
WT vs CSA KO1
WT vs CSA KO2
WT vsDDA1 KO1
WT vs DDA1 KO2
Protein Ubiquitination Pathway
EIF2 Signaling
BAG2 Signaling Pathway
FAT10 Signaling Pathway
Huntington's Disease Signaling
Kinetochore Metaphase Signaling Pathway
Inhibition of ARE-Mediated mRNA Degradation Pathway
Cell Cycle: G2/M DNA Damage Checkpoint Regulation
mTOR Signaling
NRF2-mediated Oxidative Stress Response
Mitotic Roles of Polo-Like Kinase
Remodeling of Epithelial Adherens Junctions
Regulation of eIF4 and p70S6K Signaling
Coronavirus Pathogenesis Pathway
Sertoli Cell-Sertoli Cell Junction Signaling
NAD Signaling Pathway
Sirtuin Signaling Pathway
Epithelial Adherens Junction Signaling
Ferroptosis Signaling Pathway
Diphthamide Biosynthesis
NER (Nucleotide Excision Repair, Enhanced Pathway)
Caveolar-mediated Endocytosis Signaling
Virus Entry via Endocytic Pathways
-log(p-value)
0
16.5
B
CSAKO/WT
DDA1KO/WT
POLR2A protein
POLR2A ubiquitin sites
853K
1268K
1350K
Log2 (Ratio H/L)
C
relative UV-C accumulation
Time (s)
CSA-mClover
CSA-mClover DDA1KO
D
-UV
10 J.m-2 15'-45'
10 J.m-2 10h-11h
DDA1KO -UV
DDA1KO 10 J.m-2 15'-45'
DDA1KO 10 J.m-2 10h-11h
ns
****
Immobile Fraction (%)
E
Input
IP:mClover
CSA-mC KI
CSA-mC KI DDA1 KO
Time (h) 10 J.m-2
MW
mClover
RNAPII
DDB1
DDA1
F
-UV
10 J.m-2 15'-45'
10 J.m-2 10h-11h
1 uM NAE1i -UV
1 uM NAE1i 10 J.m-2 15'-45'
1 uM NAE1i 10 J.m-2 10h-11h
*
****
Immobile Fraction (%)

Supplementary Fig. 1

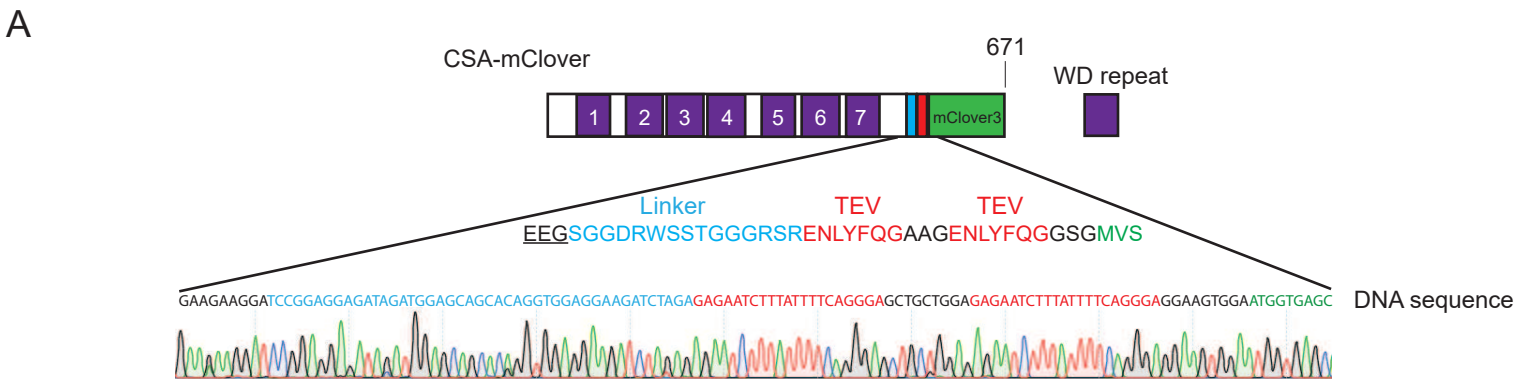

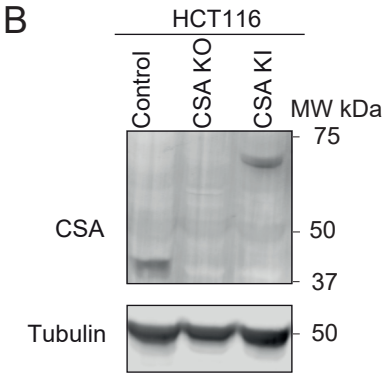

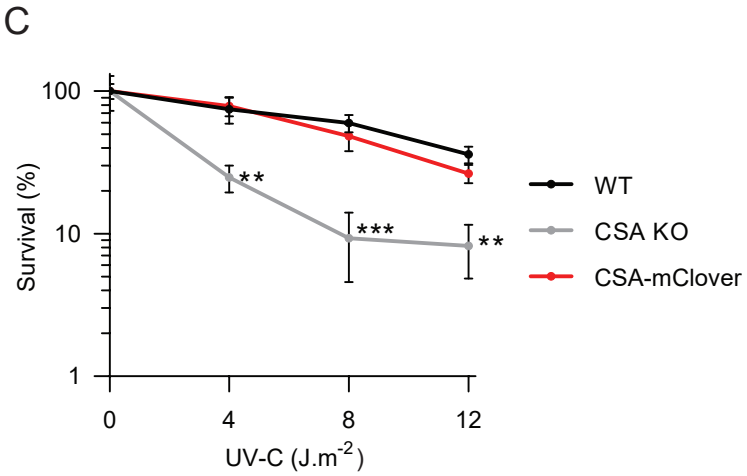

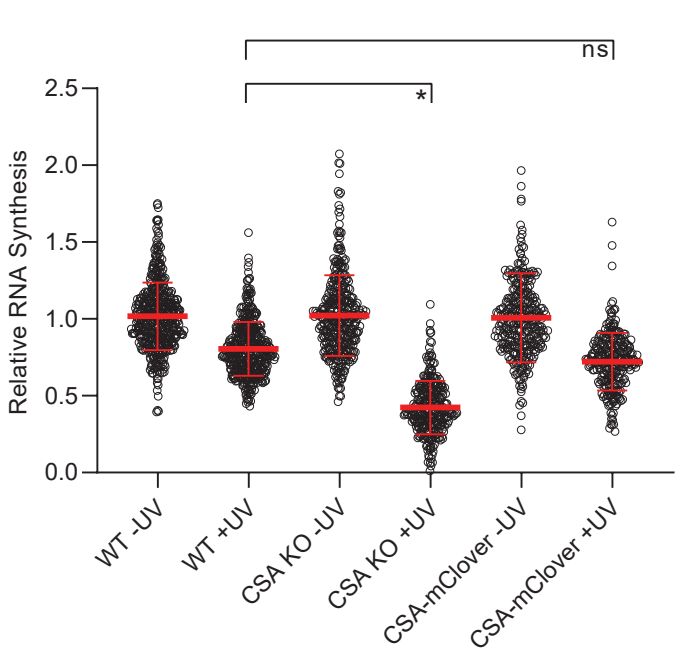

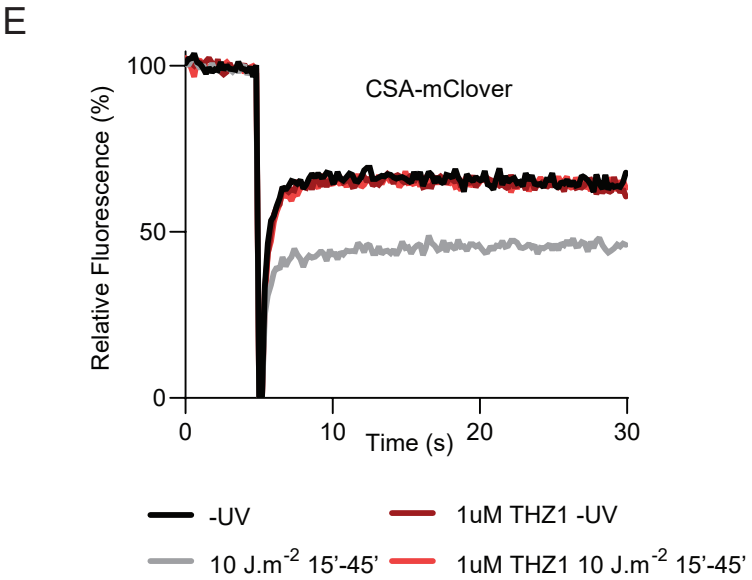

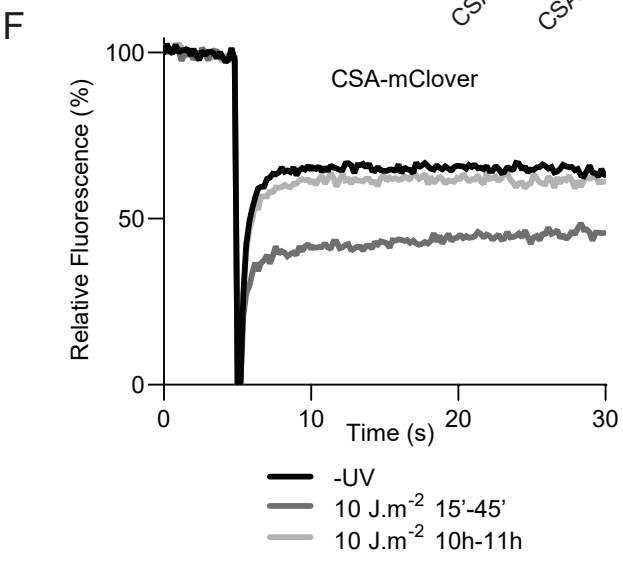

Supplementary Fig. 2

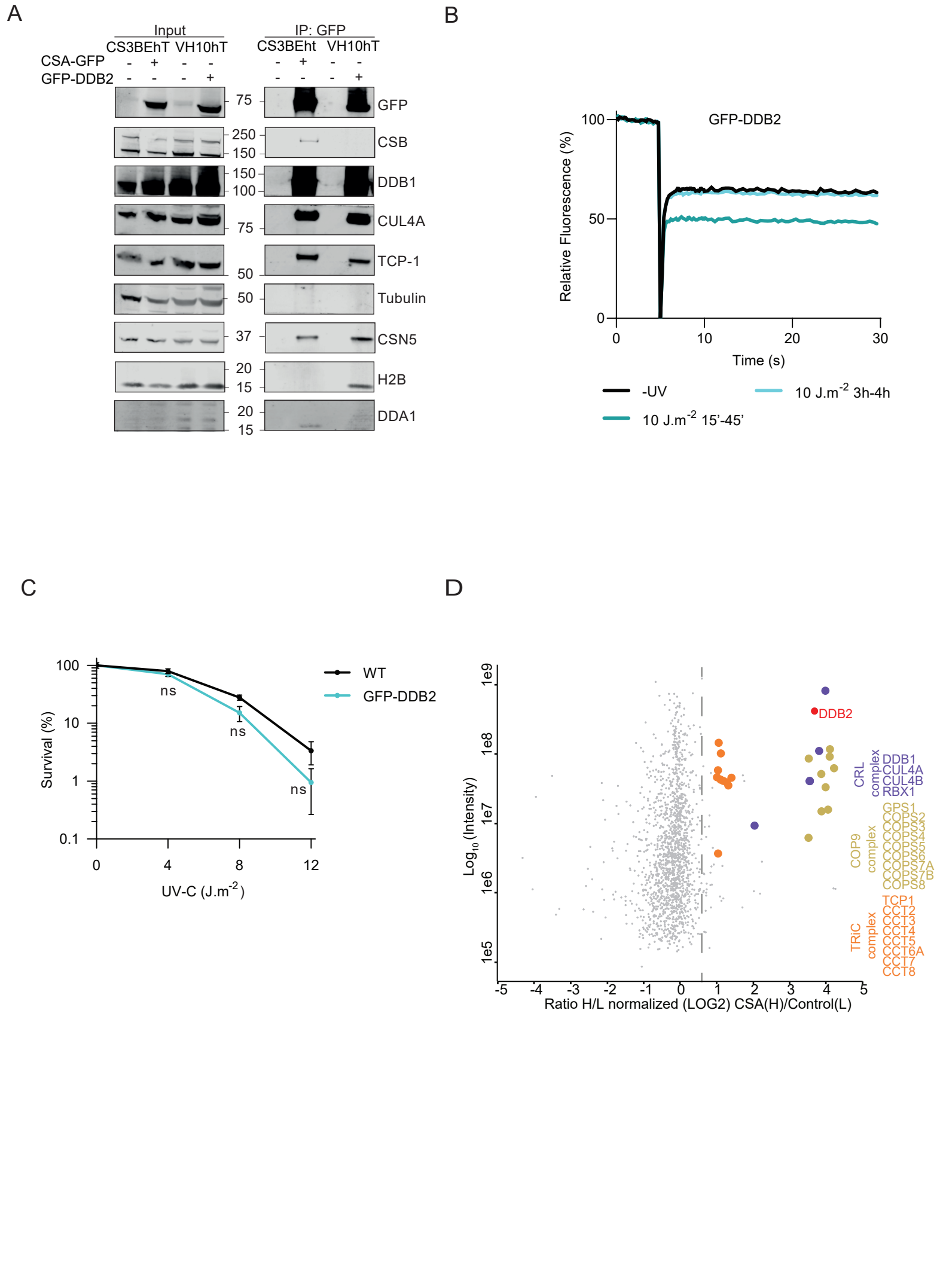

Supplementary Fig. 3

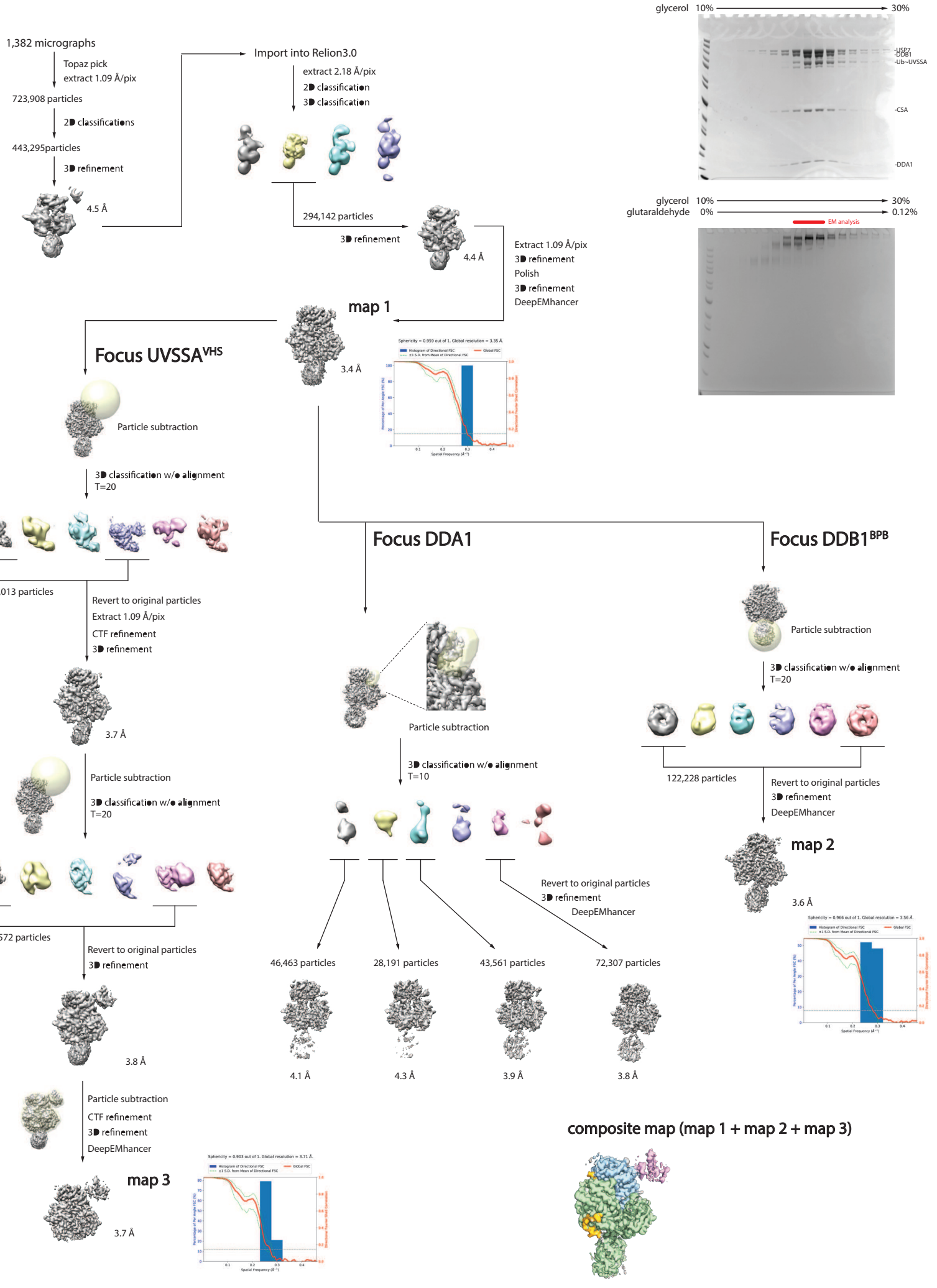

Supplementary Fig. 4

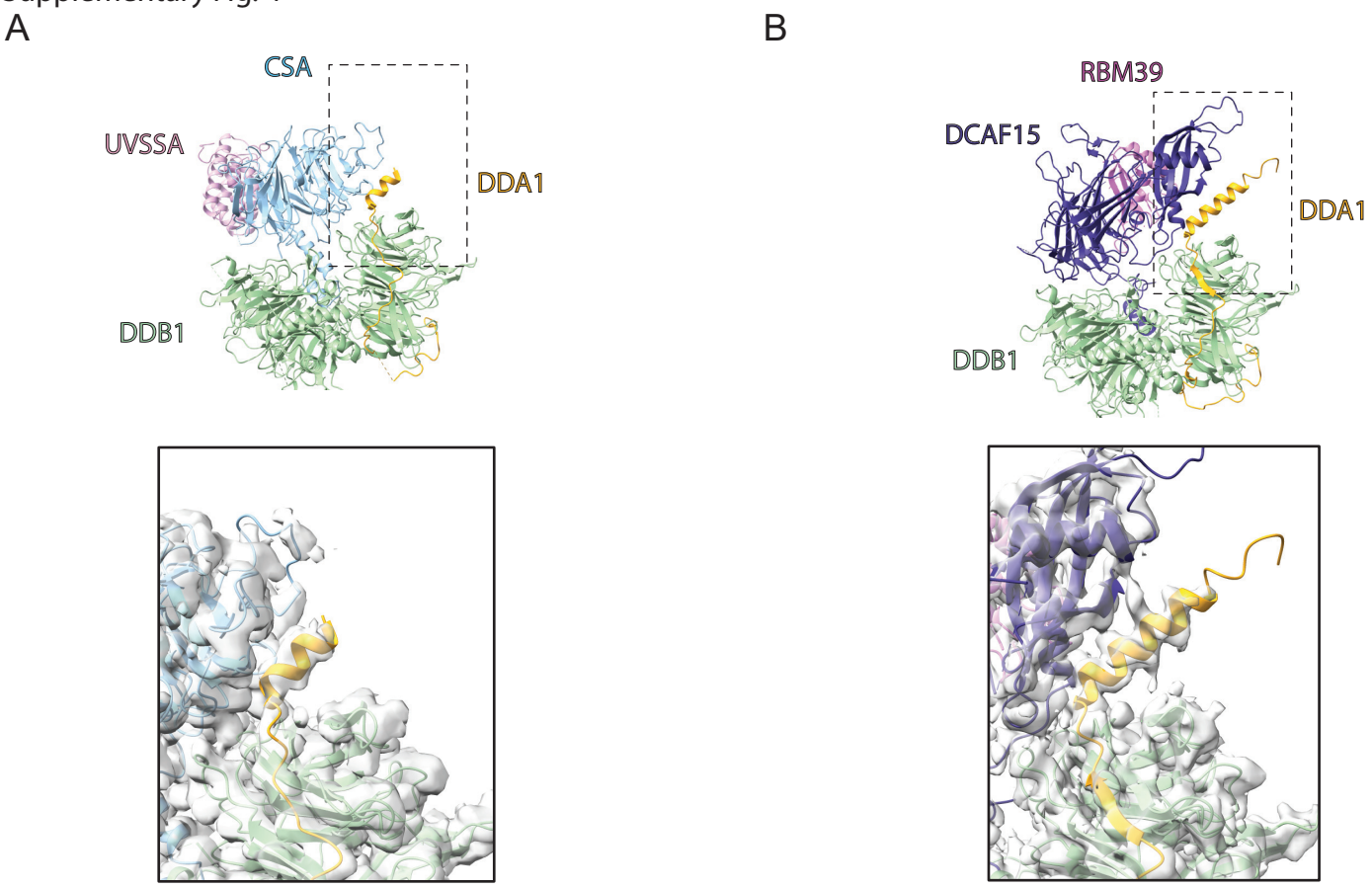

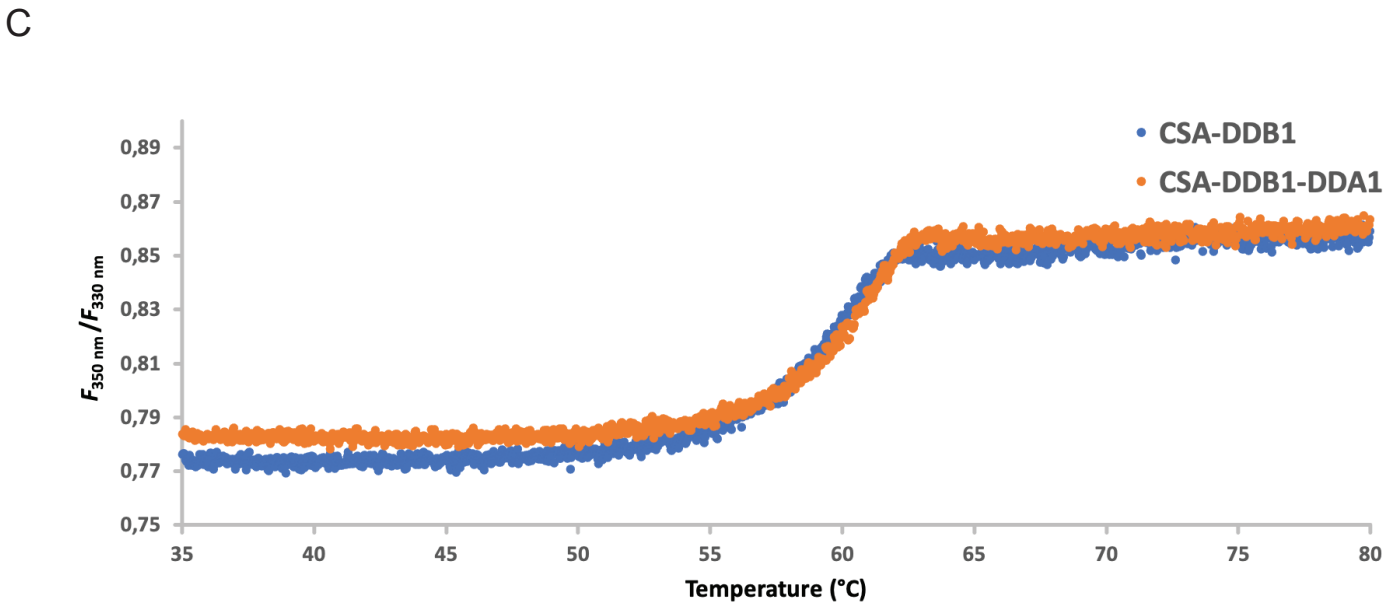

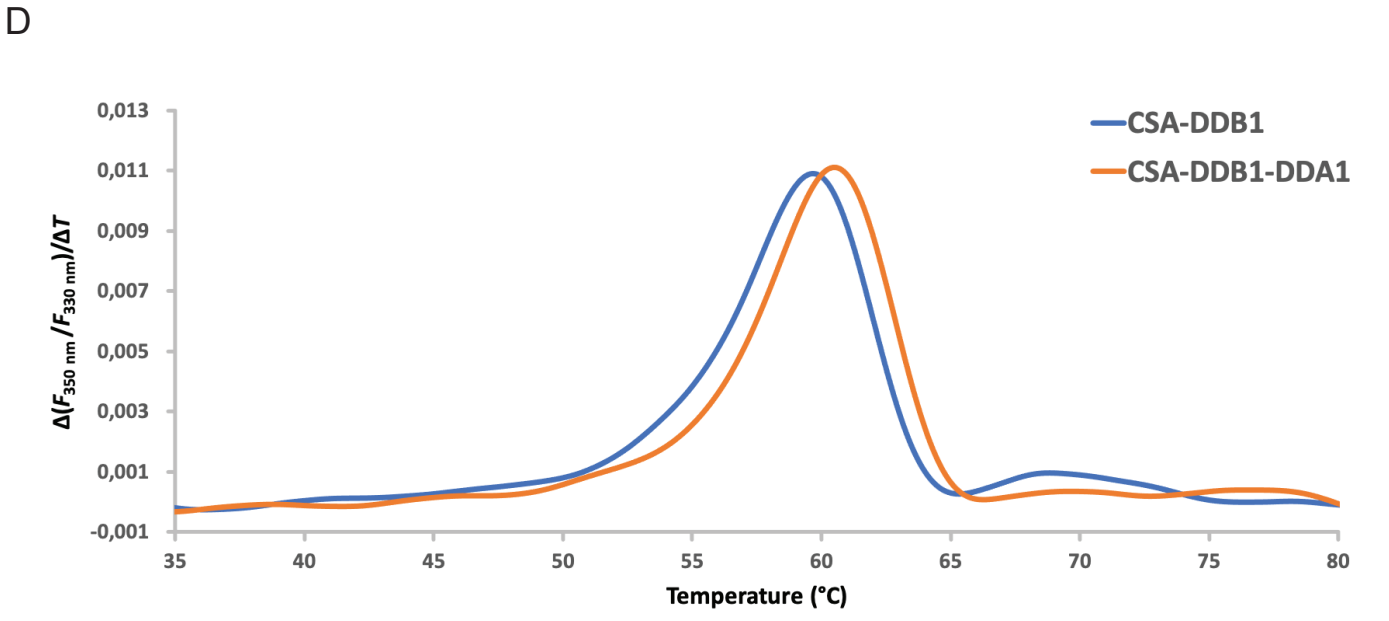

Supplementary Fig. 5

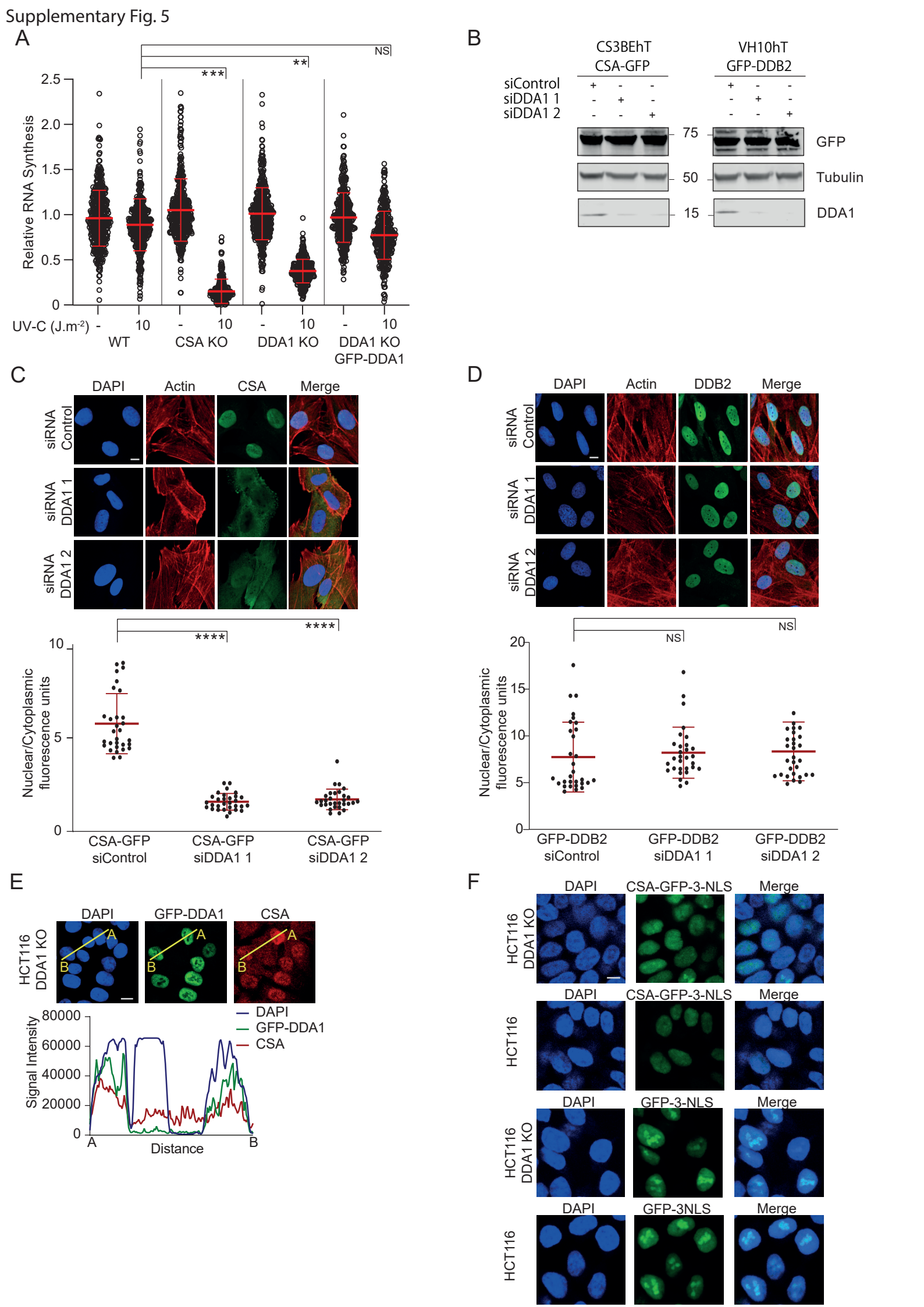

Supplementary Fig. 6

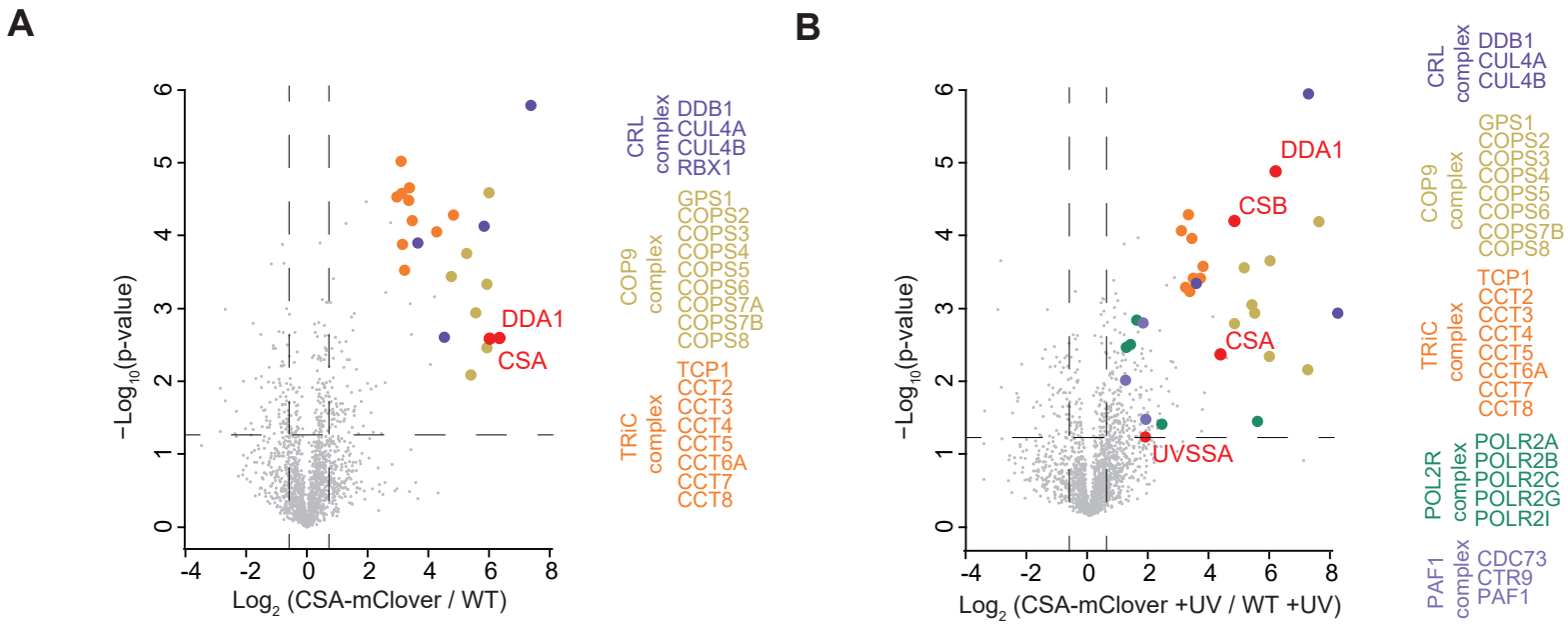

C

		CSAmClover/DDA1KO vs CSAmClover t-test Difference (Log_2)	CSAmClover/DDA1KO +UV vs CSAmClover +UV t-test Difference (Log_2)
	CSA (ERCC8)	**-0.175833**	**0.594915**
	DDB1	0.384607	0.464457
	DDA1	-3.23592	-3.68452
TRiC complex	TCP1	0.211027	0.454005
	CCT2	0.190139	0.436647
	CCT3	0.215641	0.336879
	CCT4	0.121384	0.393906
	CCT5	0.222755	0.31822
	CCT6A	0.220267	0.274117
	CCT7	0.251577	0.372348
	CCT8	0.1789	0.344252

Supplementary Fig. 7

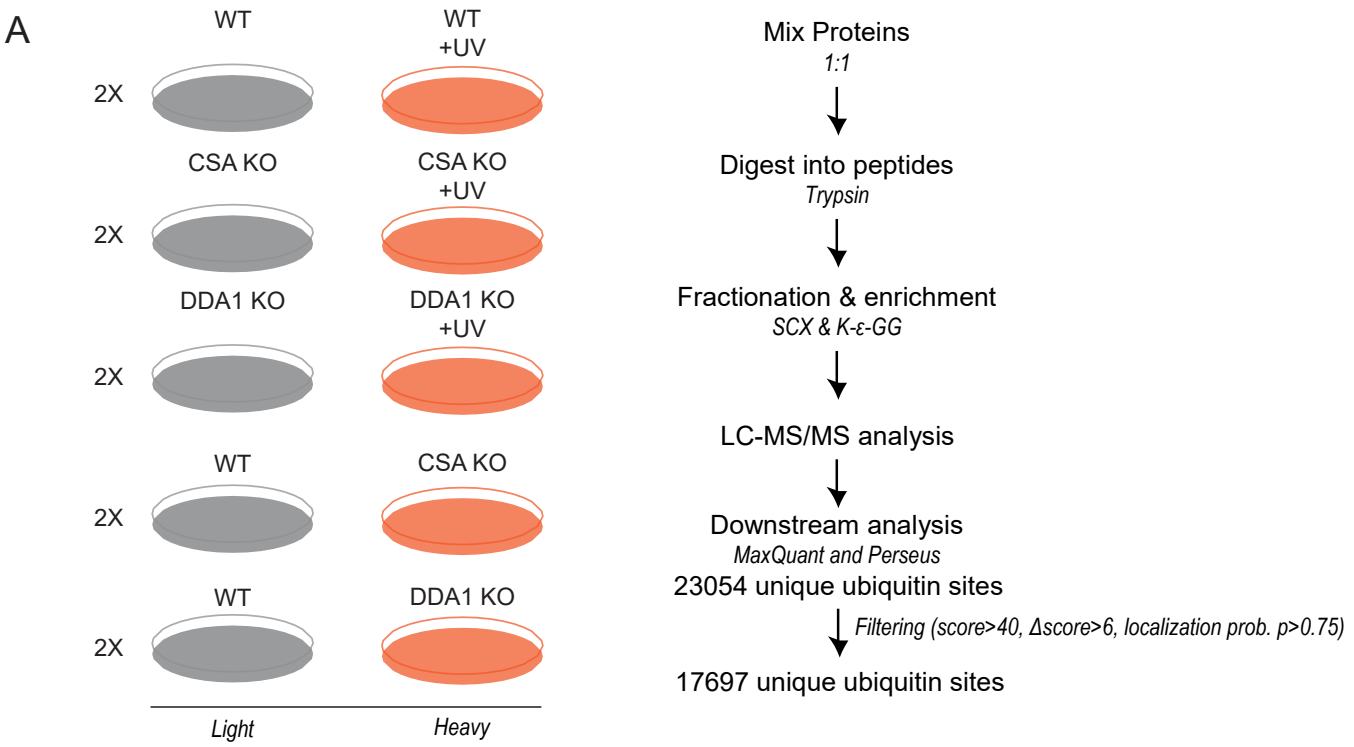

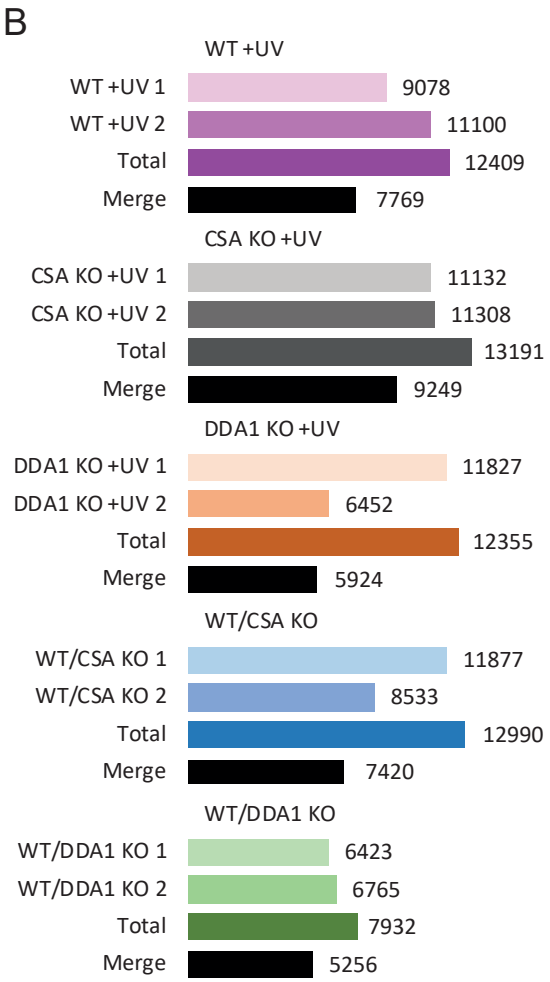

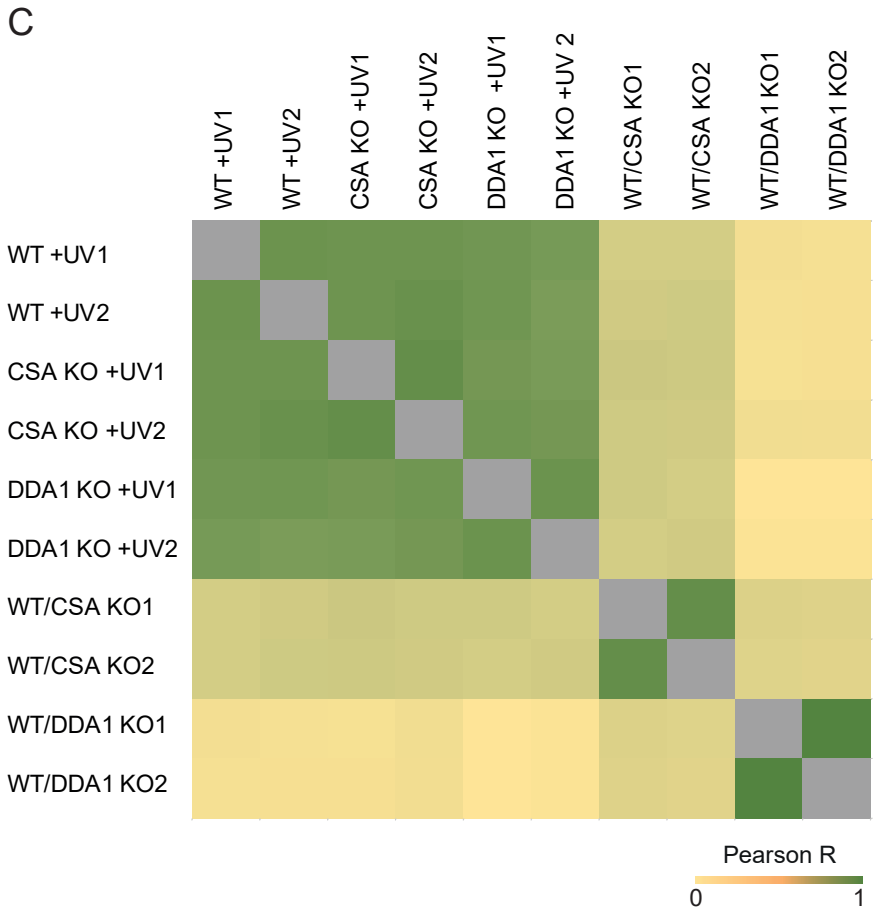

Supplementary Fig. 8

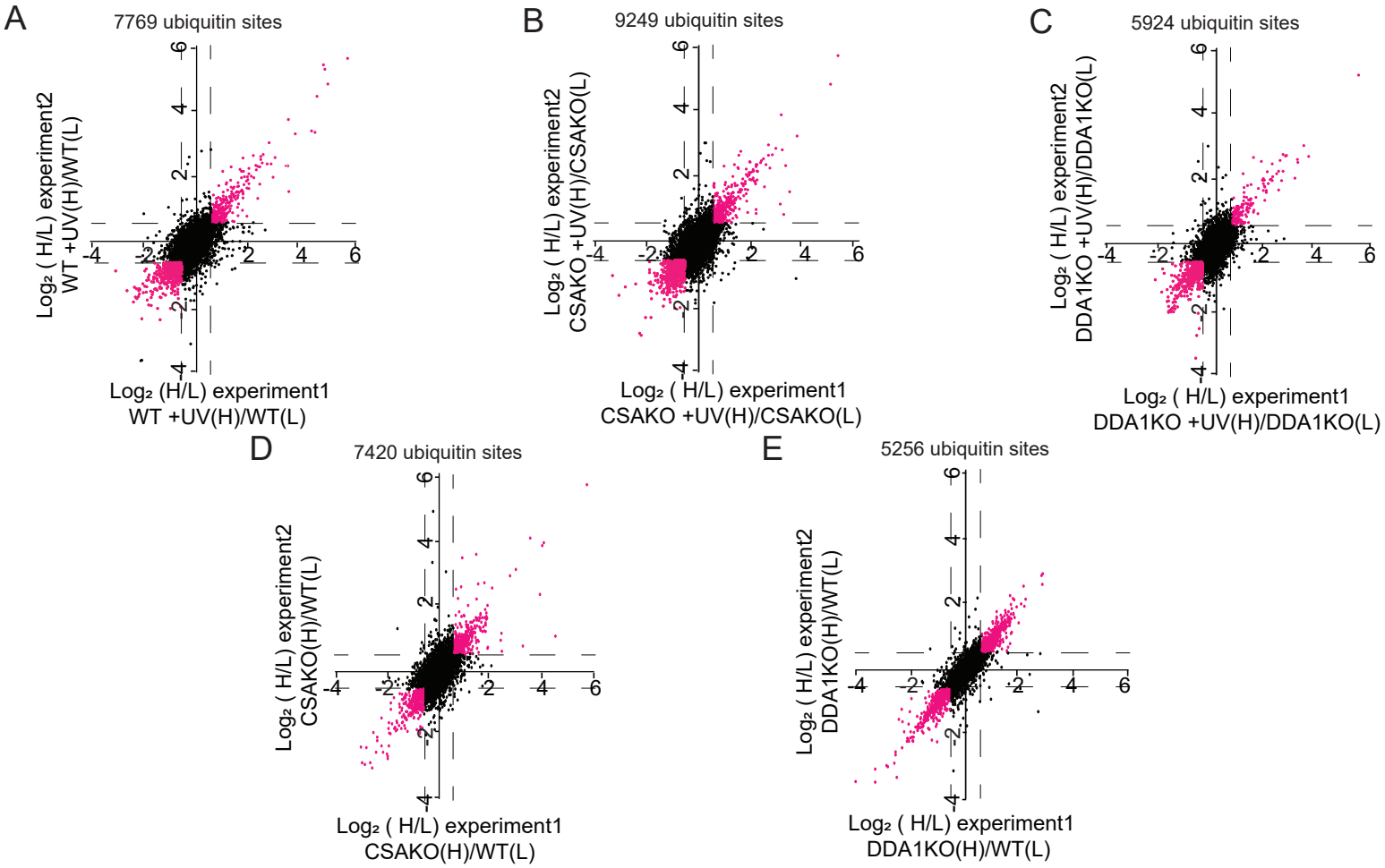

Supplementary Fig. 9

A

Top 50 up-regulated ubiquitin sites (WT)

GENE NAME	Ratio H/L (Log_2)	
(position)	Experiment1	Experiment2
XPC (364)	5.65	5.58
ERCC2 (751)	4.91	4.80
SF3B1 (1014)	4.80	5.26
XPC (374)	4.75	5.39
XPC (359)	4.50	4.43
HELLS (204)	4.42	3.32
TAP2 (245)	4.30	3.37
TRIP4 (245)	3.70	3.29
PSMA2 (171)	3.45	1.53
PSMC1 (413)	3.43	3.72
TMA7 (30)	3.40	2.31
HSPA8 (500)	2.93	2.56
YBX1 (118)	2.86	1.96
POLR2A (1268)	2.78	2.37
ACLY (1077)	2.71	3.01
POLR2A (1350)	2.64	2.36
SMARCA5 (814)	2.50	2.65
DDB2 (309)	2.45	2.40
XPC (174)	2.40	2.60
DDB2 (362)	2.39	2.51
OLA1 (190)	2.35	2.27
MYO10 (918)	2.35	1.75
CNBP (103)	2.28	2.29
RPS16 (4)	2.22	2.18
RPS12 (129)	2.22	2.32
CUEDC2 (272)	2.14	1.95
YBX3 (96)	2.12	2.62
YBX1 (64)	2.12	2.62
SND1 (513)	2.04	1.99
RPS27A (152)	1.96	2.06
RPL12 (48)	1.95	2.22
USP48 (551)	1.95	1.77
SUPT6H (306)	1.94	1.62
POLR2A (177)	1.91	1.89
RPS3 (230)	1.89	1.97
ABCE1 (397)	1.89	1.63
RPS10 (139)	1.85	1.84
XPC (161)	1.79	1.98
CNBP (8)	1.78	1.74
TIA1 (79)	1.74	2.14
UVSSA (414)	1.74	2.55
TOP1 (642)	1.73	1.50
PHRF1 (556)	1.70	1.57
CSDE1 (682)	1.68	2.14
ASCC3 (198)	1.67	1.95
CSDE1 (288)	1.67	1.53
RNH1 (46)	1.62	2.20
PHRF1 (768)	1.56	1.69
RNF170 (3)	1.56	1.50
CLPTM1 (460)	1.55	1.79

B

Top 50 up-regulated ubiquitin sites (CSA KO)

GENE NAME	Ratio H/L (Log_2)	
(position)	Experiment1	Experiment2
SF3B1 (1014)	5.42	5.68
XPC (374)	5.12	4.82
DSP (1033)	3.81	3.23
SH2B3 (373)	3.53	1.52
HSPA8 (500)	3.38	2.33
YBX1 (118)	3.25	2.81
PSMC1 (413)	3.21	3.88
DDB2 (309)	3.00	2.85
SMARCA5 (814)	2.86	2.65
CNBP (103)	2.77	2.25
DDB2 (106)	2.72	2.64
XPC (174)	2.71	2.96
SUPT6H (306)	2.61	2.36
SIVA1 (41)	2.57	1.68
OLA1 (190)	2.53	2.53
YBX3 (96)	2.44	2.48
YBX1 (64)	2.44	2.48
POLR2A (1350)	2.41	2.41
EDF1 (98)	2.28	2.15
RPS16 (4)	2.27	2.17
PRR14L (1861)	2.26	1.89
USP48 (551)	2.26	2.36
SUPT5H (258)	2.24	2.29
RPS12 (129)	2.24	2.36
MYH9 (856)	2.21	1.78
SPATS2L (11)	2.19	1.83
CNBP (8)	2.15	1.86
RPS10 (139)	2.14	2.16
SND1 (513)	2.12	2.21
XPC (161)	2.12	1.95
POLR2A (163)	2.09	2.15
POLR2A (1268)	2.09	1.90
CSDE1 (682)	2.03	1.88
RPL12 (48)	2.02	2.11
ACLY (1077)	2.01	2.43
ASCC3 (78)	1.99	2.44
RPS19 (111)	1.99	1.90
EIF2S2 (276)	1.96	2.04
BAZ2A (687)	1.96	2.11
POLR2A (177)	1.96	2.07
RPS3 (230)	1.91	2.00
PLEC (3106)	1.91	1.59
CUEDC2 (272)	1.86	2.06
POLH (709)	1.85	2.23
DCBLD2 (391)	1.82	1.85
TOP1 (642)	1.81	1.77
TOP1 (347)	1.80	1.61
SYNCRIP (297)	1.74	1.70
PHRF1 (768)	1.73	1.76
ASCC3 (213)	1.73	1.92

C

Top 50 up-regulated ubiquitin sites (DDA1 KO)

GENE NAME	Ratio H/L (Log_2)	
(position)	Experiment1	Experiment2
SF3B1 (1014)	5.21	5.16
PSMC1 (413)	3.38	2.68
TAP2 (245)	3.21	3.02
SMARCA5 (814)	2.99	2.51
XPC (183)	2.97	2.59
EDRF1 (694)	2.88	2.02
POLR2A (1268)	2.57	2.71
XPC (174)	2.53	2.70
POLR2A (1350)	2.44	2.24
OLA1 (190)	2.44	2.75
HSPA8 (500)	2.38	1.95
YBX3 (93)	2.33	2.57
YBX1 (64)	2.33	2.57
RPL12 (48)	2.28	2.24
ARIH1 (293)	2.27	1.66
RNF219 (502)	2.20	2.15
CSDE1 (682)	2.07	2.07
RPS10 (139)	2.05	1.96
SYNCRIP (407)	2.04	2.46
POLR2A (177)	2.00	1.99
DDB2 (106)	1.96	1.97
XPC (161)	1.90	1.85
USP48 (551)	1.86	2.22
POLR2A (163)	1.83	1.65
FASN (1752)	1.82	1.59
CNBP (8)	1.78	1.35
PHRF1 (556)	1.78	1.75
RPS3 (230)	1.75	1.79
RPS16 (4)	1.75	1.96
GAR1 (150)	1.72	1.65
YBX3 (150)	1.72	2.00
CSDE1 (288)	1.72	1.85
SUPT6H (306)	1.70	1.97
TMA7 (30)	1.68	1.96
UVSSA (414)	1.64	2.54
RPS2 (58)	1.53	1.71
ABCE1 (397)	1.45	1.44
ASCC3 (319)	1.37	1.04
NUMA1 (1475)	1.36	2.65
DDB1 (204)	1.33	1.25
H1F0 (12)	1.28	1.19
RPS27A (113)	1.26	1.39
SMARCA5 (836)	1.26	1.26
SUPT6H (1100)	1.26	1.83
DRG1 (46)	1.25	1.19
PSIP1 (6)	1.24	1.39
RPS3 (214)	1.23	1.34
TANK (199)	1.23	1.19
RPA1 (167)	1.21	1.11
SND1 (886)	1.17	1.36

Supplementary Fig. 10

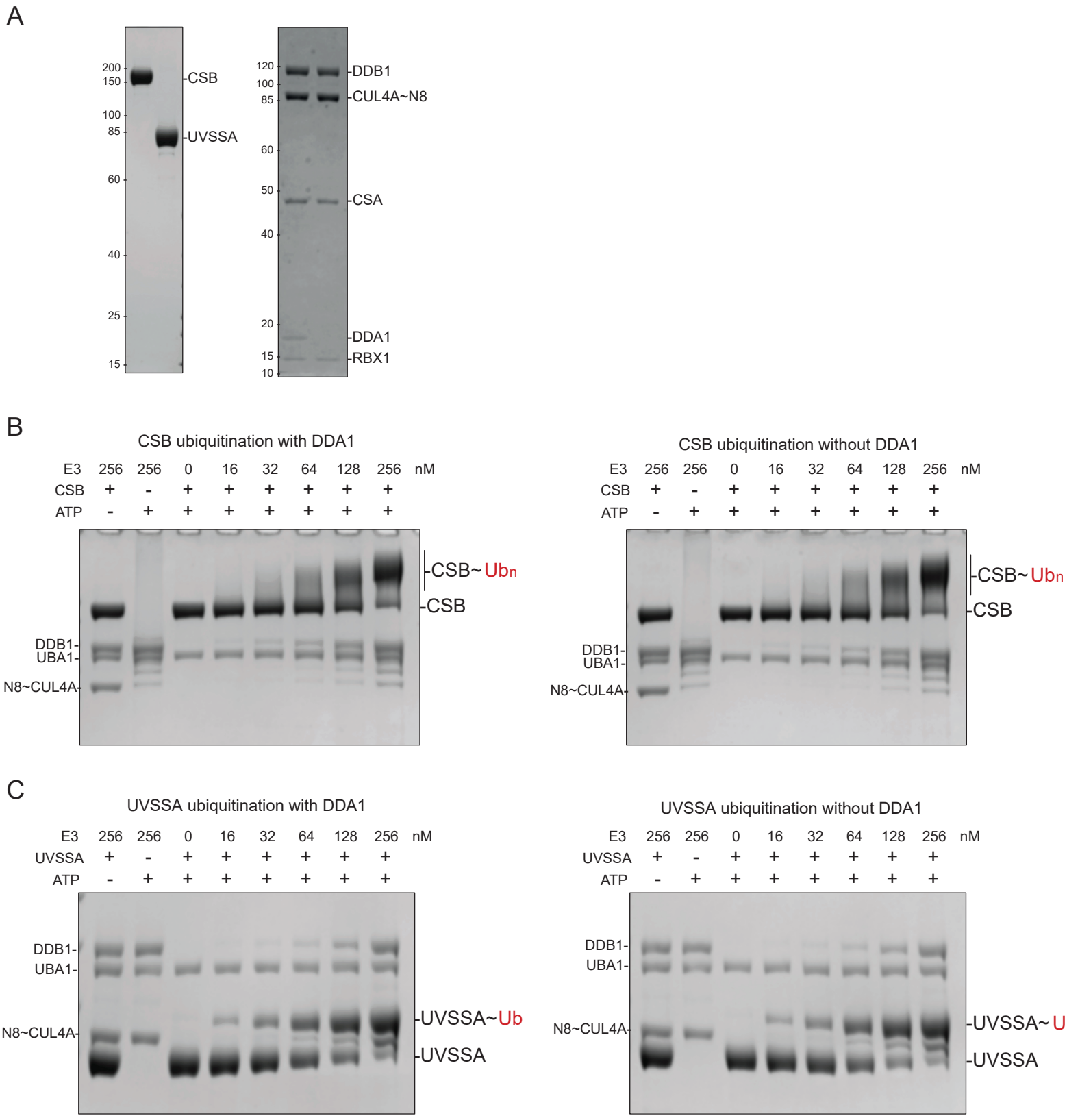

Supplementary Fig. 11

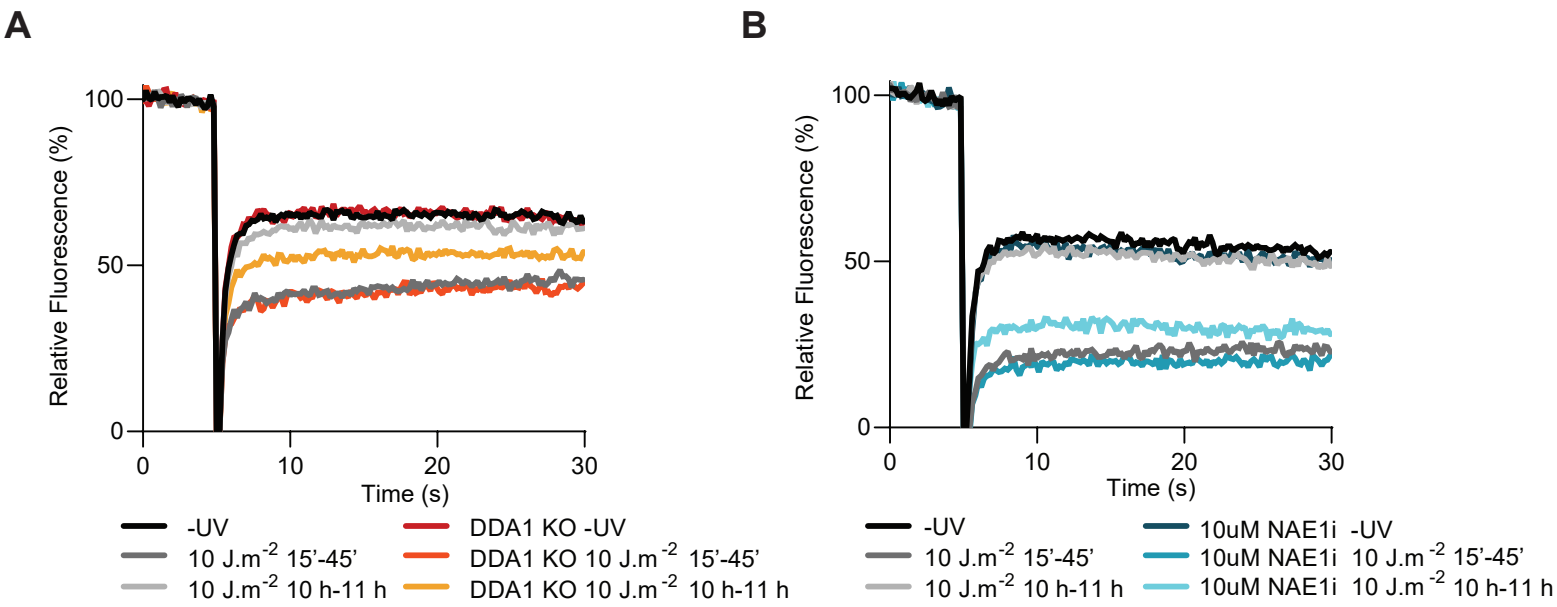

Supplementary Fig. 12

Figure 1C

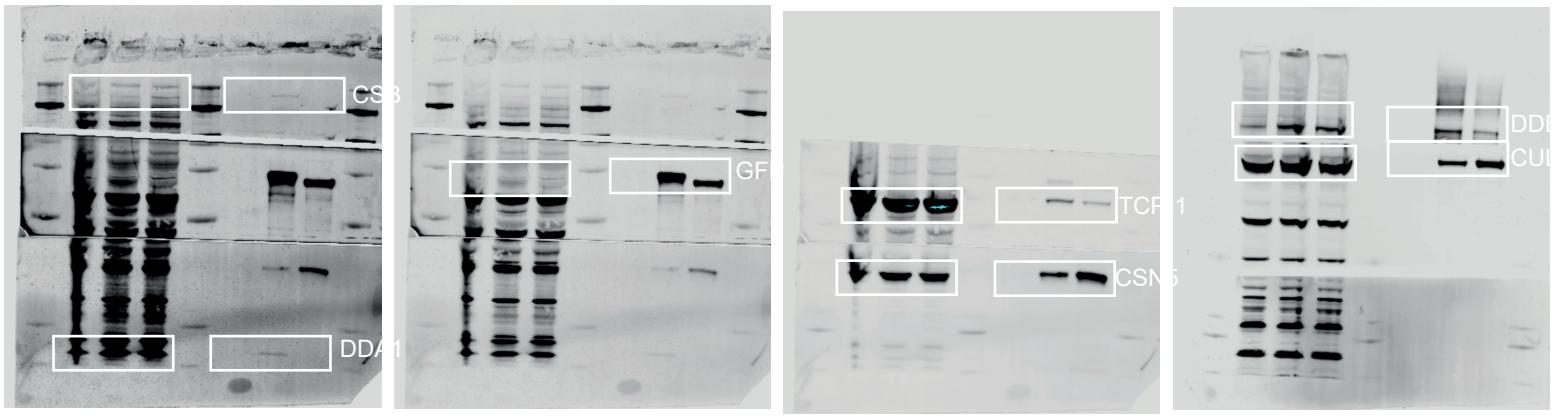

Figure 3C

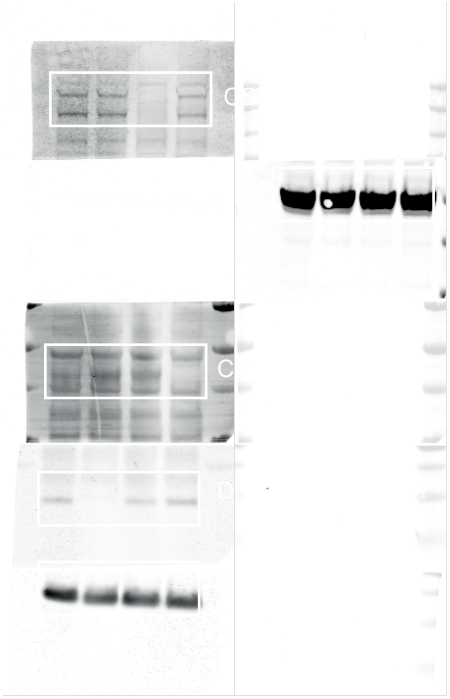

Supplementary Figure 1B

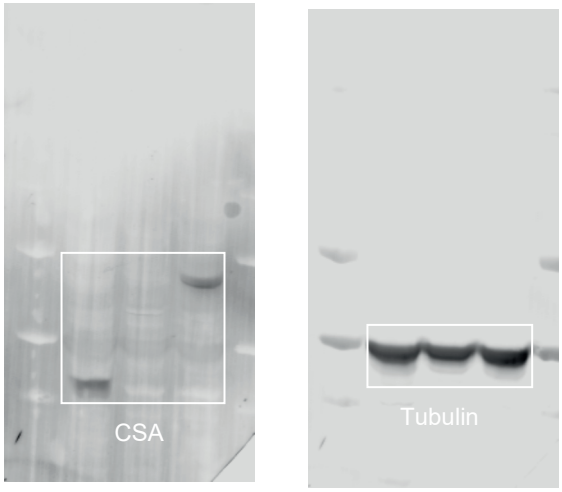

Supplementary Figure 2A

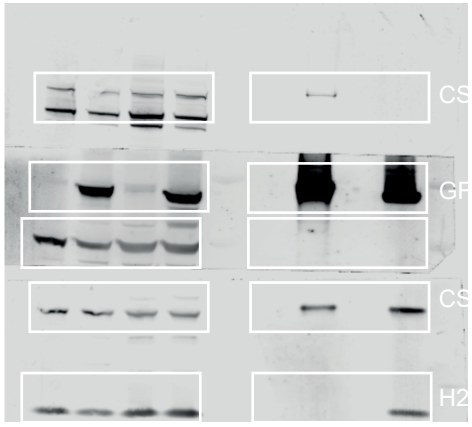

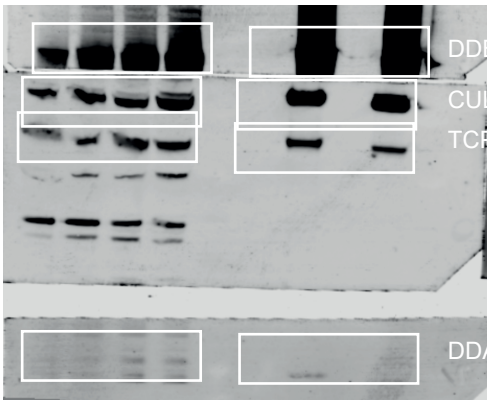

Supplementary Figure 3C

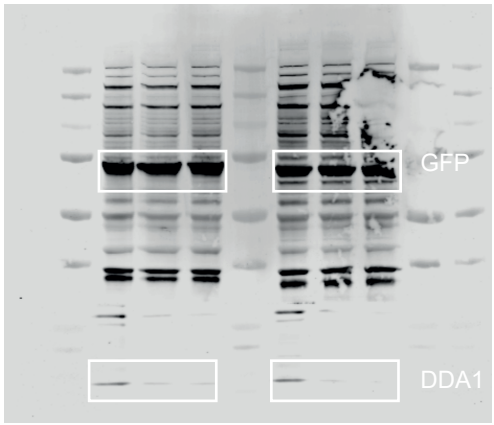

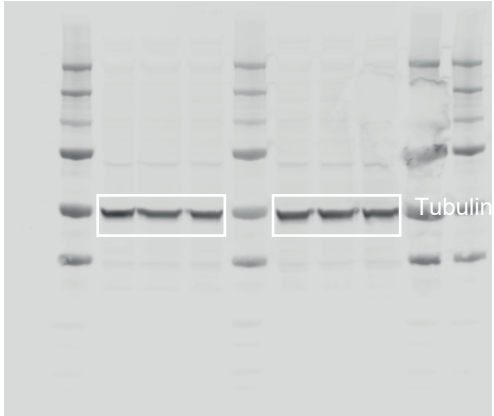

Figure 6C

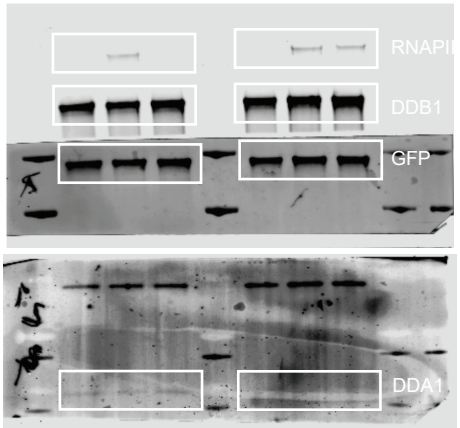

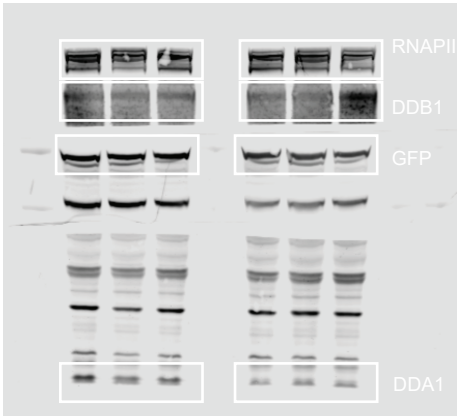

Supplementary Fig 10B

with DDA1

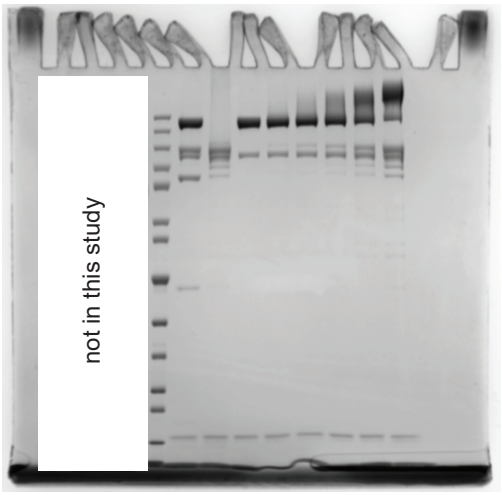

without DDA1

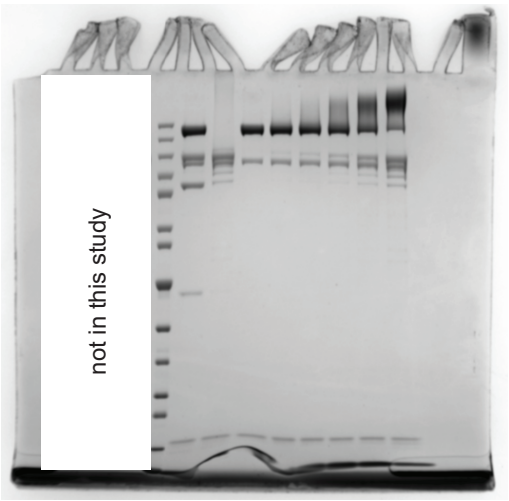

Supplementary Fig 10C

with DDA1

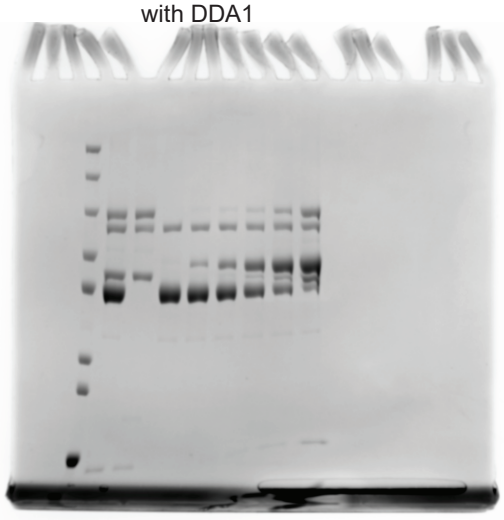

without DDA1

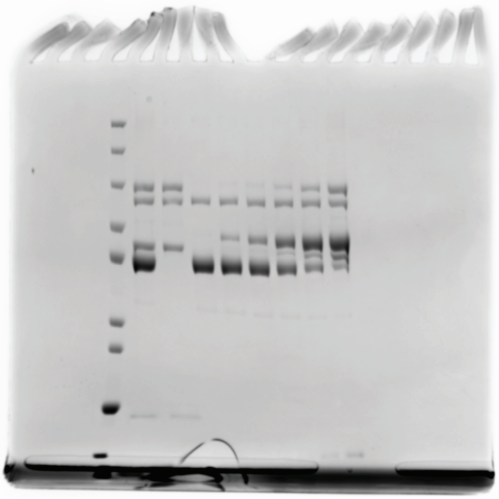

Supplementary Files

This is a list of supplementary files associated with this preprint. Click to download.

- SupplementaryTable1CSAmClover.xlsx
- SupplementaryTable2GFPDDB2.xlsx
- SupplementaryTable3CSAmCloverDIA.xlsx
- SupplementaryTable4Ubiquitinprofile.xlsx
- SupplementaryTable5Proteinprofile.xlsx
- cryoEMtable.doc
- D1292133145valreportfullP1.pdf
- Datadeposition.docx